

An Algorithmic Approach to Ion Structure and Dynamics in Astrophysical and Laboratory Plasmas

by

J Isaac Garcia

A dissertation submitted to the Graduate Faculty of
Auburn University
in partial fulfillment of the
requirements for the Degree of
Doctor of Philosophy

Auburn, Alabama
December 13, 2025

Keywords: Photoionized plasmas, dielectronic recombination, configuration-interaction, ion spectroscopy, decision tree, machine learning

Copyright 2025 by J Isaac Garcia

Approved by

Stuart Loch, Professor of Physics
Mike Fogle, Professor of Physics
Christopher J Fontes, Dr. of Physics
David Maurer, Professor of Physics
Luca Guazzotto, Professor of Physics
Dennis Bodewitz, Professor of Physics

Abstract

For astrophysical photoionized plasmas, the atomic process of dielectronic recombination (DR) is critically important in ionization balance modeling and the determination of elemental abundances in the Universe. DR rate coefficients are known to have large uncertainties at low temperatures. In this work, this issue is addressed by the development of a decision tree algorithm, called CRISTAL (Complex Resolved Ion Spectroscopy Tree ALgorithm) that selects large configuration sequences for configuration-interaction atomic structure calculations.

CRISTAL is designed to exploit the rules for configuration mixing for dimensional reduction of the configuration space: it compares computed energies against measured values and iteratively reduces the selected configuration sequence. We compute energies, resonance heights, and Maxwellian rate coefficients for Lithium-like and Beryllium-like Carbon and Nitrogen and compare the results to storage ring measurements and archived data to make the improvements clear. We report an average difference for selected resonance positions on the order of 0.1eV at a maximum n -shell of 6. Additionally, the scaling of the number of configurations with number of orbitals is reduced from quintic to cubic in the Beryllium-like case and from quartic to quadratic in the Lithium-like case.

The code results demonstrated that the optimum CRISTAL configuration sequence was invariant along both isoelectronic sequences, motivating a general proof of this invariance for any isoelectronic sequence. Thus, higher members of an isoelectronic sequence can be calculated once an optimum configuration set is generated.

It is standard practice to use the first-order approximation known as Fermi's Golden rule to calculate the Auger rates in DR calculations. We derive a method to assign an upper bound on the uncertainty in Auger rates using the Dyson series, the exact perturbative expansion of the evolution operator.

Currently, CRISTAL neglects the configuration-interaction rule for angular momentum. In the interest of improving the algorithm, we test a novel approach for calculating angular momentum coupling coefficients for the 2-particle case and outline a generalization for the N-particle case.

With the method outlined above, significant progress has been made in improving the method to calculate low temperature DR rate coefficients. The work opens up a number of interesting future directions.

Artificial Intelligence (AI) Use Disclosure Statement

In the preparation of this dissertation, no Artificial Intelligence (AI) tools were used.

Acknowledgments

A number of contributors and supporters to this work should be acknowledged: Stuart Loch for his help as my advisor and his support throughout the many challenges I've faced throughout the course of this project; Clayton Chillen for many contributions to the data visualization and analysis; Christopher J Fontes for his advice on configuration interaction, his help reviewing important foundational literature, and his feedback on the work; Evan Garbe and Phillip Stancil for their work reproducing archived ADAS data; Christopher Coger for his help in reviewing the derivative of a perturbation with respect to a continuous parameter; Duy Nguyen Vu Hoang for his original derivation of the error bound on Fermi's golden rule; Jay and Chancy Blackburn for encouraging my higher education and pursuing a career in science; Carmen and Danny Garcia for their continued support in my academic career and my early life.

Table of Contents

Abstract	ii
Acknowledgments	v
List of Tables	viii
List of Figures	ix
1 Introduction	1
2 Atomic Structure and Configuration Interaction	8
2.1 Relativistic and Nonrelativistic Hamiltonians	8
2.2 Central Field Approximation and Configuration Interaction	10
2.3 Rules for Configuration Mixing	17
2.4 Minimal Assumption	18
3 A Decision Tree Learning Algorithm	21
3.1 Tree Data Structures	21
3.2 The Complex Resolved Ion Spectroscopy Tree Algorithm (CRISTAL)	26
3.3 Truncation functions and decision forests	33
3.4 Results from CRISTAL	36
4 DR Rate Coefficient Results	43
4.1 Plasma Dielectronic Recombination Rate Coefficients	44
4.1.1 Cooler Distribution	45
4.1.2 Maxwellian Distribution	49
5 A Theorem for Isoelectronic Hamiltonians	51
6 Quantum Transitions	59
6.1 The method of time varying coefficients	59
6.2 The operator approach	61

6.3	A criterion for the validity of Fermi's Golden Rule	65
7	Coupling Angular Momenta	70
7.1	Two particles	73
7.2	N particles	81
7.3	Exchange symmetries	88
8	Conclusion	91
	Appendices	105
A	Operator Relations	106
A.1	Commutators with products of operators	106
A.2	Block diagonal matrices	107
B	Angular momentum of a single particle	109

List of Tables

3.1	The shell prefixes removed by CRISTAL. Rows correspond to the truncation function used and columns correspond to the ion.	41
-----	---	----

List of Figures

1.1	An image of the Cat's eye nebula which was processed to make the concentric rings surrounding the inner core apparent[1].	2
1.2	The charge state abundance of C^+ and C^{2+} in a planetary nebula as a function of the radial distance from the stellar surface as calculated by CLOUDY. The solid line is using the current theoretical DR rates and the dotted line uses improved experimental rates.	3
1.3	The DR rate coefficient for O^{4+} recombining to O^{3+} for a storage ring experiment as a function of the input electron energy. The experimental data is plotted in gray. The solid line shows the current calculated rate, which agrees well with experiment above 12eV ($\approx 1.4 \times 10^5 K$), but has poor agreement in the region below this point.	6
3.1	The calculated energy difference with NIST averaged over a configuration for the configurations $1s^2 2s 2p^2$ (left) and $1s^2 2s 2p 3d$ (right) for C^{2+} as a function of the maximum n -shell when including only the first few Rydberg sequences ($1s^2 2s^2 nl$, $1s^2 2s 2p nl$, and $1s^2 2p^2 nl$). The red lines are the average differences when using only the first Rydberg sequence, the green lines are those calculated when using the first two Rydberg sequences and the blue lines are those calculated when using the first three Rydberg sequences.	22
3.2	The first three levels of a configuration tree for a 4-electron system. Prefixes are shown for two extremes: the ground configuration is on the left-most branch and the highest energy configuration prefixes can be found on the right-most branch.	26

3.3	Caption: The first three levels of the complex tree for a 4-electron ion.	28
3.4	(A) Degraded = True, basic case. (B) Degraded = True, basic terminating case.	29
3.5	(A) Degraded = False, basic case. (B) Degraded = False, basic terminating case.	29
3.6	A general chain of nodes of length N	30
3.7	(A) Degraded = True, partial chain. (B) Degraded = True, chain reaches n_{\max}	31
3.8	(A) Degraded = False, partial chain created. (B) Degraded = False, created chain reaches n_{\max} . (C) Degraded = False, pre-existing chain.	32
3.9	A graph demonstrating the closure of CRISTAL within a given n_{\max} , i.e. the algorithm will terminate at a node at the bottom level of the tree (which corresponds to the current value of n_{\max}) without any navigation errors.	33
3.10	A detailed flowchart that illustrates the complete operation of CRISTAL beginning with the initialization of the parameters (such as the total number of electrons, the proton number, the representative configurations, and the starting n_{\max}) and terminating at its criterion for convergence.	34
3.11	The weighted average difference from the tabulated energies as a function of the iteration. Iterations are labeled by the current n -shell and the current iteration within that n -shell, e.g. "n5iter0" for the 5th n -shell at the 0th iteration. Rows correspond to the ion (C^+ , N^{2+} , and O^{3+} from top to bottom) and columns correspond to the truncation function ("aufbau", "ntot", and "brute" from right to left). The horizontal red dotted lines show the average difference calculated using the AUTOSTRUCTURE input files from the ADAS archive.	38

3.12	C ⁺ configuration average differences from the tabulated energies calculated from CRISTAL as a function of the iteration (see Figure 3.11) compared to the same quantity calculated from the archived AUTOSTRUCTURE input files (red dotted line). Rows correspond to the truncation function and columns correspond to the configuration. . .	39
3.13	N ²⁺ configuration average differences from the tabulated energies calculated from CRISTAL as a function of the iteration (see Figure 3.11) compared to the same quantity calculated from the archived AUTOSTRUCTURE input files (red dotted line). Rows correspond to the truncation function and columns correspond to the configuration. . .	40
3.14	O ³⁺ configuration average differences from the tabulated energies calculated from CRISTAL as a function of the iteration (see Figure 3.11) compared to the same quantity calculated from the archived AUTOSTRUCTURE input files (red dotted line). Rows correspond to the truncation function and columns correspond to the configuration. . .	41
4.1	Beam Auger resonance plots for (A) C ⁺ and (B) N ²⁺ as a function of the electron beam kinetic energy in eV relative to the ionization threshold. The experimental data from the storage ring is shown in green, the calculated data using CRISTAL's large CI and optimized orbital scaling parameters is shown in black, and the data from the ADAS archive using default AUTOSTRUCTURE with an extra shift of the ground state energy resonance nearest to the ionization threshold is shown in red. (A) also includes a dashed blue curve that shows the data calculated using default AUTOSTRUCTURE without any extra shift of the ground state energy. This blue curve is not shown in panel (B) because the shift did not significantly change the resonances in this case. Vertical dashed green lines show the tabulated resonance positions from the NIST database [2].	46

4.2 Maxwellian rate coefficients for (A) C^+ and (B) N^{2+} as a function of the plasma temperature in Kelvin. Experimental data from the storage ring is shown in green, the calculated data using CRISTAL's large CI and optimized orbital scaling parameters is shown by the black dashed curve, the data calculated using the archived AUTOSTRUCTURE input file with a shift of the ground state energy is shown by the red dotted curve, and the data calculated using the archived AUTOSTRUCTURE with no additional shift is shown by the red dot-dashed curve. Note that panel (B) only shows the archived AUTOSTRUCTURE calculation without the additional shift because the shift had no effect in this case. 49

4.3 Maxwellian rate coefficients for (A) C^{2+} and (B) N^{3+} as a function of the plasma temperature in Kelvin. Experimental data from the storage ring is shown in green, the calculated data using CRISTAL's large CI and optimized orbital scaling parameters is shown by the black dashed curve, the data calculated using the archived AUTOSTRUCTURE input file with a shift of the ground state energy is shown by the red dotted curve, and the data calculated using the archived AUTOSTRUCTURE with no additional shift is shown by the red dot-dashed curve. 50

Chapter 1

Introduction

Determining and mapping out the abundances of elements is critically important in understanding the origins, creation, and distribution of elements in the universe and in our local galaxy. Photoionized plasmas, such as planetary nebulae, are very good candidates for such studies [3–6]. As an example, a processed image of the Cat’s eye nebula (NGC 6543) [1] is shown in Figure 1.1. Parker [7] gives a thorough review of this research topic. Planetary nebulae have been used to map abundances throughout the Milky Way [8], in the Galactic bulge [9], and near the Galactic core [10]. These environments are under the broader category of low temperature plasmas, which includes many laboratory plasma experiments [11]. In this work, we seek to improve low temperature chemical abundance diagnostics in astrophysical and laboratory plasmas by improving the accuracy of dielectronic recombination (DR) rate coefficients.

In the steps to determine the elemental abundances for astrophysical photoionized plasmas, DR is often the largest source of uncertainty. First, for a given charge state, an observed spectral line is used along with a theoretical line intensity to determine the charge state’s abundance (e.g., the abundance of C^{2+} relative to the hydrogen abundance). It is quite likely that not all of the charge states from that element can be observed due to the wide range of wavelengths over which the charge states will emit. Factors known as Ionization Correction Factors (ICFs) [12] are used to convert from the charge state abundance to the elemental abundance. These ionization ICFs are evaluated from an ionization balance calculation, usually within a photionized plasma model (e.g. CLOUDY [13]). Electron-impact ionization and recombination atomic data are used in these ionization balance calculations, with low temperature DR being the most significant source of uncertainty [14].



Figure 1.1: An image of the Cat's eye nebula which was processed to make the concentric rings surrounding the inner core apparent[1].

Chemical compositions of photoionized (PI) nebulae are important for stellar nucleosynthesis and yields, galactic evolution, active galactic nuclei, and interstellar and intergalactic matter. Low-temperature DR rate coefficients are a large source of uncertainty in modeling kilonovae to extract abundance patterns [15]. Most models, like Cloudy [13] and ATOMDB [16], use purely theoretical DR rate coefficients. These theoretical DR calculations are distributed without specifying the uncertainties. As an illustration of the sensitivity of modeling results to DR rates, consider the results shown in Figure 1.2. Replacing the currently used DR theory data in the photoionization code Cloudy [13] with available experimental data from storage ring measurements illustrates the impact of improving low temperature DR rates on the modeling and diagnostics of photoionized plasmas. It can be seen that the abundances of carbon charge states as a function of the distance from the central star are significantly affected. For Fe M-shell ions in Seyfert galaxies, the low temperature DR rate coefficients can change the value of the ionization parameter that produces the maximum population by more than a factor of two [17]. DR rate coefficients for Fe need to be larger by a factor of 10 to match the ionization balance in NGC3783 [17, 18]. This has been confirmed theoretically [19] and later experimentally for Fe¹³⁺ [20]

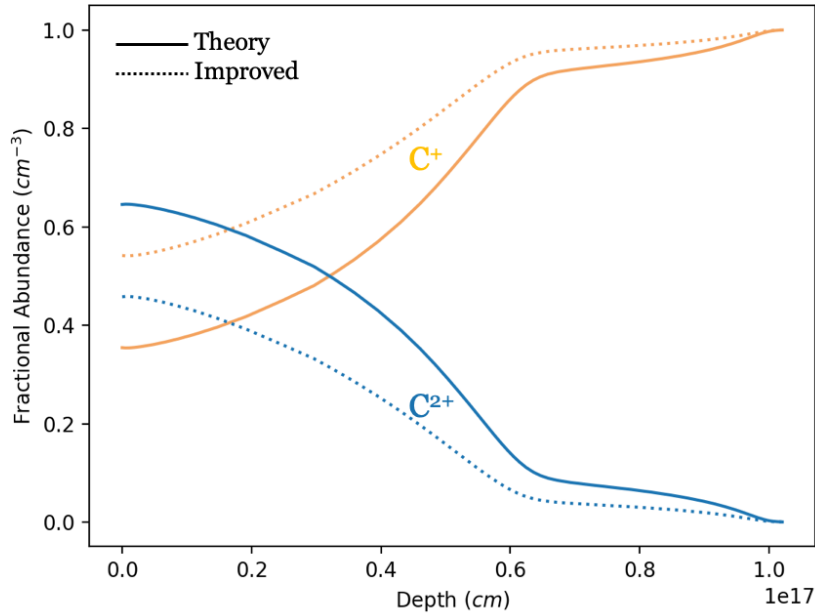
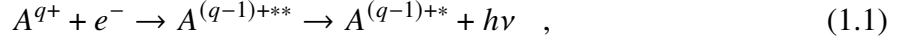


Figure 1.2: The charge state abundance of C^+ and C^{2+} in a planetary nebula as a function of the radial distance from the stellar surface as calculated by CLOUDY. The solid line is using the current theoretical DR rates and the dotted line uses improved experimental rates.

Improving low temperature DR rate coefficients would also make an impact on modeling the divertors of fusion tokamak experiments. A fusion edge plasma condition known as a 'detached divertor' [21] can have electron temperatures less than an eV [22] and often elements that are a few times ionized. Thus, improvements to low temperature DR rate coefficients would impact the modeling of impurities in detached divertors. This regime is important for the operation of tokamaks at high-performance conditions [21].

Previous work on DR rate coefficients includes that of the DR project of Nigel Badnell ([23] with 13 associated isoelectronic sequence papers [24–36]), the work using the Flexible Atomic Code [37]; *R*-matrix calculations (e.g. [38–41]), and GRASP calculations (e.g. [42]). Other than selected calculations by Sochi and Storey [38] and Pindzola [42], all focused on collisionally ionized plasmas (high temperature). For example, the DR project [23] and the FAC-DR data [37] both contain accurate rate coefficients for collisionally-ionized plasmas but have large uncertainties in the low temperature photoionized regime [14].

Generally, the DR process is a reaction which begins with an ion subject to electron impact excitation and then followed by radiative relaxation of either the captured electron or the excited core electron. This is expressed in the following chemical equation:

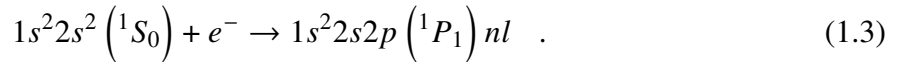


where A^{q+} is an ion with total charge q , the asterisk in the superscript denotes the number of electrons that are excited, and the term $h\nu$ signifies that a photon with frequency ν was emitted. By energy conservation, electron capture can only occur when the electron has energy satisfying:

$$E_{\text{inc}} = \Delta E_{\text{core}} + E_{nl} \quad , \quad (1.2)$$

where E_{inc} is the initial energy of the incoming electron, ΔE_{core} is the energy imparted to the core electron, and E_{nl} is the energy of the incoming electron after capture.

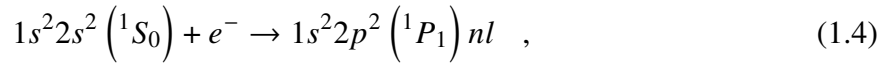
As a simple concrete example, consider a Beryllium-like system, i.e. a four-electron system. For brevity, we will frequently use the chemical abbreviation for the elements; in this case Be-like for Beryllium-like and B-like for Boron-like. One possible dielectronic capture channel would be:



Here we are using the standard spectroscopic notation to denote each configuration as well as the Russel-Saunders notation [43] to specify the particular angular momentum coupling of the electrons. This can undergo either autoionization back to the Be-like system, or radiative decay. The electron is captured if the system radiatively decays to a bound state below the ionization potential of the B-like system, which would complete the DR process. The radiative decay can be via a core electron decay (e.g. $1s^2 2s 2p({}^1P_1) nl \rightarrow 1s^2 2s^2 ({}^1S_0) nl + h\nu$) or via a Rydberg electron decay (e.g. $1s^2 2s 2p({}^1P_1) nl \rightarrow 1s^2 2s 2p({}^1P_1) n'l' + h\nu'$). The photons associated with

core radiative decays are often called **satellite lines** due to their wavelength proximity with strong radiative transitions from the recombining ion.

Note that it is also possible to excite more than one core electron. For example, one case of **trielelectronic recombination** in the above system would be:



followed by the radiative decay channels. This process, in fact, was the source of the large near threshold resonance for O^{4+} as measured by Fogle [44]. In recent years, it has been found that trielectronic recombination plays a significant role for complex systems [45–47].

Doubly (and higher) excited states are the main challenge. At high temperatures, the distance between the captured electron and the core electrons is sufficient to approximate the potential as a shielded nuclear potential, i.e. the Rydberg approximation applies. This fails at low temperatures where the electron interactions are non-negligible. Then, in order to refine the DR rate coefficients, it is necessary to refine the stationary states. This is illustrated in Figure 1.3 for the case of O^{4+} recombining to O^{3+} . Here, it can be seen that the theory results are in good agreement with the experimental measurements at higher energies (above about 12eV). At lower temperatures, particularly within the first few eV, there are many sizable differences in resonance positions and heights between theory and experiment. This highlights the main difficulty of calculating low temperature DR, the challenges of calculating accurate resonance positions and heights at low energies.

With the exception of oxygen, most abundance calculations require an ICF to account for unobserved ionization stages in the absence of multi-wavelength observations. ICF's are a significant source of uncertainty [48, 49] for abundance diagnostics in photoionized plasmas. As explained above, DR rates have proven difficult to calculate to sufficient accuracy at low-temperatures due to nontrivial electron interactions. An accidental shift of the low energy resonances in the DR rate of larger than ≈ 0.1 eV can cause significant inaccuracies in the overall rate coefficient. For

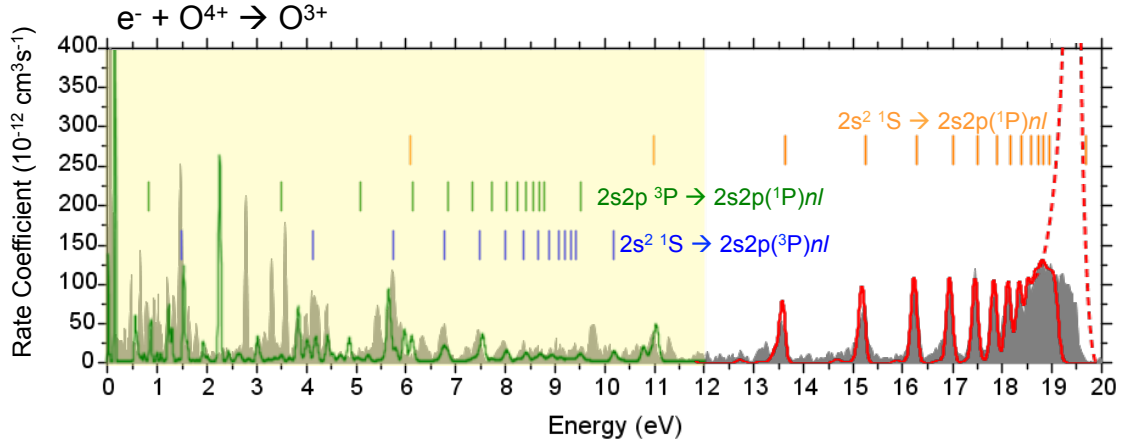


Figure 1.3: The DR rate coefficient for O^{4+} recombining to O^{3+} for a storage ring experiment as a function of the input electron energy. The experimental data is plotted in gray. The solid line shows the current calculated rate, which agrees well with experiment above 12eV ($\approx 1.4 \times 10^5$ K), but has poor agreement in the region below this point.

example, removing just one low energy resonance in O^{4+} results in a factor of 10 difference in the Maxwellian at photo-ionization temperatures [44]. Likewise, in Mg^{8+} , shifting a single resonance by 100 meV changes the rate coefficient by a factor of 2.7 at similar temperatures [50].

To address this issue, we have developed a decision tree algorithm for optimizing the selection of large configuration sequences. This algorithm uses the Breit-Pauli atomic structure code, AUTOSTRUCTURE, to compute energy spectra and compare against selected experimentally measured energies. As benchmarks, we use recent storage ring experiments performed at CRYRING@ESR as well as data recorded in the NIST atomic spectra database. The average difference between the computed energies and these experimentally measured energies is used as a cost function to guide the algorithm to convergence on an optimum selection of configurations.

Foundational work in multi-configuration atomic structure is described by Fischer [51] and Cowan [52]. Two of the earliest codes developed for CI atomic structure calculations include Cowan’s code [52] and HULLAC [53]. The Los Alamos National Lab Cowan Atomic Structure package (CATS) is based upon Cowan’s code and subsequent modifications and updates [54–56]

and is frequently used for large configuration-interaction calculations [57]. The GRASP code [58–60], is an example of a relativistic multi-configuration atomic structure code. The atomic structure code we use, AUTOSTRUCTURE, was developed by Nigel Badnell [61–63] and specializes in homogeneous, nonrelativistic central field approximations. Recent work on developing algorithmic approaches to improving CI calculations include a deep learning neural network approach [64], Monte Carlo simulations [65], and configuration state function generators [66].

In the next chapter we will review the theory of atomic structure and configuration interaction, and set the foundation for the chapters that follow. In Chapter 3, we motivate and describe the decision tree algorithm we have developed and show the convergence behavior for the selected isoelectronic sequences and their general structure. We carry these calculations through to storage ring resonances and Maxwellian rate coefficients in Chapter 4. The results of these calculations suggest an invariance of the optimum configuration-set along an isoelectronic sequence. Although it is common to assume such an invariance in the field of atomic structure modeling, we want to be confident enough in this result to extrapolate the optimum configuration set along any isoelectronic sequence we would do calculations on. Thus, a proof of the invariance has been developed in Chapter 5. The codes that we use to calculate a DR rate coefficient use the first-order approximation to the quantum transition rate known as Fermi’s Golden Rule. This choice is a potential source of uncertainty in our method, and a criterion for validity of the approximation would be helpful. We derive such a criterion in Chapter 6. Currently, CRISTAL neglects the configuration-interaction rule for angular momentum, which requires that two interacting configurations have at least one pair of orbital and spin total angular momentum quantum numbers in common. The computational expense could potentially be reduced with a method of determining the allowed angular momentum couplings. We test a novel approach for calculating angular momentum coupling coefficients for the 2-particle case and outline a generalization for the N-particle case in Chapter 7.

Chapter 2

Atomic Structure and Configuration Interaction

In this chapter, an outline is given of atomic structure and the role of configuration interaction in modeling atomic structure. This outline will serve firstly to clarify the procedure followed by our atomic structure code and the foundations on which it is built and secondly to justify the rules of configuration interaction which will form the building blocks for the decision tree algorithm. This will then be expanded upon in Chapter 3, with the results shown at the end of Chapter 3 and in Chapter 4.

2.1 Relativistic and Nonrelativistic Hamiltonians

We begin with the Hamiltonian for an ion with N_e electrons and a nuclear charge of $+eZ$. In the fully relativistic form, we have the Dirac-Coulomb-Breit Hamiltonian [67]:

$$\widehat{H}_{\text{DCB}} = \sum_i \widehat{H}_{\text{D},i}^{(f)} + \frac{e^2}{4\pi\epsilon_0} \left(-\frac{Z}{r_i} + \sum_{j<i} \frac{1}{r_{ij}} \right) - e\varphi^{(x)}(\mathbf{r}_i) - ec\vec{\alpha} \cdot \mathbf{A}^{(x)}(\mathbf{r}_i) + \frac{\mu_0}{4\pi} (ec|g_e|)^2 \sum_{j<i} \widehat{B}_{ij} \quad , \quad (2.1)$$

where the free Dirac Hamiltonian is:

$$\widehat{H}_{\text{D},i}^{(f)} = -i\hbar c(\vec{\alpha} \cdot \nabla_i) + \beta m_e c^2 = c\vec{\alpha} \cdot \widehat{\mathbf{p}}_i^{(f)} + \beta m_e c^2 \quad , \quad (2.2)$$

and the Breit operator is:

$$\widehat{B}_{ij} \equiv -\frac{1}{2r_{ij}} \left[\vec{\alpha}_i \cdot \vec{\alpha}_j + \frac{(\vec{\alpha}_i \cdot \mathbf{r}_{ij})(\vec{\alpha}_j \cdot \mathbf{r}_{ij})}{r_{ij}^2} \right] . \quad (2.3)$$

In order to take the nonrelativistic limit of this Hamiltonian we must first apply the Foldy-Wouthuysen [68] transformation, a unitary transformation of the form:

$$\widehat{H} \rightarrow \widehat{U}(\theta)\widehat{H}\widehat{U}^{-1}(\theta) , \quad (2.4)$$

$$\widehat{U}(\theta) = \exp\left(\beta \frac{\vec{\alpha} \cdot \widehat{\mathbf{p}}}{|\widehat{\mathbf{p}}|} \theta\right) = \widehat{I}_4 \cos(\theta) + \beta \frac{\vec{\alpha} \cdot \widehat{\mathbf{p}}}{|\widehat{\mathbf{p}}|} \sin(\theta) . \quad (2.5)$$

If we let $\tan(2\theta) = \frac{|\widehat{\mathbf{p}}|}{mc}$, it can be shown that the transformed Hamiltonian takes the form:

$$\widehat{H}_{\text{NW}} = c\beta\sqrt{(mc)^2 + \widehat{p}^2} , \quad (2.6)$$

which is the Newton-Wigner representation[69] of the Hamiltonian of a relativistic fermion. Noting that β acts on the bispinor part of a wavefunction and is a diagonal matrix, the matter part of the Hamiltonian can now be treated separately from the antimatter part. By Taylor expanding the above and taking the limit for small $\frac{|\widehat{\mathbf{p}}|}{mc}$, we acquire a Hamiltonian corrected to second order:

$$\widehat{H}_{\text{NR}}^{(2)} = \beta \left(mc^2 + \frac{\widehat{p}^2}{2m} - \frac{\widehat{p}^4}{8m^3 c^2} \right) . \quad (2.7)$$

Finally, we must incorporate gauge covariance by letting $\widehat{H} = \widehat{H}^{(\text{f})} + q\varphi(\mathbf{r})$ and $\widehat{p}^2 = \left[\widehat{\boldsymbol{\sigma}} \cdot \left(\widehat{\mathbf{p}}^{(\text{f})} + q\mathbf{A} \right) \right]^2$.

With this prescription, we have the standard Breit-Pauli Hamiltonian [70]:

$$\begin{aligned} \widehat{H}_{\text{BP}} = \sum_i \left[\widehat{H}_{\text{NR},i}^{(2)(f)} + \frac{e^2}{4\pi\epsilon_0} \left(-\frac{Z}{r_i} + \sum_{j<i} \frac{1}{r_{ij}} \right) - e\varphi^{(x)}(\mathbf{r}_i) \right. \\ \left. + \widehat{H}_{\mathbf{E}(r_i),\mathbf{p}_i} + \widehat{H}_{\mathbf{A}^{(x)}(r_i),\mathbf{p}_i} + \widehat{H}_{\mathbf{B}^{(x)}(r_i),\mathbf{S}_i} + \widehat{H}_{\mathbf{S}_i,\mathbf{p}_i} + \sum_{j<i} \widehat{H}_{\mathbf{S}_i,\mathbf{p}_j} + \widehat{H}_{\mathbf{p}_i,\mathbf{p}_j} + \widehat{H}_{\mathbf{S}_i,\mathbf{S}_j} \right] , \end{aligned} \quad (2.8)$$

where:

$$\begin{aligned} \widehat{H}_{\mathbf{E}(r_i),\mathbf{p}_i} &\equiv \frac{ie\hbar}{(2m_e c)^2} \left(\mathbf{E}^{(x)}(\mathbf{r}_i) - \frac{Ze}{4\pi\epsilon_0} \frac{\mathbf{r}_i}{r_i^3} \right) \cdot \widehat{\mathbf{p}}_i , \\ \widehat{H}_{\mathbf{A}^{(x)}(r_i),\mathbf{p}_i} &\equiv \frac{e|g_e|}{2m_e} \mathbf{A}^{(x)}(\mathbf{r}_i) \cdot \widehat{\mathbf{p}}_i , \\ \widehat{H}_{\mathbf{B}^{(x)}(r_i),\mathbf{S}_i} &\equiv \frac{e|g_e|}{2m_e} \mathbf{B}^{(x)}(\mathbf{r}_i) \cdot \widehat{\mathbf{S}}_i , \\ \widehat{H}_{\mathbf{S}_i,\mathbf{p}_i} &\equiv \frac{e|g_e|}{2(m_e c)^2} \widehat{\mathbf{S}}_i \cdot \left[\left(\mathbf{E}^{(x)}(\mathbf{r}_i) - \frac{Ze}{4\pi\epsilon_0} \frac{\mathbf{r}_i}{r_i^3} \right) \times \widehat{\mathbf{p}}_i \right] , \\ \widehat{H}_{\mathbf{S}_i,\mathbf{p}_j} &\equiv \frac{e|g_e|}{2(m_e c)^2} \widehat{\mathbf{S}}_i \cdot \left(\frac{e}{4\pi\epsilon_0} \frac{\mathbf{r}_{ij}}{r_{ij}^3} \times \widehat{\mathbf{p}}_j \right) , \\ \widehat{H}_{\mathbf{p}_i,\mathbf{p}_j} &\equiv -\frac{\mu_0}{4\pi} \left(\frac{e|g_e|}{2m_e} \right)^2 \frac{1}{2r_{ij}} \left[\widehat{\mathbf{p}}_i \cdot \widehat{\mathbf{p}}_j + \frac{(\mathbf{r}_{ij} \cdot \widehat{\mathbf{p}}_i)(\mathbf{r}_{ij} \cdot \widehat{\mathbf{p}}_j)}{r_{ij}^2} \right] , \\ \widehat{H}_{\mathbf{S}_i,\mathbf{S}_j} &\equiv \frac{\mu_0}{4\pi} \left(\frac{e|g_e|}{2m_e} \right)^2 \left\{ -\frac{2}{3} \widehat{\mathbf{S}}_i \cdot \widehat{\mathbf{S}}_j \delta^{(3)}(\mathbf{r}_{ij}) + \frac{1}{r_{ij}^3} \left[\widehat{\mathbf{S}}_i \cdot \widehat{\mathbf{S}}_j - \frac{3(\widehat{\mathbf{S}}_i \cdot \mathbf{r}_{ij})(\widehat{\mathbf{S}}_j \cdot \mathbf{r}_{ij})}{r_{ij}^2} \right] \right\} , \end{aligned}$$

and the fields $\mathbf{E}^{(x)}$, $\mathbf{B}^{(x)}$, $\varphi^{(x)}$, and $\mathbf{A}^{(x)}$ are external. Unfortunately, even including the Coulomb operator for the electron-electron interaction makes the time-independent Schrödinger equation unsolvable analytically. Thus, from here on, we must proceed numerically.

2.2 Central Field Approximation and Configuration Interaction

The numerical procedure we follow has three basic steps:

1. A **central field approximation** (CFA): Replace the electron interaction terms with a spherically symmetric average and solve the approximate Schrödinger equation to generate an orthonormal basis (the CFA basis).

$$\left\langle \sum_{j<i} V_{ij}(r_i, r_j) \right\rangle = V_{CFA}(r_i) \quad , \quad (2.9)$$

$$\hat{H}_{CFA} |\Psi_{CFA}\rangle = E_{CFA} |\Psi_{CFA}\rangle \quad . \quad (2.10)$$

2. **Dimensional reduction**: Choose a finite subsequence of configurations (each containing its own Hilbert subspace of states) to represent the exact Hamiltonian in the CFA basis:

$$\hat{H} = \sum_{m,n} \langle \Psi_{CFA,m} | \hat{H} | \Psi_{CFA,n} \rangle | \Psi_{CFA,m} \rangle \langle \Psi_{CFA,n} | \quad . \quad (2.11)$$

3. **Configuration interaction**: Diagonalize the original Hamiltonian in the CFA basis to find the stationary states:

$$\hat{H} \sum_n C_n^k | \Psi_{CFA,n} \rangle = E^k \sum_n C_n^k | \Psi_{CFA,n} \rangle \quad . \quad (2.12)$$

The second step will be discussed in more detail in Chapter 3 and has been the focus of the present work. This and the next section will serve as a review of the first and third steps, respectively, as discussed in the existing literature.

The most accurate method of producing a CFA Hamiltonian would employ the Hartree-Fock equation for the radial part of the wavefunctions. Here, we follow the approach and notation

provided in chapters 5 and 6 of Cowan [52]:

$$\left[\frac{\hbar^2}{2m_e} \left(-\frac{d^2}{dr^2} + \frac{l_i(l_i+1)}{r^2} \right) + \frac{e^2}{4\pi\epsilon_0} \left(-\frac{Z}{r} + \sum_{j=1}^q (w_j - \delta_{ij}) \int_0^\infty \frac{dr'}{r_{>}} P_j^2(r') - (w_i - 1)A_i(r) \right) \right] P_i(r) \\ = \varepsilon_i P_i(r) + \sum_{j=1, j \neq i}^q w_j \left[\delta_{l_i l_j} \varepsilon_{ij} + \frac{e^2}{4\pi\epsilon_0} B_{ij}(r) \right] P_j(r) \quad , \quad (2.13)$$

where

$$A_i(r) = \frac{2l_i+1}{4l_i+1} \sum_{k>0} \begin{pmatrix} l_i & k & l_i \\ 0 & 0 & 0 \end{pmatrix}^2 \int_0^\infty dr' \frac{r_{<}^k}{r_{>}^{k+1}} P_i^2(r') \quad , \\ B_{ij}(r) = \frac{1}{2} \sum_{k>0} \begin{pmatrix} l_i & k & l_j \\ 0 & 0 & 0 \end{pmatrix}^2 \int_0^\infty dr' \frac{r_{<}^k}{r_{>}^{k+1}} P_i(r') P_j(r') \quad ,$$

are the electron exchange interactions from equivalent and non-equivalent electrons respectively, w_j denotes the occupation of the j 'th orbital, and $r_{<}$ and $r_{>}$ denote the lesser and greater between r and r' respectively; the coefficients that appear as 2-row 3-column matrices in the summations for A_i and B_{ij} are 3-j symbols. The ε_i and ε_{ij} come from having applied the variational method to the configuration-average energy under two constraints: that the radial wave function be normalized and that the radial wave functions of different orbitals be mutually orthogonal. Written explicitly, it is required that

$$\delta \left\{ \left\langle \widehat{H}(r) \right\rangle_{\{(n_i l_i) w_i\}} - \sum_{i=1}^q \varepsilon_i w_i \int_0^\infty dr' P_i^2(r') - \sum_{i=1}^q \sum_{j=1, j \neq i}^q \delta_{l_i l_j} \varepsilon_{ij} w_i w_j \int_0^\infty dr' P_i(r') P_j(r') \right\} = 0 \quad , \quad (2.14)$$

where the configuration-average energy is expanded as:

$$\langle \widehat{H} \rangle_{\{(n_i l_i) w_i\}} = \sum_{i=1}^q \left[\langle \widehat{H}_{K,i} \rangle_{\{(n_i l_i) w_i\}} + \langle \widehat{H}_{N,i} \rangle_{\{(n_i l_i) w_i\}} + \langle \widehat{H}_{ii} \rangle_{\{(n_i l_i) w_i\}} + \sum_{j=1, j \neq i}^q \langle \widehat{H}_{ij} \rangle_{\{(n_i l_i) w_i\}} \right] , \quad (2.15)$$

with:

$$\begin{aligned} \langle \widehat{H}_{K,i} \rangle_{\{(n_i l_i) w_i\}} &= \frac{\hbar^2}{2m_e} \int_0^\infty dr P_i(r) \left[\frac{d^2}{dr^2} - \frac{l_i(l_i+1)}{r^2} \right] P_i(r) , \\ \langle \widehat{H}_{N,i} \rangle_{\{(n_i l_i) w_i\}} &= -\frac{e^2 Z}{4\pi\epsilon_0} \int_0^\infty dr \frac{1}{r} P_i^2(r) , \\ \langle \widehat{H}_{ii} \rangle_{\{(n_i l_i) w_i\}} &= \frac{e^2}{4\pi\epsilon_0} \left[F_{ii}^0 - \frac{2l_i+1}{4l_i+1} \sum_{k>0} \begin{pmatrix} l_i & k & l_i \\ 0 & 0 & 0 \end{pmatrix}^2 F_{ii}^k \right] , \\ \langle \widehat{H}_{ij} \rangle_{\{(n_i l_i) w_i\}} &= \frac{e^2}{4\pi\epsilon_0} \left[F_{ij}^0 - \frac{1}{2} \sum_{k>0} \begin{pmatrix} l_i & k & l_j \\ 0 & 0 & 0 \end{pmatrix}^2 G_{ij}^k \right] , \end{aligned}$$

and

$$\begin{aligned} F_{ij}^k &= \int_0^\infty dr \int_0^\infty dr' \frac{r_{<}^k}{r_{>}^{k+1}} P_i^2(r) P_j^2(r') , \\ G_{ij}^k &= \int_0^\infty dr \int_0^\infty dr' \frac{r_{<}^k}{r_{>}^{k+1}} P_i(r) P_j(r') P_j(r) P_i(r') , \end{aligned}$$

are the Slater integrals. The radial wave functions P_i must satisfy the boundary conditions:

$$P_i(0) = 0 , \quad (2.16)$$

$$\lim_{r \rightarrow \infty} P_i(r) = 0 . \quad (2.17)$$

Traditionally, if one were to use the complete Hartree-Fock equation to acquire a CFA basis, the rough outline of the procedure would be:

1. Start with trial radial functions $P_i^{(0)}(r)$ that satisfy the boundary conditions (2.17).
2. Compute the integrals in (2.13) and estimate the value of the ε_{ij} .
3. For each i , use (2.13) to find a new $P_i(r)$.

These steps would then be repeated until the output of step 3 agrees with, to within a prescribed tolerance, the input functions used to compute the central field. Therefore, this approach is usually referred to as the self-consistent method (SCF), which can be computationally expensive, depending on the complexity of the system of interest. Additionally, the SCF method using the full Hartree-Fock equation (often referred to as the HF method) runs into divergences in certain special cases (e.g. excited d and f orbitals for transition and rare-earth elements) which have to be accounted for by a specifically chosen numerical procedure outlined by Cowan in Chapter 7, Section 6 [52].

The divergences, as well as a significant amount of the computational expense, arise from the inhomogeneous terms on the right-hand side of (2.13). With this in mind, it is common to approximate the full Hartree-Fock equations with a homogeneous differential equation of the form:

$$\left[\frac{\hbar}{2m_e} \left(-\frac{d^2}{dr^2} + \frac{l_i(l_i + 1)}{r^2} \right) + V^i(r) \right] P_i(r) = \varepsilon_i P_i(r) \quad , \quad (2.18)$$

AUTOSTRUCTURE [61, 62] uses two such methods to produce a CFA Hamiltonian. The first method is closely related to the Hartree-Fock equation. If the Hartree potential is defined as:

$$V_H = \frac{e^2}{4\pi\epsilon_0} \sum_{j=1}^q (w_j - \delta_{ij}) \int_0^\infty \frac{dr'}{r'} P_j^2(r') \quad , \quad (2.19)$$

then the Hartree method is to use a CFA Hamiltonian of the form:

$$\left[\frac{\hbar}{2m_e} \left(-\frac{d^2}{dr^2} + \frac{l_i(l_i + 1)}{r^2} \right) - \frac{e^2 Z}{4\pi\epsilon_0 r} + V_H(r) \right] P_i(r) = \varepsilon_i P_i(r) \quad . \quad (2.20)$$

This Hamiltonian is far simpler and does not account for the exchange interaction with all of the other electrons or the electron's self energy. A simple improvement is to use a statistical correction

to account for exchange interactions (Hartree plus exchange):

$$V_X = -k_X f(r) \frac{\rho'}{\rho' + 0.5/(n_i - l_i)} \frac{\rho'}{\rho} \left(\frac{24\rho}{\pi} \right)^{3/2}, \quad (2.21)$$

where $\rho'(r) = \rho(r) - \min(2, w_i)\rho_i(r)$ is the electron density excluding the self exchange-effects, k_X is set to the value that gives the best agreement with HF (≈ 0.65), and $f(r)$ is a modification factor to replace the Lagrange multipliers ε_{ij} . Arranging the P_i in order of decreasing ε_i , letting k be the number of orbitals with $l = l_i$ and $n < n_i$, and r_0 be the location of the k_{th} node, the modification factor is defined as:

$$f(r) = \begin{cases} 1 & r \geq r_0 \\ 1 + 0.7 \left(1 - \frac{r}{r_0}\right) & r < r_0 \end{cases}, \quad (2.22)$$

when either (a) $l_{i-1} = l_i > 1$ or (b) $l_{i-2} = l_i > 1$ and $w_{i-1} = 1$; $f(r) = 1$ otherwise. Then the HX Hamiltonian has the form:

$$\left[\frac{\hbar}{2m_e} \left(-\frac{d^2}{dr^2} + \frac{l_i(l_i + 1)}{r^2} \right) - \frac{e^2 Z}{4\pi\epsilon_0 r} + V_H(r) + V_X(r) \right] P_i(r) = \varepsilon_i P_i(r) \quad . \quad (2.23)$$

Since the Hartree potential involves an integral over all other electron orbitals, it is still in principle necessary to treat this as a SCF method. However, since the configuration-average energies are fairly well approximated with a small number of iterations in most cases, AUTOSTRUCTURE neglects the full SCF iteration by default and allows the user to decide whether to implement it.

The second method used to implement a CFA is the lesser known Thomas-Fermi-Dirac-Amaldi method (TFDA). This approach uses the semi-classical approximation of an electron gas in the presence of a nuclear potential with an exchange correction, as in the Thomas-Fermi-Dirac model, but with dipole and quadrupole corrections. Assuming a maximum occupied radius of r_0 ,

the total energy is calculated as:

$$E_{TFDA} = \int_0^{r_0} dr 4\pi r^2 \rho(r) \left[\frac{\hbar^2}{2m_e} \left(\frac{3(3\pi)^{2/3}}{5} \rho(r)^{2/3} - \frac{3}{2} \left(\frac{3}{\pi} \right)^{1/3} \rho(r)^{1/3} \right) + V_{TFDA}(r) \right] \quad , (2.24)$$

with:

$$V_{TFDA}(r) = \frac{e^2}{4\pi\epsilon_0} \left[-\frac{Z}{r} + \int_0^{r_0} dr' 4\pi r' \rho(r') \left(\frac{1}{r_{>}} + \lambda_d \frac{r_{<}}{r_{>}^2} + \lambda_q \frac{r_{<}^2}{r_{>}^3} \right) \right] \quad .$$

The total energy is optimized under the constraint that the density integrated over the volume equals the total number of particles. With V_0 as a Lagrange multiplier, it is required that:

$$\delta \left[E_{TFDA} - V_0 \int_0^\infty dr 4\pi r^2 \rho(r) \right] = 0 \quad . \quad (2.25)$$

This leads to the relation:

$$\frac{\hbar^2}{2m_e} \left[(3\pi^2 \rho(r))^{2/3} + \frac{2}{\pi} (3\pi^2 \rho(r))^{1/3} \right] + V_{TFDA}(r) - V_0 = 0 \quad . \quad (2.26)$$

Since the potential in this treatment is static, it also satisfies Poisson's equation:

$$\frac{1}{r} \frac{d^2}{dr^2} \left[r \left(\frac{1}{\pi^2} + V_0 - V(r) \right) \right] = \frac{e\rho(r)}{\epsilon_0} \quad . \quad (2.27)$$

The potential is determined from these equations and the boundary conditions:

$$\left. \frac{d^2}{dr^2} (rV(r)) \right|_{r=r_0} = 0 \quad , \quad (2.28)$$

$$\left. -rV(r) \right|_{r=0} = \frac{e^2 Z}{\epsilon_0} \quad . \quad (2.29)$$

Once the potential is determined, the states can be extracted from the Schrödinger equation with the TFDA potential.

Finally, for either the Hartree or TFDA methods, AUTOSTRUCTURE allows the user to specify scaling parameters to each orbital function which can be used variationally to improve the starting CFA basis. This option can be thought of as an alternative to carrying out the full SCF iteration; by varying extra parameters to minimize the configuration-average energies, we save some computational expense while staying within the variational formalism.

2.3 Rules for Configuration Mixing

For a time-independent Hamiltonian, the evolution of an arbitrary state can be given by the following Taylor expansion:

$$|\psi(t)\rangle = e^{-i\hat{H}t/\hbar} |\psi(0)\rangle = \left\{ \hat{1} + \left(\frac{-it}{\hbar} \hat{H} \right) + \frac{1}{2} \left(\frac{-it}{\hbar} \hat{H} \right)^2 + \dots \right\} |\psi(0)\rangle \quad .$$

With this in mind, we can say that two configurations **mix** if there are nonzero off-diagonal elements of the Hamiltonian in rows corresponding to an initial configuration and columns corresponding to a final configuration. Using the general form of the Hamiltonian for an ion, we can derive **selection rules** for which configurations mix. Here we follow Cowan's reasoning in Chapter 13 of his book [52]. The general form of the Hamiltonian is (2.8) without external fields. Since every operator is symmetric under spatial inversion, configurations can only mix if they have the same parity. We can also see that the Hamiltonian consists of only one- and two-electron operators. This means that configurations with more than two electrons in different orbitals cannot mix. Finally, the Hamiltonian commutes with the total spin and orbital angular momentum operators:

$$\left[\widehat{L}^2, \widehat{H} \right] = 0 \quad , \quad (2.30)$$

$$\left[\widehat{S}^2, \widehat{H} \right] = 0 \quad . \quad (2.31)$$

Thus we can say that two configurations that mix must have:

1. The same parity.

2. No more than two electrons in different orbitals.
3. At least one LS term in common.

AUTOSTRUCTURE makes use of these rules to save time in computing trivial elements of the Hamiltonian matrix.

Additionally, one can justify two **propensity rules** that turn out to be far more significant for the present work. First, configuration mixing is most prominent when the off-diagonal Hamiltonian elements are large compared to the difference in configuration-average energies. In other words, configurations near in energy are more likely to mix than otherwise. Second, the radial wave functions belonging to a given pair of configurations have the maximum overlap when they share the same principle quantum numbers, $\{n_i\}$. As introduced by Layzer [71], subsets of configurations that share a common number of electrons in each n -shell are referred to as a **configuration complex**. A simple example is the lowest energy complex for a 5 electron ion: $1s^2 2s^2 2p$, $1s^2 2s 2p^2$, $1s^2 2p^3$ which we will denote using the supershell notation of [57] similar to [72], $[1]^2[2]^3$. Thus, we can say that two configurations are likely to mix if they are either:

1. Near in energy
or
2. Within the same configuration complex.

2.4 Minimal Assumption

There remains a practical issue to be considered before proceeding numerically. In order to diagonalize the unapproximated Hamiltonian as described in the third step of our procedure, we must take into consideration the finite memory of a computer. Numerical configuration interaction in the context of infinite dimensional Hilbert spaces can only be justified if we assume that the Hamiltonian can be approximated by truncating at some highest energy state and still retain reasonably accurate eigenenergies.

To expand on this idea, we first consider the case of an eigenstate of the original Hamiltonian. In this case, there are no off-diagonal elements, which results in an energy variance of zero:

$$\begin{aligned}\widehat{H} |\psi(0)\rangle = E |\psi(0)\rangle &\implies |\psi(t)\rangle = e^{-iEt/\hbar} |\psi(0)\rangle \quad , \\ &\& \langle \psi | \widehat{H}^2 | \psi \rangle - \left(\langle \psi | \widehat{H} | \psi \rangle \right)^2 = E^2 - E^2 = 0 \quad .\end{aligned}$$

A good basis for numerical configuration interaction is one in which the energy variance of the state tends towards zero as the average energy becomes large:

$$\langle i | \widehat{H} | i \rangle \rightarrow \infty \implies \sum_j \langle i | \widehat{H} | j \rangle \langle j | \widehat{H} | i \rangle - \left(\langle i | \widehat{H} | i \rangle \right)^2 \rightarrow 0 \quad .$$

This may be too strong an assumption to make, since this would be neglecting transitions between states that belong to the same configuration above a certain energy. Likewise, following from the second propensity rule, we expect that transitions between configurations that belong to the same complex cannot usually be neglected. Thus our minimal assumption must be that the matrix element between configurations belonging to different complexes tends towards zero as the average energy of the complex becomes large:

$$\sum_{i \in C} \langle i | \widehat{H} | i \rangle \rightarrow \infty \implies \sum_{i \in C} \left(\sum_j \langle i | \widehat{H} | j \rangle \langle j | \widehat{H} | i \rangle \right) - \left(\langle i | \widehat{H} | i \rangle \right)^2 = \sum_{i \in C} \sum_{j \notin C} \langle i | \widehat{H} | j \rangle \langle j | \widehat{H} | i \rangle \rightarrow 0 \quad . \quad (2.32)$$

This result is equivalent to the assumption that the Hamiltonian matrix is (to a good approximation) block diagonal, and that the highest energy blocks correspond at most to the configuration complexes.

Chapter 3

A Decision Tree Learning Algorithm

Calculating the energy levels of the unapproximated Hamiltonian requires a linear combination of the non-stationary CFA states. Although the CFA Hilbert space is infinite dimensional, with the finite memory of a CPU we can only hope to represent a finite dimensional subspace. With this in mind, we seek an algorithmic method to strategically truncate the Hilbert space such that the remaining subspace balances both accuracy and memory usage, i.e. we seek a dimensional reduction algorithm. At minimum, we assume that the Hamiltonian must be block diagonal in the CFA basis so that the highest energy blocks correspond exactly to transitions within a configuration complex. Thus, high energy complexes can be treated separately and we can focus on finding the lowest energy block of the Hamiltonian.

To illustrate the difficulty, we will consider the example of C^{2+} . Suppose that we used a naive algorithm that chooses only the first few Rydberg sequences: $1s^22s^2nl$, $1s^22s2pnl$, and $1s^22p^2nl$. If this was a good selection of configurations then we should see consistent convergence to experimentally measured energies when we increment the maximum n -shell but, as can be clearly seen in Figure 3.1, the average difference with the experimentally measured energies actually grows as a function of the maximum n -shell. Therefore, we cannot expect that increasing the maximum n -shell will always improve the accuracy of the calculated energy levels. Without carefully selecting the configuration sequence, the calculated stationary energies can easily veer away from the experimentally observe values.

3.1 Tree Data Structures

The first challenge is to probe the set of all possible configurations up to a maximum n -shell in a memory efficient way. We can treat each configuration as a dictionary whose keys are the

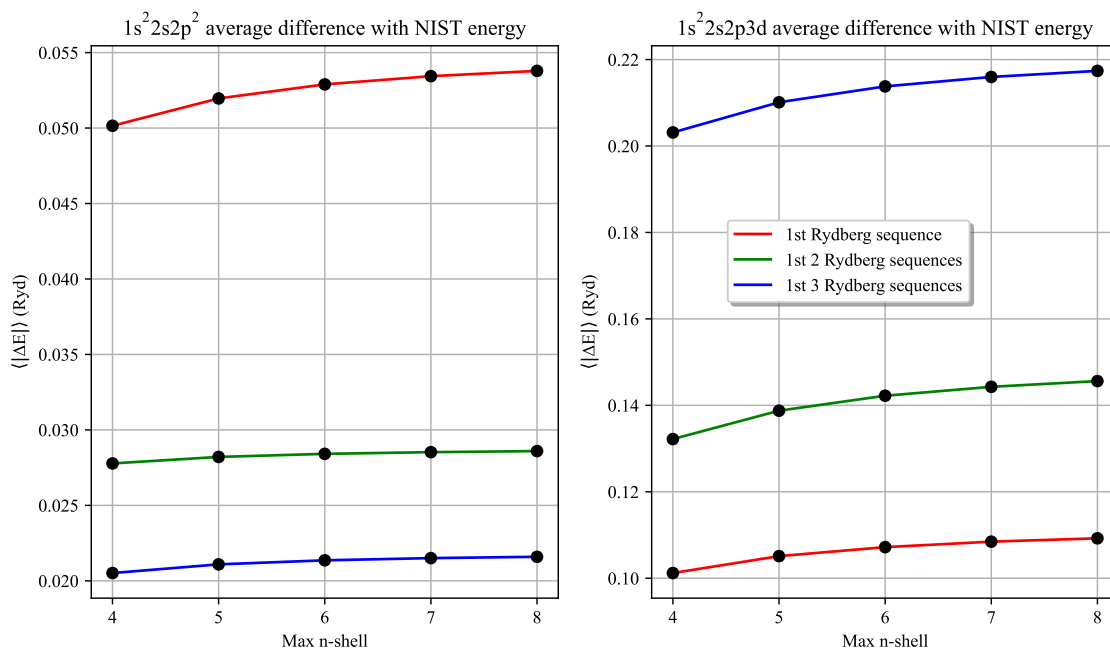


Figure 3.1: The calculated energy difference with NIST averaged over a configuration for the configurations $1s^2 2s 2p^2$ (left) and $1s^2 2s 2p 3d$ (right) for C^{2+} as a function of the maximum n -shell when including only the first few Rydberg sequences ($1s^2 2s^2 nl$, $1s^2 2s 2p nl$, and $1s^2 2p^2 nl$). The red lines are the average differences when using only the first Rydberg sequence, the green lines are those calculated when using the first two Rydberg sequences and the blue lines are those calculated when using the first three Rydberg sequences.

(n, l) tuples specifying an orbital and whose values are the corresponding occupation numbers. A naive probing algorithm would generate each configuration sequentially. To motivate what follows, let's first consider the time complexity $\mathcal{T}_{\text{naive}}$ of such a naive algorithm as a function of the number of orbitals, N_{orb} , and the number of electrons, N_e . Neglecting the maximum occupancy of each orbital, the number of possible configurations generated by permuting all electrons in the ion up to a maximum n -shell goes roughly as $\binom{N_{\text{orb}}+N_e}{N_e}$. And if we have that $N_{\text{orb}} \gg 1$, then this can be simplified further:

$$\binom{N_{\text{orb}} + N_e}{N_e} = \frac{1}{N_e!} \prod_{k=1}^{N_e} (N_{\text{orb}} + k) \approx \frac{(N_{\text{orb}})^{N_e}}{N_e!} . \quad (3.1)$$

Since the number of entries in each dictionary is the same as the number of orbitals, the time complexity $\mathcal{T}_{\text{naive}}$ of the naive probing algorithm should then go as the product of the number of orbitals and the number of possible configurations. Thus we can say that:

$$\mathcal{T}_{\text{naive}}(N_{\text{orb}}, N_e) = O\left(\frac{(N_{\text{orb}})^{N_e+1}}{N_e!}\right) . \quad (3.2)$$

We can improve on this approach by considering a nonlinear data structure. A **tree data structure** satisfies the definition of a tree in graph theory: an undirected connected graph with a unique path connecting any pair of nodes (i.e no cycles). In computation, one typically assigns some value to each node and arranges the tree into **levels** such that a given node has one **parent node** at the previous level and **children nodes** at the next level. The one exception is the **root node** at the zeroth level which has no parents. We refer to the total number of levels as the **depth** of the tree. One could intuit that arranging the configuration sequence into a tree data structure, where each level corresponds to an orbital, would reduce the time complexity of listing out each configuration individually, but for clarity we will show this concept in more explicit detail.

A tree data structure arises naturally when partitioning a configuration sequence into Rydberg sequences. As an example, for a 4-electron system, the first three Rydberg sequences would usually be denoted as $1s^2 2s \, nl$, $1s^2 2p \, nl$, and $1s^2 3s \, nl$. These sequences can be more compactly identified

as sets of 3-electron configurations that have a common **configuration prefix**: $1s^22s$, $1s^22p$, and $1s^23s$ respectively. These 3-electron prefixes are all part of the more general sequence $1s^2 nl n'l'$, which corresponds to the one-orbital prefix $1s^2$. Since configuration prefixes are a natural way to partition the set of possible configurations that is close to the familiar notation, and we want the levels of the tree to correspond to orbitals, a natural first guess for what values to assign to the nodes would be the occupation numbers for each orbital. It happens that there are problems with such a direct assignment for the value at each node. Firstly, we will encounter a problem when trying to place the first entries in each of the respective Rydberg sequences: $1s^22s^2$, $1s^22p^2$, and $1s^23s^2$. Intuitively, these configurations belong on the same branch as their single excitation counterparts, yet they have a different two-orbital prefix. Another problem arises when trying to place the remaining one-orbital prefixes ($1s^1$ and $1s^0$) in separate branches. If the root node on the tree corresponds to the $1s$ orbital, and we insist that the value of the nodes are occupation numbers, then we would need to make three different trees.

The solution to this problem is to make a change of variables. We let the value at each node, X_{nd} , be the number of electrons occupying orbitals subsequent to the parent node's associated orbital:

$$X_{nd} = \sum_{(n,l)=(n_{nd},l_{nd})}^{(n_{\max},l_{\max})} \Xi_{(n,l)} \quad . \quad (3.3)$$

An appropriate name for this quantity is the **remnant occupation**, or the **remnant** for short. Given a prefix with $N_{e,\text{pfx}}$ electrons in an ion with N_e total electrons, we can say that there is a remnant of $N_e - N_{e,\text{pfx}}$ electrons occupying the remaining orbitals. Since the root node has no parent, its value will always be the total number of electrons in the ion. To recover the occupation number at a given parent node, we can simply subtract the value of one of the child nodes from that of the parent node:

$$\Xi_{(n_{\text{pt}},l_{\text{pt}})} = X_{\text{pt}} - X_{\text{cd}} \quad , \quad (3.4)$$

where Ξ_{pt} is the occupation at the parent node and X_{pt} and X_{cd} are the values of the parent and child respectively. A configuration prefix can then be reconstructed by repeating this procedure at each preceding level until we reach the root node.

This change of variables makes it straightforward to arrange the node values in consecutive order so that they can easily be generated by a for-loop. From (3.4), we can see that the minimum remnant that can be assigned to a child node depends on the maximum occupation number of the parent node, $\Xi_{\text{pt,max}} = 4l_{\text{pt}} + 2$. Since it must also be nonnegative, the minimum value for a given child node can be defined as:

$$X_{\text{cd,min}} \equiv \max(0, X_{\text{pt}} - \Xi_{\text{pt,max}}) \quad . \quad (3.5)$$

Similarly, the maximum remnant that can be assigned to a child node depends on the maximum occupation numbers of all remaining orbitals and also cannot exceed the value of the parent. Thus the maximum value for a given child node can be defined as:

$$X_{\text{cd,max}} \equiv \min\left(X_{\text{pt}}, \sum_{(n,l)=(n_{\text{cd}},l_{\text{cd}})}^{(n_{\text{max}},l_{\text{max}})} \Xi_{(n,l),\text{max}}\right) \quad . \quad (3.6)$$

From here on we refer to this tree as the **configuration tree**. An example for an ion with four-electrons is shown in Figure 3.2.

We can consider the time complexity at this stage by estimating the total number of nodes in the tree. Since each level in the tree corresponds to an orbital, the number of nodes up to a given level in the tree is the same as the number of possible configurations generated by permuting all electrons in the ion up to the level's corresponding orbital. In that case, we can use our estimation (3.1) and sum over the number of orbitals. If $\mathcal{T}_{\text{tree}}$ is the time complexity of an algorithm that generates the tree, this goes as:

$$\mathcal{T}_{\text{tree}} \sim O\left(\frac{1}{N_{\text{e}}!} \sum_{N=0}^{N_{\text{orb}}} N^{N_{\text{e}}}\right) \sim O\left(\frac{(N_{\text{orb}})^{N_{\text{e}}+1}}{(N_{\text{e}} + 1)!}\right) \quad . \quad (3.7)$$

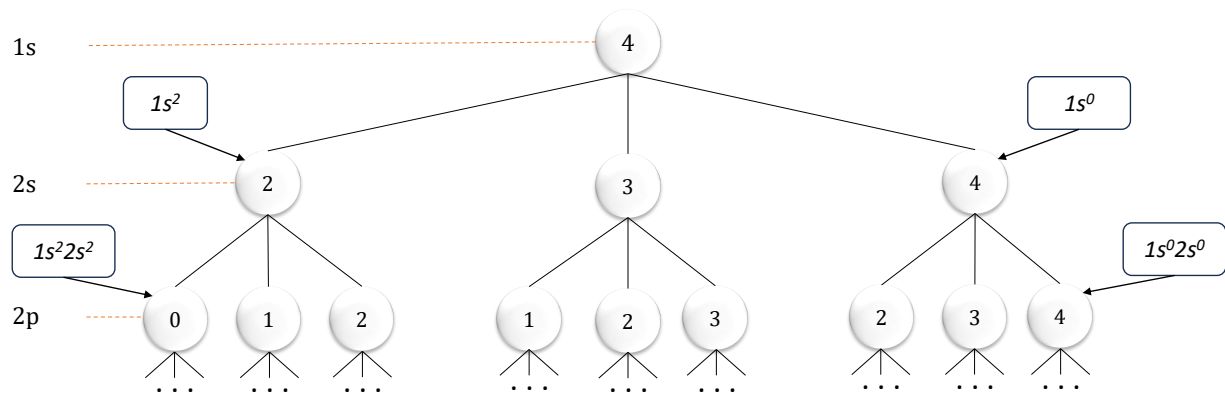


Figure 3.2: The first three levels of a configuration tree for a 4-electron system. Prefixes are shown for two extremes: the ground configuration is on the left-most branch and the highest energy configuration prefixes can be found on the right-most branch.

The power of leading order in N_{orb} remains the same, but we now divide by an extra factor of $N_e + 1$. This result is a slight improvement, but we will find that we can reduce the time complexity to the order of $N_{\text{orb}}^{N_{e,\text{vlc}}}$, where $N_{e,\text{vlc}}$ is the number of electrons in the valence n -shell, once we take advantage of this new data structure by incorporating a decision tree algorithm.

3.2 The Complex Resolved Ion Spectroscopy Tree Algorithm (CRISTAL)

All machine learning algorithms require a cost function to minimize. In this case, the cost function should quantify the accuracy of calculated energy levels. We can minimize either the average difference from measured energy levels with the L^1 norm, or the average square difference with the L^2 norm. Choosing between the L^1 and L^2 norms is challenging since both have comparable time complexity and have various pros and cons for convergence. For the first ions calculated, we have opted to use the L^1 norm, though these results should be compared with those using the L^2 norm in the future. Since we ultimately want accurate DR rates, and we know that configurations near in energy are likely to mix, we should pick representative configurations from the single and

double excitation Rydberg sequences near to the ionization threshold. From the first selection rule, we also know that configurations that mix must have the same parity. Thus, our cost function is calculated with one even and one odd representative configuration from both the single excitation Rydberg sequence and the first double excitation Rydberg sequence. For example, for O^{3+} the chosen representative configurations are $1s^2 2s^2 5f$, $1s^2 2s^2 5g$, $1s^2 2s 2p 4d$, and $1s^2 2s 2p 5p$. We can define a **degradation** by subtracting the cost function evaluated at the current step from its value at some previous step, which we will call the **degradation reference**. The degradation reference begins as the initial value of the cost function, and is updated to the current value of the cost function any time the degradation is negative. To avoid over-fitting within a maximum n -shell, we set a degradation threshold. We will say that the energy levels have degraded *if and only if* the degradation exceeds the threshold. The threshold used for the Boron-like isoelectronic sequence was 0.0004 Rydbergs.

At this stage we can begin optimizing the selected configuration sequence by systematically pruning branches of the tree. We can use the rules for configuration mixing discussed in Section 2.3 to justify some guiding principles. First, we will need to add some structure to the tree. According to the second propensity rule, configurations are likely to mix within a configuration complex. We can group the configurations into complexes by simply adding a layer to the configuration tree, which we will call the **complex tree**. To distinguish the two kinds of nodes, we will refer to nodes in the configuration tree as **orbital nodes** and nodes in the complex tree as **shell nodes**. Both layers can be generated simultaneously. Each shell node is given the value of an orbital node corresponding to the s orbital of its n -shell, and the two nodes are connected to one another by a two-way link. Orbital nodes that do not correspond to an s orbital are connected by a one-way link to the shell node of their parent. An example of a complex tree for a 4-electron ion is shown in Figure 3.3.

Now that the nodes are appropriately grouped so that no remaining complexes will be incomplete, we can begin deriving a decision tree algorithm to strategically prune the branches, which we have named the **Complex Resolved Ion Spectroscopy Tree Algorithm** (CRISTAL). From the

Example: 4 electrons, shell nodes

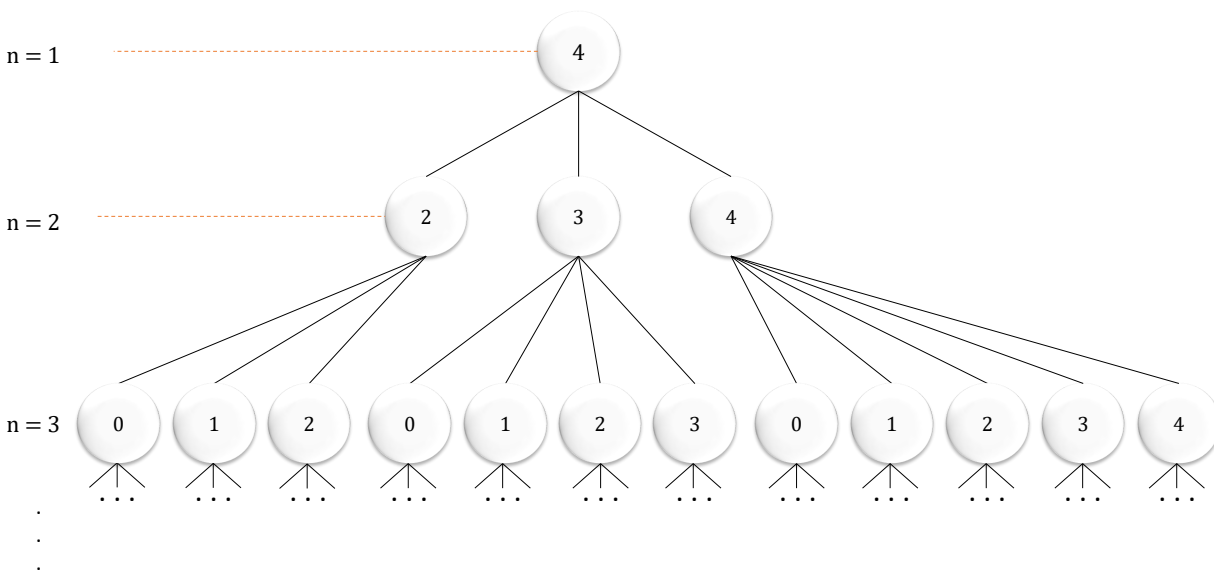


Figure 3.3: Caption: The first three levels of the complex tree for a 4-electron ion.

1st propensity rule, we know that two configurations are likely to mix if they are near in energy and, by our minimal assumption, we expect that complexes that have a large average energy will also have a negligible average transition rate. In other words, mixing with complexes that are high in average energy can be assumed to be negligible. Thus, as our first guiding principle, *the safest complexes to remove will be those highest in energy*. Making this choice means that the first shell node to check should be that corresponding to the complex prefix $[1]^0$.

Recalling the previous chapter, since we are seeking the lowest energy block of the Hamiltonian, we can assume that there exists a mixing boundary in quantum number separating the complexes that contribute to this block from those that do not. Beneath this mixing boundary, all complexes should be included. Thus we have our second guiding principle: *the remaining configuration sequence should be complete within a mixing boundary*. Therefore, if the calculated energy levels degrade when removing a shell node, it will be restored and the next node to check should be its highest value child (Figure 3.4 (A)). If the restored node has no children, i.e. it is at the current maximum n -shell, this is a terminating case (Figure 3.4 (B)). If the calculated energies do not

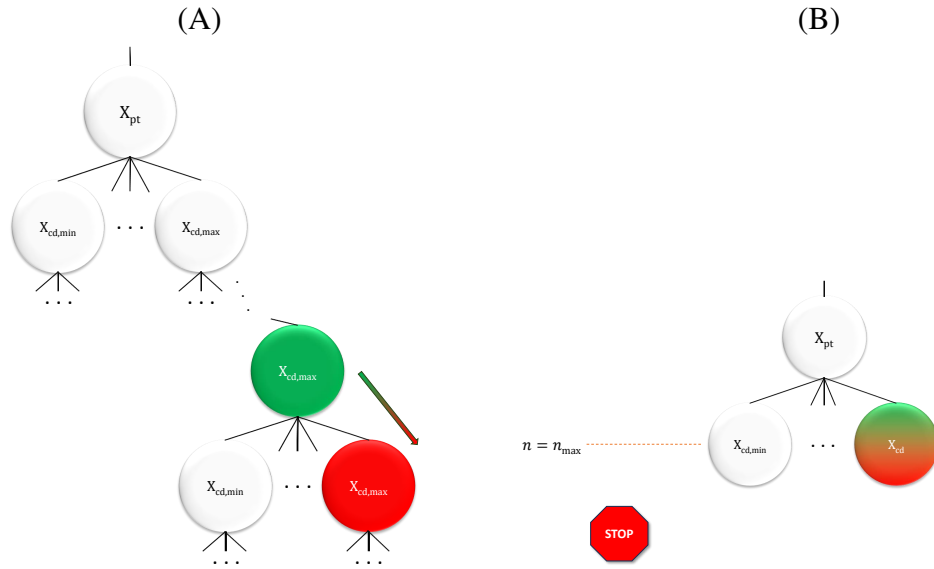


Figure 3.4: (A) Degraded = True, basic case. (B) Degraded = True, basic terminating case.

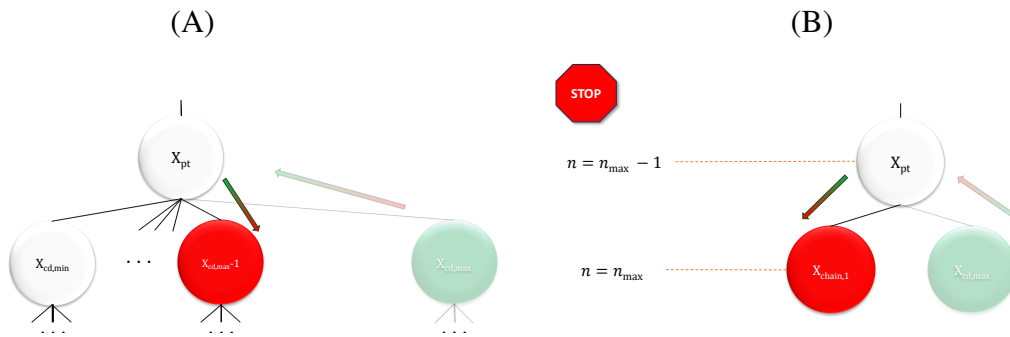


Figure 3.5: (A) Degraded = False, basic case. (B) Degraded = False, basic terminating case.

degrade, the shell node is pruned successfully and the next node to check is the sibling node with the highest value (Figure 3.5 (A)).

The final guiding principle has to do with the fact that we want navigation on the tree to be straightforward in the sense that we can assume that all remaining branches reach the maximum n -shell. More succinctly, we *disallow short branches to avoid navigation errors*. Thus, if a node is successfully pruned and there is only one remaining sibling node that is at the maximum n -shell (which we will often refer to as n_{max}), this node is selected (but not pruned) and the algorithm terminates within the current max n -shell (Figure 3.5 (B)).

This guiding principle is also important for the case when we encounter a **chain** of nodes, i.e. a sequence of nodes for which the k_{th} node is the only child of the $(k - 1)_{th}$ node (Figure 3.6). If

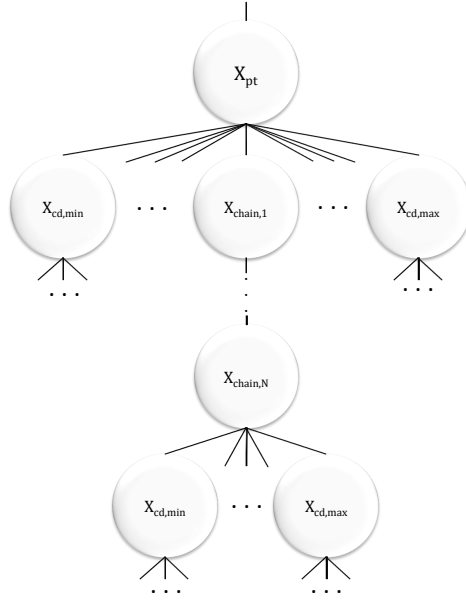


Figure 3.6: A general chain of nodes of length N .

a restored node is the first in a chain that terminates before the maximum n -shell, the next node to check should be the highest value child of the last node in the chain (Figure 3.7 (A)). If the chain reaches the maximum n -shell, this is a terminating case (Figure 3.7 (B)). There are two ways a chain can be encountered when a node is successfully removed. The first can be thought of as a generalization of the basic terminating case shown in Figure 3.5 (B). When a successfully removed node has only one sibling, the parent is now the first node in a chain. If this newly created chain terminates before reaching n_{max} , then we select the highest value child of the last node in the chain (Figure 3.8 (A)). If the created chain reaches n_{max} , the last node in the chain is selected, but not pruned, and the algorithm terminates within the current max n -shell (Figure 3.8 (B)). The second way a chain can be encountered when a node is successfully removed is in the case of a preexisting chain. In this case, the first node of the chain is the sibling node of the node that was successfully removed, and we can try pruning this node without leaving any short branches (Figure 3.8 (C)).

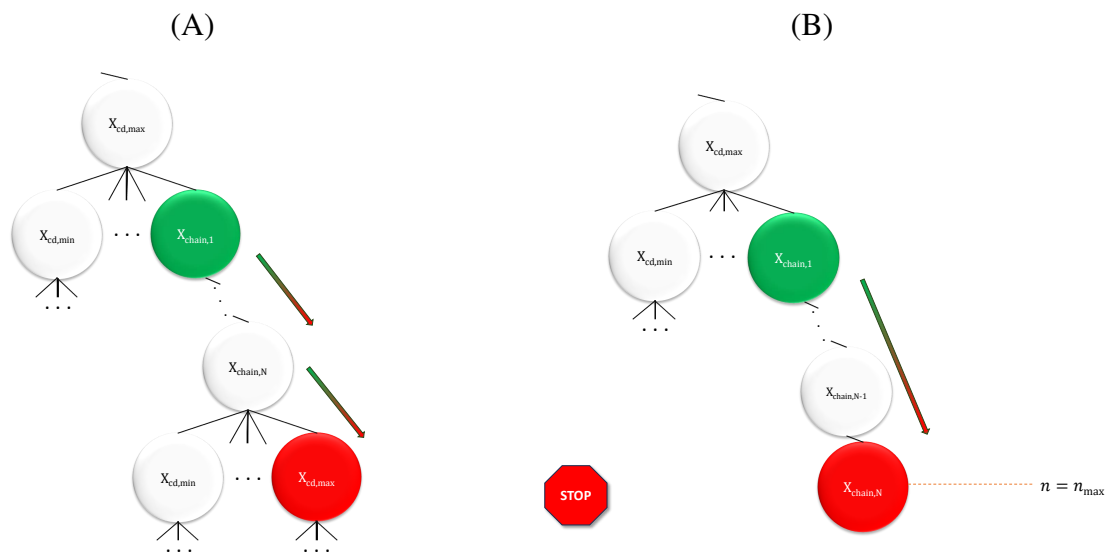


Figure 3.7: (A) Degraded = True, partial chain. (B) Degraded = True, chain reaches n_{max} .

To summarize the guiding principles:

1. The highest energy complexes are the safest to remove. Begin with the highest value child of the root node (prefix $[1]^0$).
2. The remaining configuration sequence should be complete within a mixing boundary in quantum number space.
3. All remaining branches must extend to n_{max} to avoid navigation errors.

In Figure 3.9, it is shown that all of the cases discussed will either feed into each other or feed into a terminating case, so CRISTAL is closed within the current max n -shell, i.e. it will halt with no navigation errors.

Once CRISTAL reaches some terminating case, the maximum n -shell is incremented and the remaining branches of configuration and complex trees are grown to probe the new set of available configurations. In all of the terminating cases at the previous max n -shell, the selected node has either already been checked and restored (Figure 3.4 (B)) or is part of a chain and must be kept (Figures 3.5 (B), 3.7 (B), and 3.8 (B)). Thus, we can effectively treat the starting case at the next max n -shell as a case where degraded = True and then let CRISTAL continue as it would otherwise.

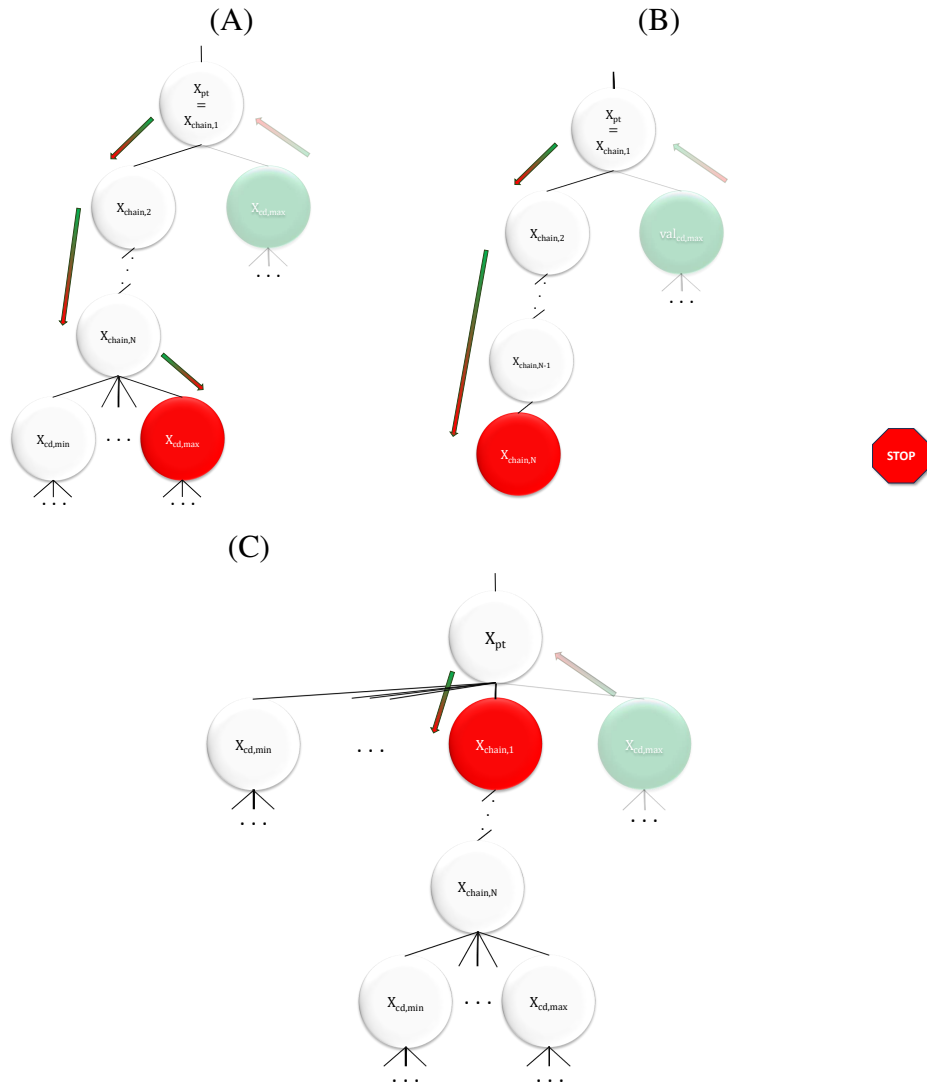


Figure 3.8: (A) Degraded = False, partial chain created. (B) Degraded = False, created chain reaches n_{max} . (C) Degraded = False, pre-existing chain.

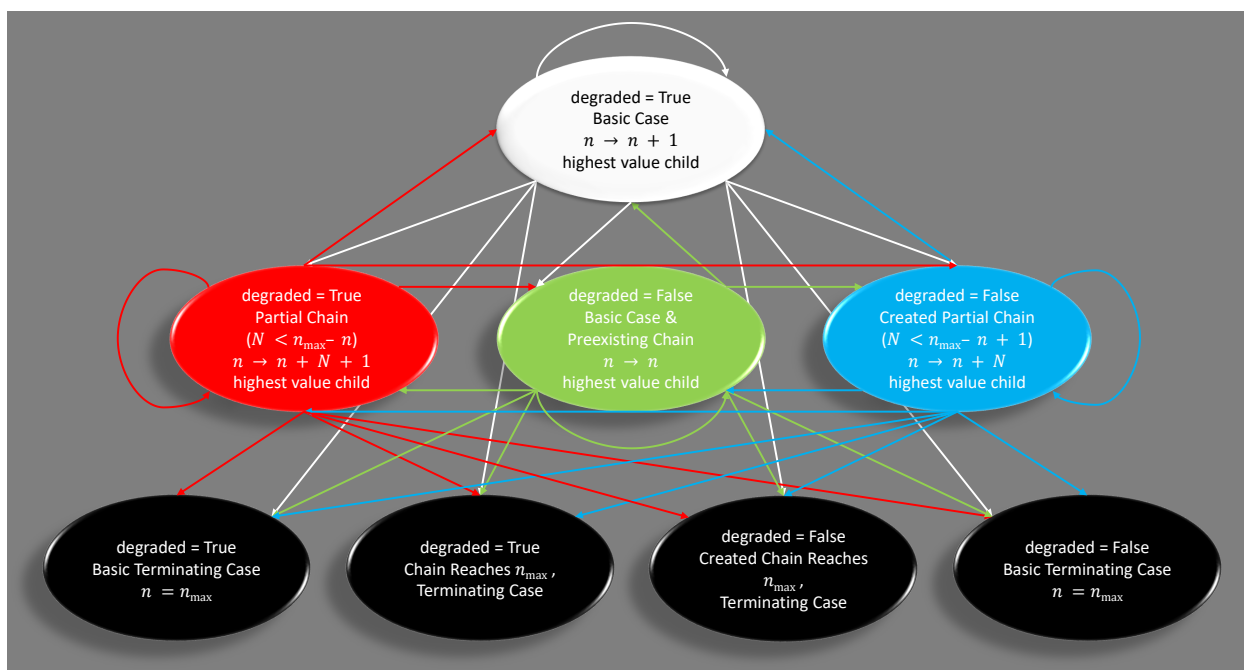


Figure 3.9: A graph demonstrating the closure of CRISTAL within a given n_{\max} , i.e. the algorithm will terminate at a node at the bottom level of the tree (which corresponds to the current value of n_{\max}) without any navigation errors.

If the degradation is positive when incrementing the max n -shell, we should take this to mean that CRISTAL must be reset with a lower degradation threshold.

Finally, if CRISTAL is at the maximum n -shell and the remnant is 0, then all subsequent child nodes from this node on will also have a value of 0. CRISTAL cannot remove any of the nodes in this chain without creating a short branch, so we consider the algorithm to be converged in this case. The general flowchart summarizing CRISTAL can be seen in Figure 3.10.

3.3 Truncation functions and decision forests

There is one remaining practical issue: at the zeroth iteration (before any pruning has taken place), the representative configurations will typically require a starting n_{\max} that allows too many configurations. For example, using the previously mentioned representative configurations for O^{3+} ($1s^22s^25f$, $1s^22s^25g$, $1s^22s2p4d$, and $1s^22s2p5p$), the starting max n -shell cannot be lower than $n = 5$. But, without any pruning, 11,028 configurations will be generated by permuting all electrons

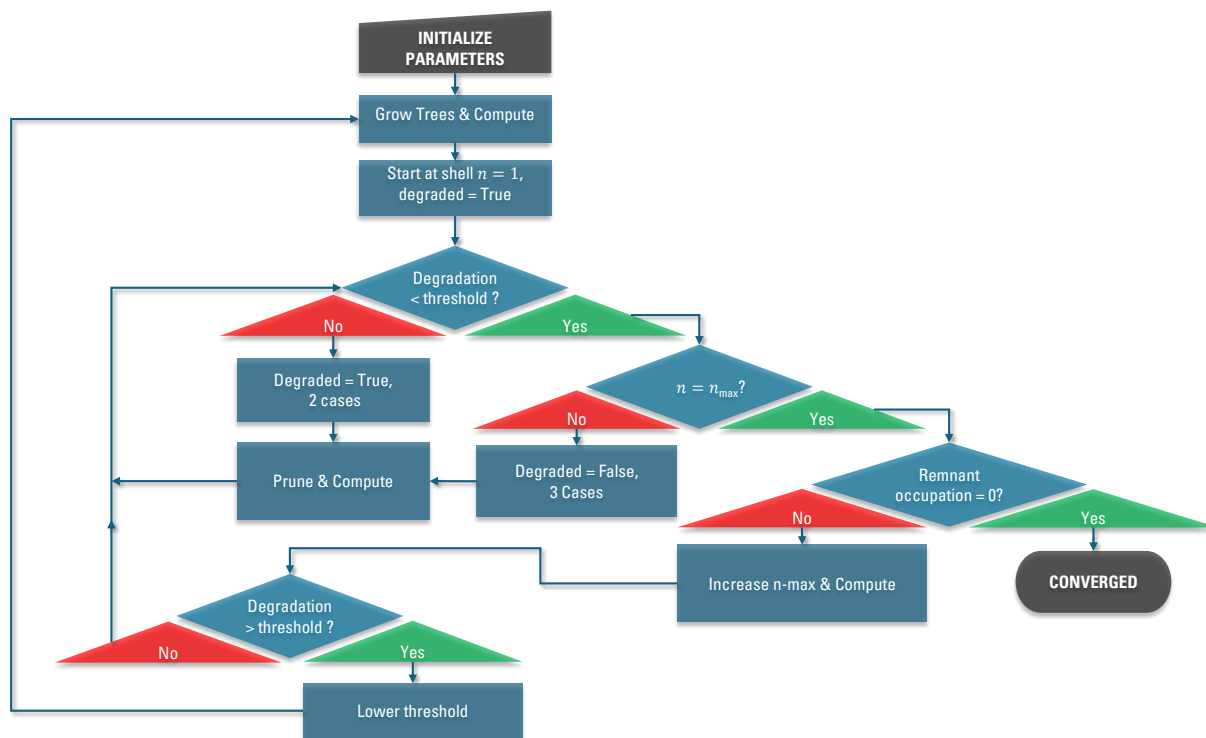


Figure 3.10: A detailed flowchart that illustrates the complete operation of CRISTAL beginning with the initialization of the parameters (such as the total number of electrons, the proton number, the representative configurations, and the starting n_{\max}) and terminating at its criterion for convergence.

in the ion. This means that the number of elements in the Hamiltonian will be roughly on the order of $(10 \cdot 10^4)^2 = 10^{10}$. We can save a great deal of time by making an initial guess at the form of the mixing boundary. We define a **truncation function** as a function of the quantum numbers of a configuration that must evaluate to a number below a set maximum in order for a configuration to be included at the zeroth iteration. The simplest possible guess at truncation function is the total n for all electrons in a configuration:

$$f_{n\text{-tot}}\{(n_i, l_i)\} = \sum_i n_i \quad . \quad (3.8)$$

The next simplest possible guess is similar to the aufbau rule for the order of orbital occupation in the ground configurations of neutral elements, i.e. the total $n + l$ for all electrons in a configuration:

$$f_{\text{auf}}\{(n_i, l_i)\} = \sum_i n_i + l_i \quad . \quad (3.9)$$

The bound is set by evaluating the truncation functions at the terminus of the first Rydberg sequence. For example, for the case that $n_{\text{max}} = 6$, the last entry of the first Rydberg sequence in a five-electron ion is $1s^2 2s^2 6g$. Using the aufbau truncation function:

$$f_{\text{auf}}\{1s^2 2s^2 6g\} = 17 \quad ,$$

while for the total n truncation function:

$$f_{n\text{-tot}}\{1s^2 2s^2 6g\} = 12 \quad .$$

Let it be clear that *there is nothing physical about these guesses*; they are purely for the purpose of reducing the number of configurations within a maximum n -shell. What we find empirically is that these two truncation functions are different enough from one another that the decisions made by CRISTAL with the aufbau truncation function will, at a certain iteration, diverge from those

made with the total n truncation function. We take these first agreed upon decisions to be the decisions that would have been made without any truncation function and give them to CRISTAL as user input for a brute calculation (i.e. one with no truncation function). This choice usually removes enough configurations to fit within the RAM limits of most computing clusters.

Here we find a clear trend: the number of decisions agreed upon between CRISTAL using aufbau truncation vs using total n depends on the ratio of protons to electrons. For C^+ , they agree on 1 decision; for N^{2+} , they agree on 3 decisions; for O^{3+} , they agree on 5 decisions; and, for O^{4+} , they agree on 7 decisions. This is a consequence of the deviations gained from starting with the central-field approximation: the greater the ratio of the charge nuclear charge to the total charge of the bound electrons, the better the CFA basis will approximate the stationary states.

In the worst case scenario (C^+) of our chosen ions, the two different truncation schemes have only the first decision in common (i.e. the pruning of the $[1]^0$ prefix) which, with $n_{\max} = 5$, leaves a total of 2880 configurations and approaches RAM limits. For reference, a DR calculation using CRISTAL's optimum configuration set with $n_{\max} = 6$ and 1952 configurations, fed into AUTOSTRUCTURE (using the LAPACK diagonalizer), required 30 Gb of RAM, and required 134 Gb with $n_{\max} = 7$ and 4233 configurations. In this case, the only option is to grow multiple configuration trees, each with different guesses for which branches CRISTAL would prune next. Such a group of trees is called a **decision forest**. The more CRISTAL decisions that we guess, the larger our forest will have to be in order to check all alternative possibilities. Therefore, we only guess as many pruning decisions as is necessary for the configuration sequence of each tree to stay within RAM limits. CRISTAL can then run on separate trees in parallel and the decision set that gives the most quickly decaying cost function is taken as the optimum solution.

3.4 Results from CRISTAL

As our first example, we compute the optimum selection of states for three ions in the Boron-like isoelectronic sequence (C^+ , N^{2+} , and O^{3+}) using the TFDA method for our CFA basis. For each ion, the chosen representative configurations of the first Rydberg sequence are $2s^25f$ and $2s^25g$. For

the second Rydberg sequence, the chosen representative configurations are: $2s2p3p$ and $2s2p3d$ for C^+ , $2s2p4p$ and $2s2p4d$ for N^{2+} , and $2s2p4d$ and $2s2p5p$ for O^{3+} . Figures 3.11–3.14 show the convergence of the energy spectra to the NIST values as a function of the iteration (see Figure 3.11) for both truncation functions and for the brute truncation.

In the case that $n_{\max} = 6$, using brute truncation, the average differences with NIST spectra are 0.0274Ry for C^+ , 0.0147Ry for N^{2+} , and 0.00727Ry for O^{3+} . As shown by Figures 3.11–3.14, these are roughly an order of magnitude smaller than the average differences calculated using the AUTOSTRUCTURE input files that were used to generate the archived rate coefficients. We can also see that the accuracy follows our expectations for the strength of the CFA. C^+ has the smallest ratio of protons to electrons and so has the least accurate energies of the three ions, while the opposite is true for O^{3+} .

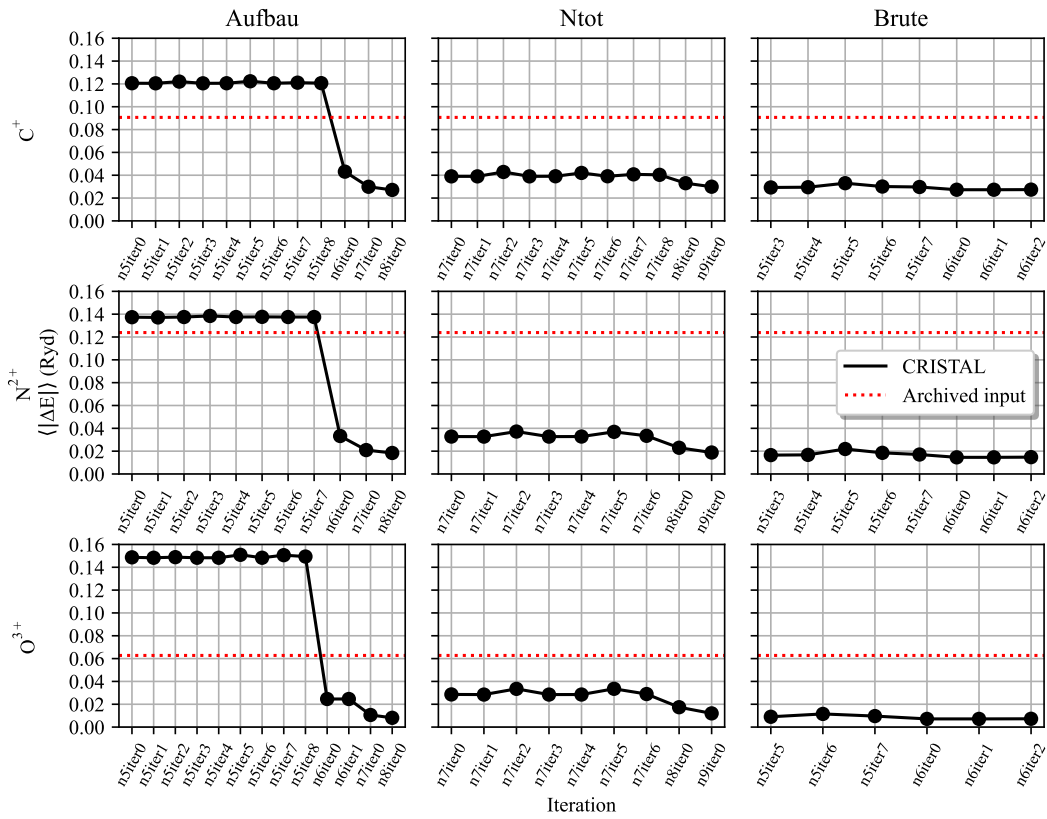


Figure 3.11: The weighted average difference from the tabulated energies as a function of the iteration. Iterations are labeled by the current n -shell and the current iteration within that n -shell, e.g. "n5iter0" for the 5th n -shell at the 0th iteration. Rows correspond to the ion (C^+ , N^{2+} , and O^{3+} from top to bottom) and columns correspond to the truncation function ("aufbau", "ntot", and "brute" from right to left). The horizontal red dotted lines show the average difference calculated using the AUTOSTRUCTURE input files from the ADAS archive.

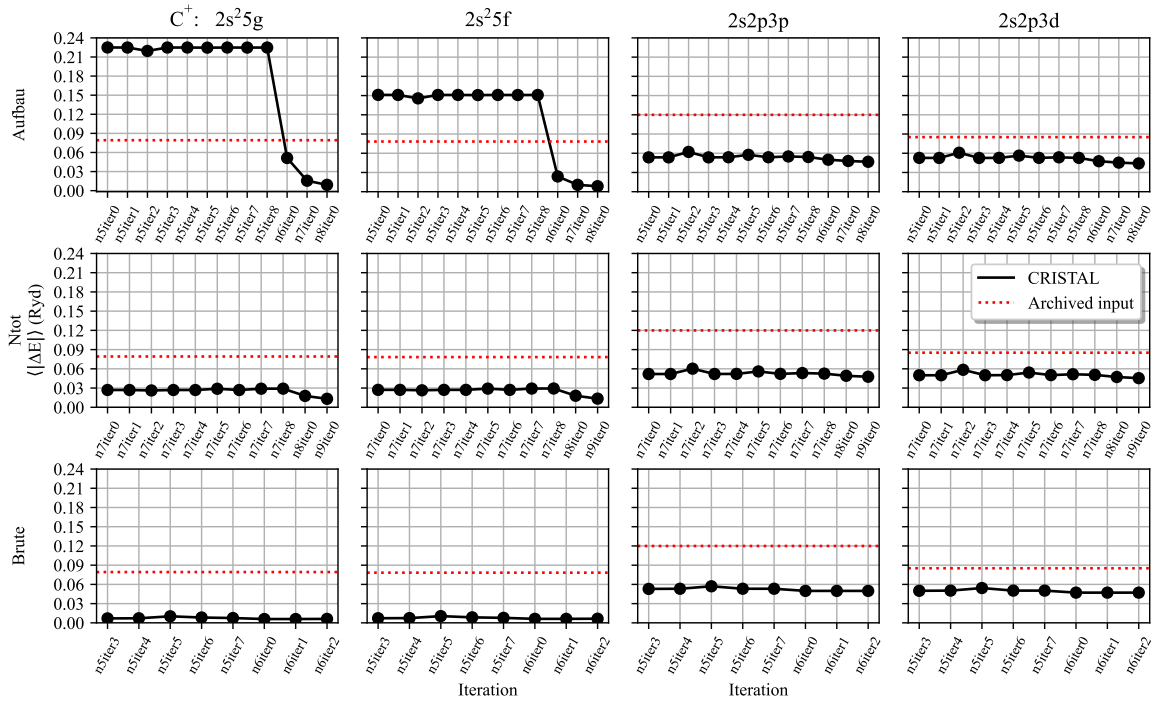


Figure 3.12: C^+ configuration average differences from the tabulated energies calculated from CRISTAL as a function of the iteration (see Figure 3.11) compared to the same quantity calculated from the archived AUTOSTRUCTURE input files (red dotted line). Rows correspond to the truncation function and columns correspond to the configuration.

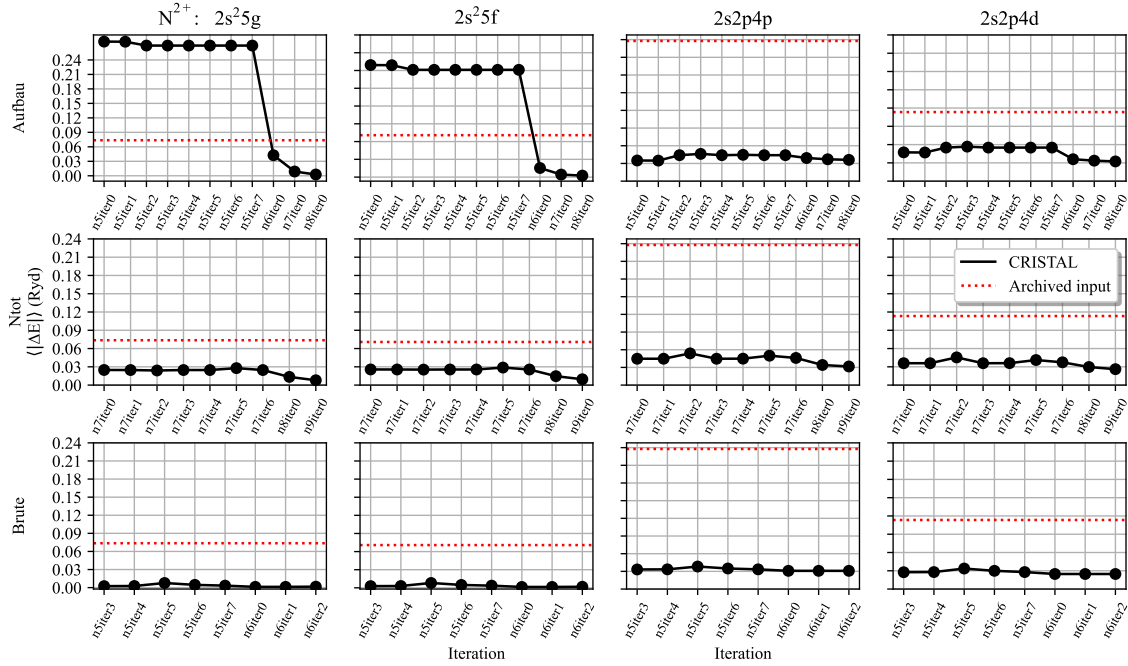


Figure 3.13: N^{2+} configuration average differences from the tabulated energies calculated from CRISTAL as a function of the iteration (see Figure 3.11) compared to the same quantity calculated from the archived AUTOSTRUCTURE input files (red dotted line). Rows correspond to the truncation function and columns correspond to the configuration.

Another result that can be seen in Table 3.1 is that the pruning decisions made CRISTAL are the same for all ions in the isoelectronic sequence when no truncation function is used. One may have guessed that this would be the case from physical intuitions but, to confidently apply this assumption to other isoelectronic sequences, it would be preferable to prove this result rigorously. This will be our next immediate goal (see Chapter 5).

Finally, we can see that the configuration sequences that CRISTAL constructs have a particular character. Consider the remaining complex prefixes for the Boron-like isoelectronic sequence: $[1]^2$, $[1]^1[2]^2[3]^2$, $[1]^1[2]^2[3]^1$, $[1]^1[2]^2[3]^0[4]^2$, $[1]^1[2]^2[3]^0[4]^1$, and $[1]^1[2]^2[3]^0[4]^0[5]^2$. In terms of Rydberg sequences, these are: $1s^2 nl n'l' n''l''$ with $n, n', n'' \geq 2$; $1s2s^2 nl n'l'$, $1s2s2p nl n'l'$, and $1s2p^2 nl n'l'$ with $3 \leq n \leq 4$ and $n' \geq 3$; and finally $1s2s^2 5l 5l'$, $1s2s2p 5l 5l'$, and $1s2p^2 5l 5l'$. It should be clear that the fastest growing sequence here is the first which grows cubically. Then the size of the configuration sequence, and thus the time complexity (\mathcal{T}_{tree}) of generating the

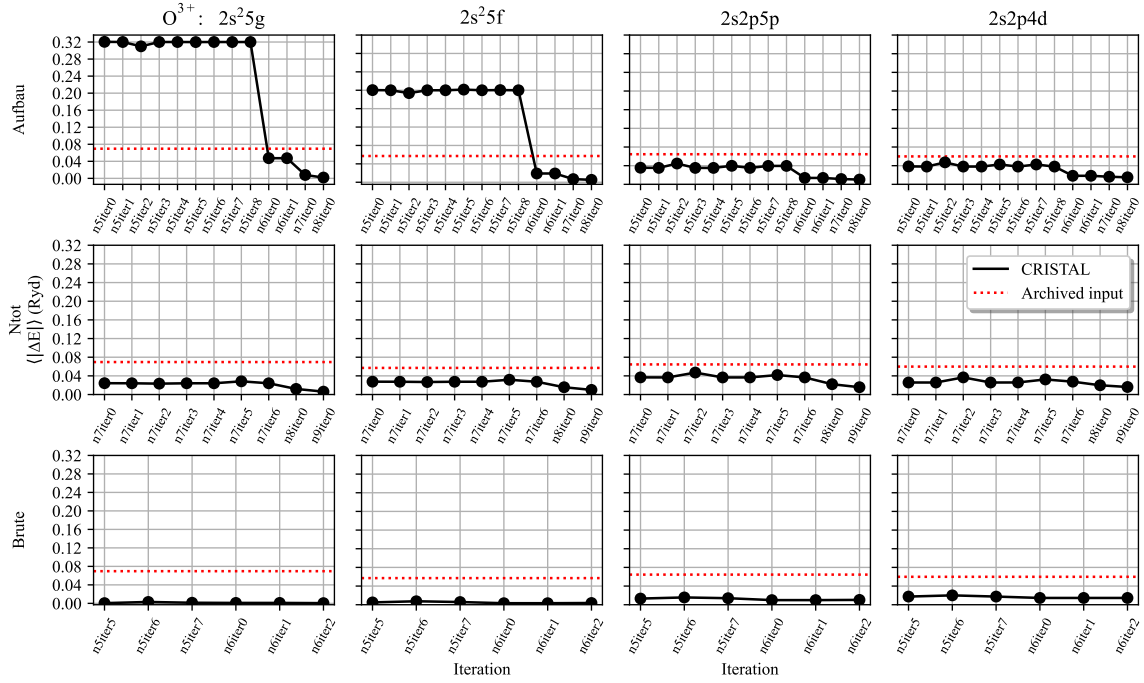


Figure 3.14: O^{3+} configuration average differences from the tabulated energies calculated from CRISTAL as a function of the iteration (see Figure 3.11) compared to the same quantity calculated from the archived AUTOSTRUCTURE input files (red dotted line). Rows correspond to the truncation function and columns correspond to the configuration.

	C^+	N^{2+}	O^{3+}
Aufbau	$[1]^0$ $[1]^1[2]^0$ $[1]^1[2]^1$ $[1]^1[2]^2[3]^0$ $[1]^1[2]^2[3]^1[4]^0$	$[1]^0$ $[1]^1$ $[1]^2[2]^0[3]^0$ $[1]^2[2]^0[3]^1[4]^0$ $[1]^2[2]^0[3]^1[4]^1$	$[1]^0$ $[1]^1[2]^0$ $[1]^1[2]^1$ $[1]^1[2]^2[3]^0$ $[1]^1[2]^2[3]^1[4]^0[5]^0$
Ntot	$[1]^0$ $[1]^1[2]^0$ $[1]^1[2]^1$ $[1]^1[2]^2[3]^0$	$[1]^0$ $[1]^1[2]^0$ $[1]^1[2]^1$	$[1]^0$ $[1]^1[2]^0$ $[1]^1[2]^1$
Brute	$[1]^0$ $[1]^1[2]^0$ $[1]^1[2]^1$ $[1]^1[2]^2[3]^0[4]^0[5]^0$ $[1]^1[2]^2[3]^0[4]^0[5]^1$	$[1]^0$ $[1]^1[2]^0$ $[1]^1[2]^1$ $[1]^1[2]^2[3]^0[4]^0[5]^0$ $[1]^1[2]^2[3]^0[4]^0[5]^1$	$[1]^0$ $[1]^1[2]^0$ $[1]^1[2]^1$ $[1]^1[2]^2[3]^0[4]^0[5]^0$ $[1]^1[2]^2[3]^0[4]^0[5]^1$

Table 3.1: The shell prefixes removed by CRISTAL. Rows correspond to the truncation function used and columns correspond to the ion.

sequence, grows cubically as a function of the number of orbitals from this point on. In the cases of C^{2+} and N^{3+} , the remaining complex prefixes chosen by CRISTAL are: $[1]^2$, $[1]^1[2]^3$, $[1]^1[2]^2$, $[1]^1[2]^1[3]^2$, $[1]^1[2]^1[3]^1[4]^1$, and $[1]^1[2]^1[3]^1[4]^0[5]^1$. In terms of Rydberg sequences, these are: $1s^2 nl n'l'$ with $n, n' \geq 2$; $1s2s^2 nl$, $1s2s2p nl$, and $1s2p^2 nl$ with $n \geq 2$; and finally $1s2s3s nl$, $1s2s3p nl$, $1s2s3d nl$, $1s2p3s nl$, $1s2p3p nl$ and $1s2p3d nl$ with $3 \leq n \leq 5$. Clearly, the first sequence listed has the highest growth, being quadratic, with the others being linear or finite. Then, as we claimed in Section 3.1, $\mathcal{T}_{\text{tree}}$ is reducible to $O(N_{\text{orb}}^{N_{\text{e,vic}}})$.

Now that the accuracy of the calculated stationary states and their associated energies has been improved, the next task will be to use them to calculate dielectronic recombination data. In the next chapter, we will briefly review the theoretical foundations of calculating DR rate coefficients and then show the predictions given by our new models.

Chapter 4

DR Rate Coefficient Results

In order to plot the relevant rate coefficients for dielectronic recombination, the raw energies, Auger and radiative rates from AUTOSTRUCTURE must go through a post-processing step performed by the ADAS post-processing code. Before discussing our final results, it would be helpful to review some of the relevant theory behind DR rate coefficients as well as the assumptions and approximations that are particular to AUTOSTRUCTURE and ADAS. First, note that, quantum mechanically, dielectronic recombination interferes with radiative recombination. For practical purposes, however, it has been shown [73] that the effect on the total Maxwellian recombination rate coefficient is very small in the absence of an external electric and magnetic fields so we can treat DR and RR as independent processes. For most temperatures studied here, the radiative recombination rate coefficient is very small and so there is very little background to interfere with. Using the isolated resonance approximation, the detailed balance relation between the DR and Auger rates, and treating the resonances as delta functions, one can obtain the dielectronic recombination rate coefficient α_{iv}^{z+1} from an initial metastable state ν of an ion X^{+z+1} into a state i of an ion X^{+z} . This is given in [74] and in the present form in [23]:

$$\alpha_{iv}^{z+1} = \left(\frac{4\pi a_0^2 I_H}{k_B T} \right)^{3/2} \sum_j \frac{\omega_j}{2\omega_\nu} e^{E_c/(k_B T_e)} \frac{\sum_l A_{j \rightarrow \nu, E_c l}^a A_{j \rightarrow i}^r}{\sum_h A_{j \rightarrow h}^r + \sum_{m, l} A_{j \rightarrow m, E_c l}^a} \quad (4.1)$$

where a_0 is the Bohr radius, I_H is the ionization potential of hydrogen, ω_j is the statistical weight of the recombined doubly-excited resonance state j , ω_ν is the statistical weight of the recombining target state, E_c is the energy of the continuum electron (with orbital angular momentum l), and the autoionization (A^a) and radiative (A^r) rates are in inverse seconds.

AUTOSTRUCTURE (by default) uses a further approximation: the autoionization rates are calculated via perturbation theory using the Golden Rule coined by Fermi [75] (but actually derived by Dirac [76]) and continuum electron wave functions represented as distorted waves. With this choice, the current approach is typically referred to as the independent processes and isolated resonances using distorted waves (IPIRDW) approximation. Here, the following limit is crucial:

$$\lim_{n \rightarrow \infty} \left(\frac{\pi n^3}{2z^2} \right)^{3/2} P_{nl}(r) = F_{kl}(r) \Big|_{r=0} , \quad (4.2)$$

where P_{nl} is a high-energy bound orbitals (normalized to unity) for the captured electron, and is being approximated by the continuum orbital F_{kl} (normalized to $\pi\delta(k-k')$ with $k^2 = E_c$) evaluated with energy $E = E_c + z^2/n^2$. As explained by Badnell [23], the mean radius of a Rydberg orbital scales as n^2 and, thus, this approximation is necessary to represent orbitals with high n values. With this approximation, transition rates can be calculated straightforwardly using Fermi's Golden rule. Non-perturbative methods that go beyond the distorted wave approximation, such as the R-matrix approach, can also be used to generate DR rate coefficients and also include interference between radiative and DR rates.

4.1 Plasma Dielectronic Recombination Rate Coefficients

With the exception of ultra-high density plasmas [77], we can treat the total rate coefficient using the statistics of non-interacting particles:

$$\alpha(T_e) = \int dE \alpha(E) f(E, T_e) , \quad (4.3)$$

where the energy-dependent rate from (4.1) is now being convolved with an electron energy distribution function $f(E, T_e)$. For a storage ring experiment, there are two useful expositions of the DR spectral data: (1) a plot of the DR rate coefficient as a function of the kinetic energy of an electron beam and (2) a plot of the DR rate coefficient as a function of the electron temperature in a diffuse plasma. We discuss these cases below.

4.1.1 Cooler Distribution

In the case of an electron beam being coaxially merged with an ion beam, we need the energy distribution function of an electron cooler. As done by Danared [78], the AUTOSTRUCTURE post-processor models the velocity distribution of the beam as having a Gaussian profile in the parallel and perpendicular directions, with associated temperatures $T_{e\parallel}$ and $T_{e\perp}$ respectively. Explicitly, the velocity distribution function is:

$$f(\mathbf{v}_e) = \frac{m_e}{2\pi k_B T_{e\perp}} \sqrt{\frac{m_e}{2\pi k_B T_{e\parallel}}} \exp\left(-\frac{m_e v_{e\perp}^2}{2k_B T_{e\perp}} - \frac{m_e v_{e\parallel}^2}{2k_B T_{e\parallel}}\right). \quad (4.4)$$

The configuration sets described in the previous sections were used in an AUTOSTRUCTURE DR calculation by including an additional set of configurations that model the recombining ion and an incident electron. The resulting energies, Auger rates, and radiative rates can be post-processed into DR rate coefficients. As mentioned at the end of Section 2.2, orbital scaling parameters can be used to improve the radial part of the wave functions. Although AUTOSTRUCTURE possesses its own internal optimization method that minimizes the sum of selected eigenenergies, we have used the cost function from CRISTAL so that the net optimization is self-consistent. We varied the scaling parameters for the 2s and 2p orbitals, excluding those pairs for which above-threshold eigenenergies were shifted to below-threshold and those below-threshold shifted to above-threshold. Following this procedure, the optimum values of the N^{2+} scaling parameters were 1.13 for the 2s orbital and 1.24 for the 2p orbital. For C^+ , the analogous values were 1.04 for the 2s orbital and 1.2 for the 2p orbital. Incidentally, these values are not significantly different from those obtained using AUTOSTRUCTURE's internal optimization method.

One important aspect of the DR rate coefficients from the ADAS archive [79] for these two ions is that an additional shift of the ground state energy was included in the post-processing to make some low-energy doubly excited state energies agree with the available NIST energies. This shift improves the DR rate coefficients in the archived data at low temperatures, but is only possible for systems with measured values for the low energy resonances. Thus, we have plotted both the

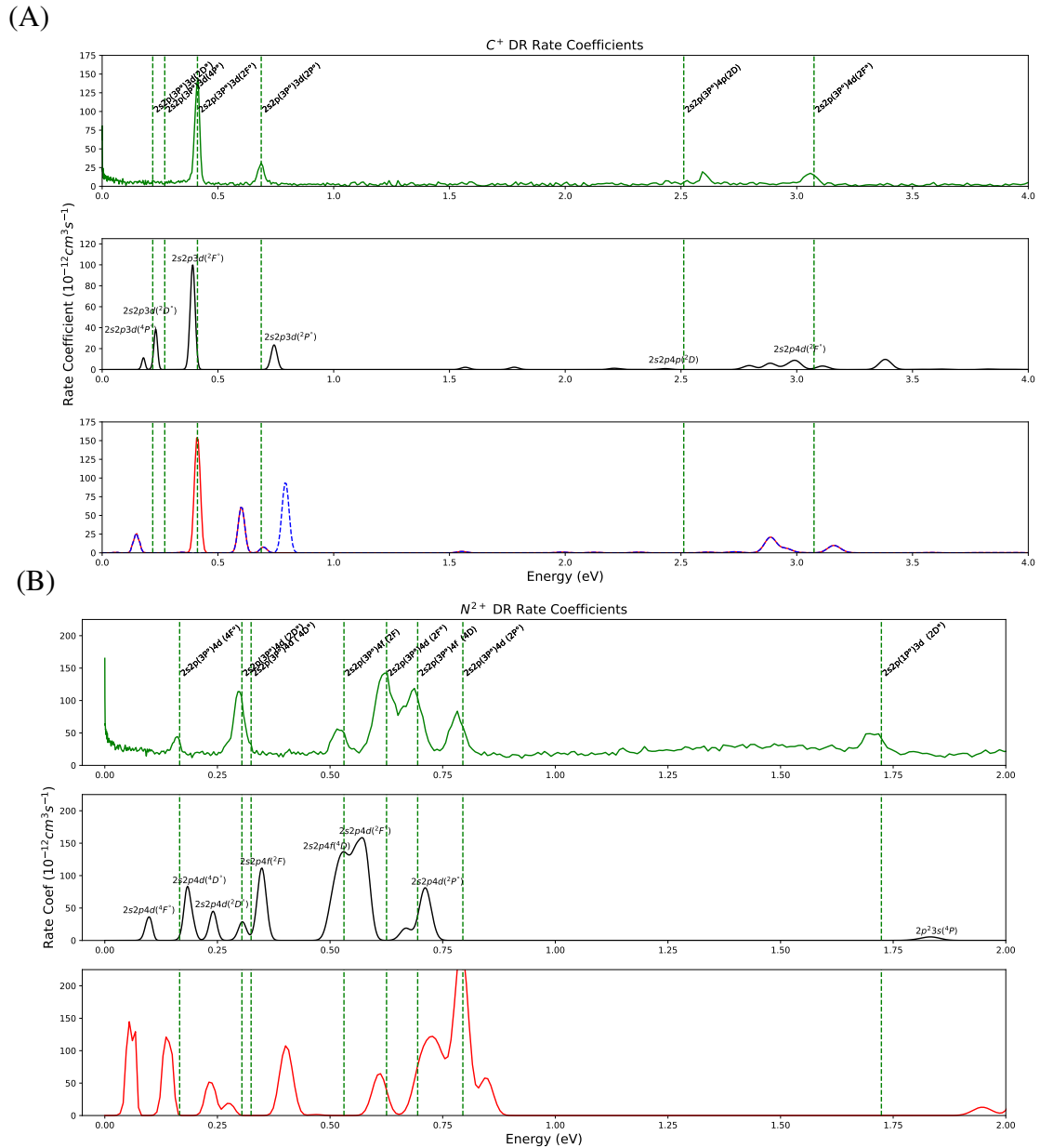


Figure 4.1: Beam Auger resonance plots for (A) C^+ and (B) N^{2+} as a function of the electron beam kinetic energy in eV relative to the ionization threshold. The experimental data from the storage ring is shown in green, the calculated data using CRISTAL's large CI and optimized orbital scaling parameters is shown in black, and the data from the ADAS archive using default AUTOSTRUCTURE with an extra shift of the ground state energy resonance nearest to the ionization threshold is shown in red. (A) also includes a dashed blue curve that shows the data calculated using default AUTOSTRUCTURE without any extra shift of the ground state energy. This blue curve is not shown in panel (B) because the shift did not significantly change the resonances in this case. Vertical dashed green lines show the tabulated resonance positions from the NIST database [2].

archived data and the data that would be generated from the archived input files with no extra shift (i.e., typical for the majority of the DR project data).

A comparison between the calculated and experimental beam resonances from a set of experiments done using a storage ring ([44]) is shown in Figure 4.1 for two of the three ions, C^+ and N^{2+} . Similarly, Figure 4.2 shows a comparison between the calculated and experimental Maxwellian-convolved rate coefficients rates for the same ions. Since the widths of the experimental resonances are on the order of 10^{-2} eV and the J splitting is on the order of 10^{-3} eV, we should consider this data to be LS resolved but not J resolved. It is clear that, in both cases, rate coefficients calculated using our method are a closer match to the experimental data than those calculated using the archived input files and the archived rates that were shifted for better agreement in post processing.

In the case of C^+ , the improvement is qualitative: our method predicts the correct number of resonances in the correct order (with the exception of the resonance nearest to the ionization threshold) whereas the archived rates do not. In the second panel from the top in Figure 4.1 (A), we can see the resonances tabulated by NIST (vertical dashed green lines) compared to the calculated resonance positions (black curve). In order from lowest to highest energy, the calculated resonances are: $2s2p3d(^4P)$ at 0.176 ± 0.002 eV ($\Delta E_{NIST} = -0.095$ eV), $2s2p3d(^2D)$ at 0.236 ± 0.001 eV ($\Delta E_{NIST} = 0.018$ eV), $2s2p3d(^2F)$ at 0.389 ± 0.003 eV ($\Delta E_{NIST} = -0.024$ eV), $2s2p3d(^2P)$ at 0.747 ± 0.002 eV ($\Delta E_{NIST} = 0.060$ eV), $2s2p4p(^2D)$ at 2.440 ± 0.002 eV ($\Delta E_{NIST} = 0.072$ eV), and $2s2p4p(^2F)$ at 2.9953 ± 0.003 eV ($\Delta E_{NIST} = -0.079$ eV), where ΔE_{NIST} is the signed difference from the tabulated energy value. It should be noted that the storage ring data for C^+ appears to be missing two resonances near threshold. Since both tabulated energies and the calculated energies predict that these two resonances should be present, we believe that these resonances are likely absent due to an experimental complication such as background noise overpowering the signal. This behavior would be consistent with the storage ring data for N^{2+} , whose background noise features a wide bump centered around 1.5eV and holds fairly constant moving towards the ionization threshold, ending in a sharp spike.

For the case of N^{2+} , the new calculated resonances positions (Figure 4.1 (B) in black) are demonstrably closer to the tabulated energy values than those calculated with the archived input files, though the $2s2p4d(^2D)$ and $2s2p4d(^2F)$ resonances have exchanged order with the $2s2p4d(^4D)$ and $2s2p4f(^4D)$ resonances respectively. Again, in order from lowest to highest energy, the calculated resonances are: $2s2p4d(^4F)$ at 0.096 ± 0.006 eV ($\Delta E_{NIST} = -0.070$ eV), $2s2p4d(^4D)$ at 0.185 ± 0.003 eV ($\Delta E_{NIST} = -0.140$ eV), $2s2p4d(^2D)$ at 0.243 ± 0 eV ($\Delta E_{NIST} = -0.061$ eV), $2s2p4f(^2F)$ at 0.349 ± 0.001 eV ($\Delta E_{NIST} = -0.182$ eV), $2s2p4f(^4D)$ at 0.526 ± 0.005 eV ($\Delta E_{NIST} = -0.168$ eV), $2s2p4d(^2F)$ at 0.562 ± 0.006 eV ($\Delta E_{NIST} = -0.064$ eV), and $2s2p4d(^2P)$ at 0.711 ± 0.004 eV ($\Delta E_{NIST} = -0.084$ eV), and $2p^23s(^4P)$ at 1.837 ± 0.008 eV ($\Delta E_{NIST} = -0.391$ eV).

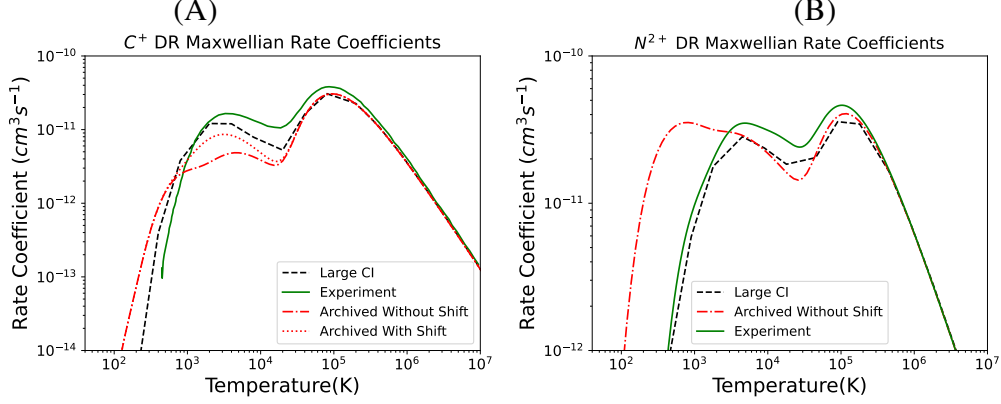


Figure 4.2: Maxwellian rate coefficients for (A) C^+ and (B) N^{2+} as a function of the plasma temperature in Kelvin. Experimental data from the storage ring is shown in green, the calculated data using CRISTAL’s large CI and optimized orbital scaling parameters is shown by the black dashed curve, the data calculated using the archived AUTOSTRUCTURE input file with a shift of the ground state energy is shown by the red dotted curve, and the data calculated using the archived AUTOSTRUCTURE with no additional shift is shown by the red dot-dashed curve. Note that panel (B) only shows the archived AUTOSTRUCTURE calculation without the additional shift because the shift had no effect in this case.

4.1.2 Maxwellian Distribution

For the case of a diffuse plasma, we can use the familiar Maxwellian distribution function to represent the free-electron energy distribution:

$$f(E, T_e) = \frac{2E^{1/2}}{\pi^{1/2}(k_B T_e)^{3/2}} \exp\left(-\frac{E}{k_B T_e}\right). \quad (4.5)$$

The Maxwellian rate coefficients for C^+ and N^{2+} are shown in Figure 4.2 and those for C^{2+} and N^{3+} are shown in Figure 4.3. In all cases, the Maxwellian rate coefficient predicted by the archived AUTOSTRUCTURE input files without the extra shift of the ground state energy is significantly further from the experimental rate coefficient than that predicted by our new input files. Additionally, even with the additional shift of the ground state energy, as was done to calculate the archived Maxwellian rate coefficients, the predicted curve is still further from our new calculated rate coefficients in all but the N^{3+} case. We note that the experimental rate coefficient tends to be higher than the calculated curves in the 1–10 eV region, which may be due to signal noise between the resonances that can be seen in the resonance plots in Figure 4.1.

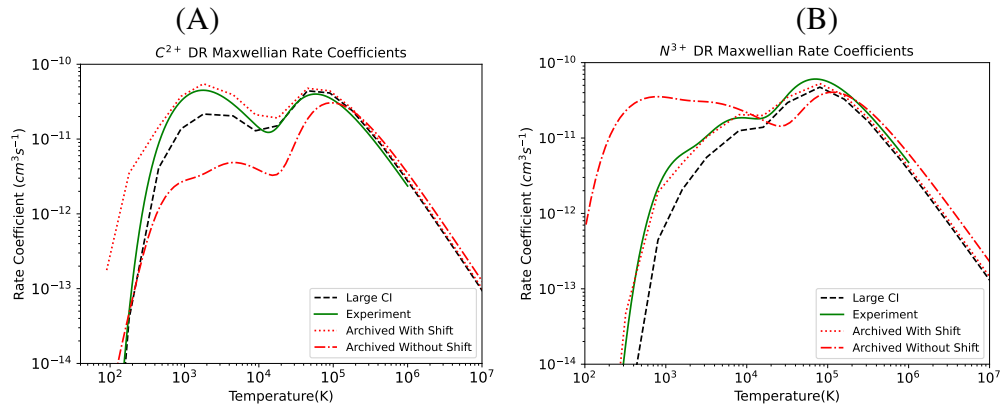


Figure 4.3: Maxwellian rate coefficients for (A) C^{2+} and (B) N^{3+} as a function of the plasma temperature in Kelvin. Experimental data from the storage ring is shown in green, the calculated data using CRISTAL's large CI and optimized orbital scaling parameters is shown by the black dashed curve, the data calculated using the archived AUTOSTRUCTURE input file with a shift of the ground state energy is shown by the red dotted curve, and the data calculated using the archived AUTOSTRUCTURE with no additional shift is shown by the red dot-dashed curve.

It is clear in all cases shown that the configuration sequences chosen by CRISTAL show good agreement with the experimental data. Additionally, the new data is a marked improvement over the archived rate coefficients in the low temperature regime.

Chapter 5

A Theorem for Isoelectronic Hamiltonians

In Section 3.4, it was shown that the optimum configuration sequences chosen by CRISTAL were invariant along the Boron-like and Beryllium-like isoelectronic sequences. In the field of atomic structure modeling, it is common to assume such an invariance. If this result holds for all cases, we will be able to apply the optimum configuration set for one ion of interest to any other ion in the isoelectronic sequence. Without a rigorous proof, however, such a strong claim will rest only on intuition. In this chapter, we will demonstrate that the robustness of the invariance rests only on the validity of the Hamiltonian used to model the system. This demonstration requires the treatment of the parameter Z , which specifies the proton number, as a dynamical variable. Such an approach may seem strange to the reader, perhaps even alarming. However, this sort of treatment has been used successfully by Layzer [71] to derive a series expansion for the eigenvalues of a multi-electron ion. As described in his 1959 publication, the structure of atomic spectra has no qualitative dependence on the discrete character of Z , so we lose nothing by ignoring it.

Lemma 5.0.1. *Let $\{Z_k\}$ parametrize a family of Hamiltonians, $\widehat{H}(\{Z_k\})$, such that the mapping between any two such Hamiltonians and its inverse are both smooth and differentiable, i.e. we have a set of one parameter families of diffeomorphisms. If \widehat{H} is nondegenerate, this induces a diffeomorphism on its eigenstates represented by the matrix with elements:*

$$\zeta_{k,mn} = \begin{cases} \frac{(\partial \widehat{H} / \partial Z_k)_{mn}}{E_n - E_m} & (m \neq n) \\ 0 & (m = n) \end{cases} .$$

Proof:

First, define the matrix $\widehat{\zeta}_k$ by:

$$\zeta_{k,mn} = \langle m | \frac{\partial}{\partial Z_k} | n \rangle, \quad \frac{\partial}{\partial Z_k} | n \rangle = \widehat{\zeta}_k | n \rangle = \sum_{n'} \zeta_{k,n'n} | n' \rangle . \quad (5.1)$$

Note that, by considering its action on the Kronecker delta, we have

$$\begin{aligned} \frac{\partial(\delta_{mn})}{\partial Z_k} = 0 &= \frac{\partial}{\partial Z_k} (\langle m | | n \rangle) + \langle m | \frac{\partial}{\partial Z_k} | n \rangle \\ &= \left(\langle n | \frac{\partial}{\partial Z_k} | m \rangle \right)^* + \langle m | \frac{\partial}{\partial Z_k} | n \rangle . \end{aligned}$$

Since we are dealing with bound eigenstates of a Hamiltonian, we can choose them to be real valued. Thus, $\widehat{\zeta}_k$ is antisymmetric:

$$0 = \left(\widehat{\zeta}^\dagger \right)_{mn} + \left(\widehat{\zeta} \right)_{mn} \implies \zeta_{mm} = 0 . \quad (5.2)$$

Now, to find the off-diagonal elements of $\widehat{\zeta}_k$, we need only consider the action of the Hamiltonian on its eigenstates:

$$\widehat{H} | n \rangle = E_n | n \rangle .$$

Now, taking the derivative w.r.t. Z_k , we have:

$$\frac{\partial \widehat{H}}{\partial Z_k} | n \rangle + \widehat{H} \sum_{n'} \zeta_{n'n} | n' \rangle = \frac{\partial E_n}{\partial Z_k} | n \rangle + E_n \sum_{n'} \zeta_{n'n} | n' \rangle .$$

Acting from the left by a bra, we find the off-diagonal elements:

$$m \neq n \implies \left(\frac{\partial \widehat{H}}{\partial Z_k} \right)_{mn} + E_m \zeta_{k,mn} = 0 + \zeta_{k,mn} E_n .$$

Now, solving for the matrix elements of $\widehat{\zeta}_k$, it is clear that they must be non-singular if $\frac{\partial \widehat{H}}{\partial Z_k}$ is non-singular:

$$\therefore \zeta_{k,mn} = \begin{cases} \frac{(\partial \widehat{H} / \partial Z_k)_{mn}}{E_n - E_m} & (m \neq n) \\ 0 & (m = n) \end{cases} \quad \square . \quad (5.3)$$

Lemma 5.0.2. *If another operator, \widehat{h} , is also transformed diffeomorphically, then the matrix elements of its partial derivative w.r.t. Z_k is related to the partial derivative of its matrix elements w.r.t. Z_k in the eigenbasis of $\widehat{H}(\{Z_k\})$ by the following non-singular differential equation:*

$$\left(\frac{\partial \widehat{h}}{\partial Z_k} \right)_{mn} = \left[\widehat{\zeta}_k, \widehat{h} \right]_{mn} + \frac{\partial (h_{mn})}{\partial Z_k} .$$

Proof:

The steps follow similarly as in the proof of Lemma 5.0.1: expand the action of \widehat{h} on a ket, and then take the partial derivative w.r.t. Z_k . In this case, we need to take more care to account for the fact that \widehat{h} is not necessarily diagonal:

$$\begin{aligned} \widehat{h} |n\rangle &= \sum_{n'} h_{n'n} |n'\rangle , \\ \frac{\partial \widehat{h}}{\partial Z_k} |n\rangle + \widehat{h} \sum_{n'} \zeta_{k,n'n} |n'\rangle &= \sum_{n'} \left[\frac{\partial (h_{n'n})}{\partial Z_k} |n'\rangle + h_{n'n} \sum_{n''} \zeta_{k,n''n'} |n''\rangle \right] , \\ \frac{\partial \widehat{h}}{\partial Z_k} |n\rangle + \sum_{n''n'} h_{n''n'} \zeta_{k,n'n} |n''\rangle &= \sum_{n'} \frac{\partial (h_{n'n})}{\partial Z_k} |n'\rangle + \sum_{n''n'} \zeta_{k,n''n'} h_{n'n} |n''\rangle . \end{aligned}$$

Now, just as before, we can act from the left by a bra:

$$\begin{aligned} \langle m | \frac{\partial \widehat{h}}{\partial Z_k} | n \rangle + \sum_{n''n'} h_{n''n'} \zeta_{k,n'n} \langle m | n'' \rangle &= \sum_{n'} \frac{\partial (h_{n'n})}{\partial Z_k} \langle m | n' \rangle + \sum_{n''n'} \zeta_{k,n''n'} h_{n'n} \langle m | n'' \rangle \quad , \\ \left(\frac{\partial \widehat{h}}{\partial Z_k} \right)_{mn} + \sum_{n'} h_{mn'} \zeta_{k,n'n} &= \frac{\partial (h_{mn})}{\partial Z_k} + \sum_{n'} \zeta_{k,nn'} h_{n'n} \quad . \end{aligned}$$

It's now clear that, by subtracting the summation from the right-hand side, we get the stated differential equation, which must be non-singular by Lemma 5.0.1:

$$\left(\frac{\partial \widehat{h}}{\partial Z_k} \right)_{mn} = \left[\widehat{\zeta}_k, \widehat{h} \right]_{mn} + \frac{\partial (h_{mn})}{\partial Z_k} \quad \square \quad . \quad (5.4)$$

The differential equation (5.4) can be solved by using an exponential integrating factor. Formally, this integrating factor would be defined by a Dyson series. We will describe this in more detail in Chapter 6, Section 6.2, but for now we take it as a given that such an integrating factor can be solved by a path-ordered exponential (denoted by $\mathcal{P} \exp$). Let:

$$\widehat{E}(Z_k) = \mathcal{P} \exp \left[\int_{Z_{k,0}}^{Z_k} dZ'_k \widehat{\zeta}_k(Z'_k) \right], \quad \widehat{E}^{-1}(Z_k) = \mathcal{P} \exp \left[- \int_{Z_{k,0}}^{Z_k} dZ'_k \widehat{\zeta}_k(Z'_k) \right] \quad . \quad (5.5)$$

Then we have that:

$$\frac{\partial}{\partial Z_k} \left\{ \sum_{ab} \left[\left(\widehat{E} \right)_{ma} h_{ab} \left(\widehat{E}^{-1} \right)_{bn} \right] (Z_k) \right\} = \sum_{ab} \left[\left(\widehat{E} \right)_{ma} \left(\frac{\partial \widehat{h}}{\partial Z_k} \right)_{ab} \left(\widehat{E}^{-1} \right)_{bn} \right] (Z_k) \quad ,$$

and therefore:

$$\boxed{h_{mn}(Z_k) = \sum_{ab} \left(\widehat{E}^{-1}(Z_k) \right)_{ma} h_{ab}(Z_{k,0}) \left(\widehat{E}(Z_k) \right)_{bn} + \sum_{aa'b'b} \left(\widehat{E}^{-1}(Z_k) \right)_{ma} \left\{ \int_{Z_{k,0}}^{Z_k} dZ'_k \left[\left(\widehat{E} \right)_{aa'} \left(\frac{\partial \widehat{h}}{\partial Z_k} \right)_{a'b'} \left(\widehat{E}^{-1} \right)_{b'b} \right] (Z'_k) \right\} \left(\widehat{E}(Z_k) \right)_{bn}} \quad . \quad (5.6)$$

Lemma 5.0.3. *A Hamiltonian \widehat{H} is differentiable by Z_k iff its eigenstates are differentiable by Z_k and its eigenenergies are differentiable by Z_k .*

Proof

We can simply apply equation (5.4) to the Hamiltonian itself:

$$\left(\frac{\partial \widehat{H}}{\partial Z_k} \right)_{mn} = \zeta_{k,mn} E_m - E_n \zeta_{k,mn} + \frac{\partial E_n}{\partial Z_k} \delta_{mn} \quad . \quad (5.7)$$

The equation can only be non-singular if both $\widehat{\zeta}_k$ and $\frac{\partial E_n}{\partial Z_k}$ are non-singular. \square

In the context of ions, our Hamiltonian has the general form:

$$\widehat{H} = \sum_i \frac{\widehat{p}_i^2}{2m_e} + Z \widehat{V}_i(\mathbf{r}_i, \mathbf{p}_i) + \sum_{j < i} \widehat{V}_{ij}(\mathbf{r}_{ij}, \mathbf{p}_i, \mathbf{p}_j) \quad . \quad (5.8)$$

Likewise, the mean field approximation to this Hamiltonian has the general form:

$$\widehat{H}_{MF} = \sum_i \frac{\widehat{p}_i^2}{2m_e} + Z \widehat{V}_i(\mathbf{r}_i, \mathbf{p}_i) + \widehat{V}_{MF,i}(Z; \mathbf{r}_i, \mathbf{p}_i) \quad . \quad (5.9)$$

Theorem 5.0.1. *In the eigenbasis of a mean-field approximated Hamiltonian that includes all one-electron operators of the original Hamiltonian, the set of block indices of the original Hamiltonian are invariant under change of proton number that leaves the total charge non-positive.*

Proof:

First, define the perturbation from the mean field as:

$$\widehat{V}_p = \widehat{H} - \widehat{H}_{MF} = \sum_i \left(\sum_{j < i} \widehat{V}_{ij} \right) - \widehat{V}_{MF,i} \quad . \quad (5.10)$$

The off-diagonal elements of \widehat{V}_p will be the same as those of \widehat{H} , but the nuclear interaction and kinetic energy operators have been canceled, so the block index sets of \widehat{V}_p will be the same as those of \widehat{H} .

Next, we show that mapping \widehat{H}_{MF} and \widehat{V}_p to a different proton number is a diffeomorphism. As long as the total charge is non-positive, we can be certain that bound states will remain bound. Additionally, for each bound state, there will always be an analogous state in an ion that differs only in the number of protons (i.e. any other ion in the isoelectronic sequence). More precisely, since the eigenfunctions of each ion in an isoelectronic sequence form orthonormal bases of functions and all bases have the same boundary conditions, the mapping between bases must be unitary. Then a continuous change of the effective proton number forms a one parameter subgroup of the unitary Lie group and is, therefore, differentiable in both directions. Thus the mapping is a diffeomorphism of the eigenstates. By the same reasoning, the eigenenergies are also diffeomorphic between ions in an isoelectronic sequence and, as long as LS coupling is included, there is no degeneracy. Then, by Lemma 5.0.3, a change in the proton number that leaves the total charge non-positive is a diffeomorphism of ionic Hamiltonians. That the mean-field Hamiltonians are diffeomorphic then follows by the same arguments, but with the configuration average energies and the corresponding radial wave functions. Therefore, we can substitute \widehat{V}_p into equation (5.4), and be sure that it is non-singular:

$$\frac{\partial V_{p,mn}}{\partial Z_k} + [\widehat{\zeta}_k, \widehat{V}_p]_{mn} = - \left(\sum_i \frac{\partial \widehat{V}_{MF,i}}{\partial Z_k} \right)_{mn} . \quad (5.11)$$

Additionally, using equation (5.3) we can see that:

$$\zeta_{k,mn} = \frac{\left(\partial \widehat{H}_{MF} / \partial Z_k \right)_{mn}}{E_n - E_m} = \frac{\sum_i \left(\widehat{V}_{k,i}(\mathbf{r}_i, \mathbf{p}_i) + \partial \widehat{V}_{MF,i}(Z; \mathbf{r}_i, \mathbf{p}_i) / \partial Z_k \right)_{mn}}{E_n - E_m} \quad (m \neq n) . \quad (5.12)$$

From this result it is clear that all of the operators that would transform \widehat{V}_p in the solution given by equation (5.6) have the same symmetries as \widehat{V}_p (i.e. symmetric under spatial inversion, and commuting with \widehat{L}^2 and \widehat{S}^2). However, they are one-electron operators whereas \widehat{V}_p has two-electron operators from the electron-electron interactions. Therefore, *the sets of block indices of*

With this theorem, and a sufficiently accurate Hamiltonian that includes all the relevant 1-electron operators, there is no longer any doubt that the optimum configuration sequence given by an algorithm such as CRISTAL will be invariant along an isoelectronic sequence.

Chapter 6

Quantum Transitions

When computing the DR rate coefficient, it is common practice to calculate the transition rate using a first-order approximation known as Fermi's Golden Rule, as mentioned in Chapter 4. Studies on the breakdown of this first-order approximation are relatively recent e.g. [80–83]. As summarized by Chen [83], the validity of the rule rests on the existence of a continuum of states, a weak perturbing potential, and an appropriate time window in which the transition will be completed. A common example where Fermi's Golden rule is not appropriate is in the case of metastable transitions. Quantifying the uncertainty of using Fermi's Golden rule is necessary to accurately gauge the accuracy of our current models for DR. In this chapter, we derive a relatively simple quantitative heuristic that can be used to place an upper bound on this uncertainty.

6.1 The method of time varying coefficients

The first approach to solving a time-dependent Hamiltonian is to assume a superposition of eigenstates of the initial Hamiltonian and solve for the time varying coefficients. We begin similarly to time dependent perturbation theory by assuming the following:

$$|\Psi(t)\rangle = \sum_k c_{ki}(t) e^{-iE_k t/\hbar} |\psi_k\rangle = \widehat{U}(t) |\psi_i\rangle \quad , \quad (6.1)$$

where $\widehat{U}(t)$ is the time evolution operator on the initial ket $|\psi_i\rangle$. Now we apply the Schrödinger equation with an added time-varying potential:

$$\left(\widehat{H}_0 + \widehat{V}(t)\right) |\Psi(t)\rangle = i\hbar \frac{\partial}{\partial t} \sum_k c_{kj}(t) e^{-iE_k t/\hbar} |\psi_k\rangle = i\hbar \sum_k \left(-i \frac{E_k}{\hbar} c_{kj}(t) + \frac{dc_{kj}}{dt}\right) e^{-iE_k t/\hbar} |\psi_k\rangle \quad .$$

Taking the inner product with $\langle \psi_f |$ gives:

$$E_i c_{fi}(t) e^{-iE_f t/\hbar} + \sum_k \langle \psi_f | \widehat{V}(t) | \psi_k \rangle c_{ki}(t) e^{-iE_k t/\hbar} = E_f c_{fi}(t) + i\hbar \frac{dc_{fi}}{dt} e^{-iE_f t/\hbar} .$$

Simplifying and letting $V_{fk}(t) = \langle \psi_f | \widehat{V}(t) | \psi_k \rangle$, and $\omega_{fk} = \frac{E_f - E_k}{\hbar}$, we obtain the following system of ordinary differential equations:

$$\boxed{\frac{dc_{fi}}{dt} = -\frac{i}{\hbar} \sum_k V_{fk}(t) e^{i\omega_{fk} t} c_{ki}(t)} . \quad (6.2)$$

If the potential has a small factor λ , then the standard procedure is to expand each coefficient perturbatively:

$$c_{fi}(t) = \sum_{j=0}^{\infty} \lambda^j c_{fi}^{(j)}(t), \quad \text{with} \quad c_{fi}(0) = \delta_{fi} .$$

With these conditions, and substituting $V_{fk}(t) \rightarrow \lambda V_{fk}(t)$,

$$\begin{aligned} \sum_{j=0}^{\infty} \lambda^j \frac{dc_{fi}^{(j)}}{dt} &= -\frac{i}{\hbar} \sum_k \lambda V_{fk}(t) e^{i\omega_{fk} t} \sum_{j=0}^{\infty} \lambda^j c_{ki}^{(j)}(t) \\ &= \sum_{j=0}^{\infty} \lambda^{j+1} \left(-\frac{i}{\hbar} \right) \sum_k V_{fk}(t) e^{i\omega_{fk} t} c_{ki}^{(j)}(t) , \\ \sum_{j=0}^{\infty} \lambda^j \frac{dc_{fi}^{(j)}}{dt} &= \sum_{j=1}^{\infty} \lambda^j \left(-\frac{i}{\hbar} \right) \sum_k V_{fk}(t) e^{i\omega_{fk} t} c_{ki}^{(j-1)}(t) . \end{aligned}$$

Now, matching powers of the perturbative parameters, we can see that

$$\begin{cases} \frac{dc_{fi}^{(0)}}{dt} = 0 \\ \frac{dc_{fi}^{(j)}}{dt} = -\frac{i}{\hbar} \sum_k V_{fk}(t) e^{i\omega_{fk} t} c_{ki}^{(j-1)}(t) \quad \text{for } j > 0 \end{cases} . \quad (6.3)$$

This gives a recurrence relation for the j th order of the expansion of the coefficients. Since the 0th order term is time independent, it must carry the initial condition, $c_{fi}^{(0)} = \delta_{fi}$. Then the recurrence

relation gives the first-order correction:

$$\frac{dc_{fi}^{(1)}}{dt} = -\frac{i}{\hbar} \sum_k V_{fk}(t) e^{i\omega_{fk}t} \delta_{ki} = -\frac{i}{\hbar} V_{fi}(t) e^{i\omega_{fi}t} .$$

And thus,

$$c_{fi}^{(1)} = -\frac{i}{\hbar} \int_{t_0}^t d\tau e^{i\omega_{fi}\tau} V_{fi}(\tau) , \quad (6.4)$$

which gives the famous Fermi's Golden rule:

$$P_{i \rightarrow f}(t) \approx \frac{1}{\hbar^2} \left| \int_{t_0}^t d\tau e^{i\omega_{fi}\tau} V_{fi}(\tau) \right|^2 \quad (6.5)$$

This approach is common in textbook introductions to quantum mechanics. However the method of time varying coefficients proves cumbersome to extract second- and higher-order corrections to the transition rate. A general solution requires a broader framing of the problem.

6.2 The operator approach

Another approach we could take is to find an equation for the transition operator. This approach was developed by Freeman Dyson [84], and leads to the Dyson series. We begin by expressing a general solution form in terms of an initial ket and the time evolution operator on the initial ket.

$$|\Psi(t)\rangle = \widehat{U}(t) |\Psi(0)\rangle .$$

Now, applying the Schrödinger equation,

$$i\hbar \frac{\partial}{\partial t} \left(\widehat{U}(t) |\Psi(0)\rangle \right) = \widehat{H}(t) \widehat{U}(t) |\Psi(0)\rangle ,$$

and since the initial state is time independent, this implies that

$$i\hbar \frac{d}{dt} \widehat{U} = \widehat{H}(t) \widehat{U} \quad . \quad (6.6)$$

If we are careful about how we define the exponential, then we can say:

$$\widehat{U}(t) = \exp \left(-\frac{i}{\hbar} \int_{t_0}^t d\tau \widehat{H}(\tau) \cdot \right) \quad , \quad (6.7)$$

where the symbol " \cdot " is used to denote that this is an integral operator acting on the space of functions of τ .

We must use an expansion analogous to a Taylor expansion for a scalar argument, but redefine the meaning of a power of the argument to better suit an operator argument. For example, this expression:

$$\left(\int_{t_0}^t d\tau \widehat{H}(\tau) \cdot \right)^2 = \int_{t_0}^t d\tau_1 \int_{t_0}^t d\tau_2 \widehat{H}(\tau_1) \widehat{H}(\tau_2) \cdot \quad ,$$

would be naive because the time derivative would be:

$$\frac{d}{dt} \int_{t_0}^t d\tau_1 \int_{t_0}^t d\tau_2 \widehat{H}(\tau_1) \widehat{H}(\tau_2) \cdot = \widehat{H}(t) \int_{t_0}^t d\tau_2 \widehat{H}(\tau_2) \cdot + \left(\int_{t_0}^t d\tau_1 \widehat{H}(\tau_1) \cdot \right) \widehat{H}(t) \quad ,$$

which leaves an operator on the right of the last term.

Alternatively, we could split the integral into two parts, one where $\tau_1 > \tau_2$ and another where $\tau_1 < \tau_2$:

$$\left(\int_{t_0}^t d\tau \widehat{H}(\tau) \cdot \right)^2 = \int_{t_0}^t d\tau_1 \int_{t_0}^{\tau_1} d\tau_2 \widehat{H}(\tau_1) \widehat{H}(\tau_2) \cdot + \int_{t_0}^t d\tau_2 \int_{t_0}^{\tau_2} d\tau_1 \widehat{H}(\tau_1) \widehat{H}(\tau_2) \cdot \quad .$$

By simply relabeling the integration variables on the second integral we get:

$$\begin{aligned} \left(\int_{t_0}^t d\tau \widehat{H}(\tau) \cdot \right)^2 &= \int_{t_0}^t d\tau_1 \int_{t_0}^{\tau_1} d\tau_2 \widehat{H}(\tau_1) \widehat{H}(\tau_2) \cdot + \int_{t_0}^t d\tau_1 \int_{t_0}^{\tau_1} d\tau_2 \widehat{H}(\tau_2) \widehat{H}(\tau_1) \cdot \quad , \\ \therefore \left(\int_{t_0}^t d\tau \widehat{H}(\tau) \cdot \right)^2 &= \int_{t_0}^t d\tau_1 \int_{t_0}^{\tau_1} d\tau_2 \left[\widehat{H}(\tau_1) \widehat{H}(\tau_2) \cdot + \widehat{H}(\tau_2) \widehat{H}(\tau_1) \cdot \right] \quad . \end{aligned}$$

Now it is clear that the problem is the second term in the integrand. The correct integrand to use would be the time ordered product with a factor to account for the permutations. We want to make the replacement:

$$\left(\int_{t_0}^t d\tau \widehat{H}(\tau) \cdot \right)^2 \rightarrow 2! \int_{t_0}^t d\tau_1 \int_{t_0}^{\tau_1} d\tau_2 \widehat{H}(\tau_1) \widehat{H}(\tau_2) \cdot \quad .$$

And in general, we express the n -th power of a time-ordered integral of an operator in the following way:

$$\mathcal{T} \left\{ \left(\int_{t_0}^t d\tau \widehat{H}(\tau) \cdot \right)^n \right\} = n! \prod_{k=1}^n \int_{t_0}^{\tau_{k-1}} d\tau_k \widehat{H}(\tau_k) \cdot \quad \text{with } \tau_0 = t \quad . \quad (6.8)$$

Therefore, the correct expression of the time-evolution operator is:

$$\boxed{\widehat{U}(t) = \mathcal{T} \exp \left(-\frac{i}{\hbar} \int_{t_0}^t d\tau \widehat{H}(\tau) \cdot \right) = \widehat{1} + \sum_{n=1}^{\infty} \left(-\frac{i}{\hbar} \right)^n \prod_{k=1}^n \int_{t_0}^{\tau_{k-1}} d\tau_k \widehat{H}(\tau_k) \cdot} \quad (\tau_0 = t) \quad . \quad (6.9)$$

where the product is done in order from left to right (left-action of subsequent terms) and the usual weight of $\frac{1}{n!}$ has canceled due to the time ordering. This gives an exact solution to the Schrödinger equation for the case of a time-dependent Hamiltonian.

It's also worth noting that since the time ordered exponential can solve any system of linear differential equations with initial conditions, such as

$$\frac{dy_i}{dt} = M_{ij} y_j \quad .$$

(using the Einstein summation convention), we can also solve an IVP for a linear ODE of any order since we could always make a matrix which maps consecutive vector elements to the derivative of the previous elements. To illustrate, consider the following 4×4 system:

$$\frac{d}{dt} \begin{pmatrix} y_1 \\ y_2 \\ y_3 \\ y_4 \end{pmatrix} = \begin{pmatrix} 0 & 1 & 0 & 0 \\ 0 & 0 & 1 & 0 \\ 0 & 0 & 0 & 1 \\ M_{41}(t) & M_{42}(t) & M_{43}(t) & M_{44}(t) \end{pmatrix} \begin{pmatrix} y_1 \\ y_2 \\ y_3 \\ y_4 \end{pmatrix} .$$

In this case, y_2 is the time derivative of y_1 , y_3 is the time derivative of y_2 , y_4 the time derivative of y_3 , and the time derivative of y_4 is a linear combination of the last four, making this system equivalent to a linear fourth order ODE with time varying coefficients. As before, given the initial values, we can use the time ordered exponential of the matrix to solve the system and equivalently solve the fourth order ODE.

To apply this in the context of time-dependent perturbations to a quantum Hamiltonian, we must change to the interaction picture. We define the following change of variables:

$$\widehat{H}(t) = \widehat{H}_0 + \widehat{V}(t) ; \quad |\Psi(t)\rangle = e^{-i\widehat{H}_0 t/\hbar} |\Psi_I(t)\rangle . \quad (6.10)$$

Now our Schrödinger equation becomes

$$\begin{aligned} (\widehat{H}_0 + \widehat{V}(t)) e^{-i\widehat{H}_0 t/\hbar} |\Psi_I(t)\rangle &= i\hbar \frac{\partial}{\partial t} e^{-i\widehat{H}_0 t/\hbar} |\Psi_I(t)\rangle \\ &= \widehat{H}_0 e^{-i\widehat{H}_0 t/\hbar} |\Psi_I(t)\rangle + i\hbar e^{-i\widehat{H}_0 t/\hbar} \frac{\partial}{\partial t} |\Psi_I(t)\rangle . \end{aligned}$$

Now subtracting the equal terms and replacing $|\Psi_I(t)\rangle = \widehat{U}(t) |\Psi_I(t_0)\rangle$ we get

$$\begin{aligned} \widehat{V}(t) e^{-i\widehat{H}_0 t/\hbar} \widehat{U}(t) |\Psi_I(t_0)\rangle &= i\hbar e^{-i\widehat{H}_0 t/\hbar} \frac{d\widehat{U}(t)}{dt} |\Psi_I(t_0)\rangle , \\ \implies \frac{d\widehat{U}(t)}{dt} &= -\frac{i}{\hbar} e^{i\widehat{H}_0 t/\hbar} \widehat{V}(t) e^{-i\widehat{H}_0 t/\hbar} \widehat{U}(t) . \end{aligned}$$

This then yields the solution:

$$\boxed{\widehat{U}_I(t) = \mathcal{T} \exp \left\{ -\frac{i}{\hbar} \int_{t_0}^t d\tau e^{i\widehat{H}_0\tau/\hbar} \widehat{V}(\tau) e^{-i\widehat{H}_0\tau/\hbar} \right\}} , \quad (6.11)$$

and the wave function:

$$|\Psi_I(t)\rangle = \left\{ \widehat{1} + \sum_{n=1}^{\infty} \left(-\frac{i}{\hbar} \right)^n \prod_{k=1}^n \int_{t_0}^{\tau_{k-1}} d\tau_k e^{i\widehat{H}_0\tau_k/\hbar} \widehat{V}(\tau_k) e^{-i\widehat{H}_0\tau_k/\hbar} \right\} |\Psi_I(t_0)\rangle \quad (\tau_0 = t) \quad . \quad (6.12)$$

This perturbative expansion, when truncated at the second term, is documented to agree with experiment to one part in 10^{10} for measurements of the fine structure constant [85].

Note that the first two terms in the expansion, when projected onto the unperturbed basis, are equivalent to the 0th and 1st order corrections to the perturbative coefficients:

$$\begin{aligned} \widehat{1} &\rightarrow \delta_{fi} \quad , \\ -\frac{i}{\hbar} \int_{t_0}^t d\tau e^{i\widehat{H}_0\tau/\hbar} \widehat{V}(\tau) e^{-i\widehat{H}_0\tau/\hbar} &\rightarrow -\frac{i}{\hbar} \int_{t_0}^t d\tau e^{iE_f\tau/\hbar} V_{fi}(\tau) e^{-iE_i\tau/\hbar} \quad . \end{aligned}$$

6.3 A criterion for the validity of Fermi's Golden Rule

With this foundation in place, we are in a good position to derive a criterion for the validity of Fermi's golden rule. First, note that the form of equation (6.9) can be thought of as a geometric series with the ratio being the operator:

$$-\frac{i}{\hbar} \int_{t_0}^{\tau_{k-1}} d\tau_k \widehat{H}(\tau_k) \quad ,$$

or, in the interaction picture:

$$-\frac{i}{\hbar} \int_{t_0}^{\tau_{k-1}} d\tau_k e^{i\widehat{H}_0\tau_k/\hbar} \widehat{V}(\tau_k) e^{-i\widehat{H}_0\tau_k/\hbar} \quad .$$

This can be most clearly seen if we recast the differential equation for the evolution operator as an integral equation:

$$\frac{d\widehat{U}(t)}{dt} = -\frac{i}{\hbar} e^{i\widehat{H}_0 t/\hbar} \widehat{V}(t) e^{-i\widehat{H}_0 t/\hbar} \widehat{U}(t) \quad .$$

Integrating both sides of this equation with the initial condition that $\widehat{U}(t_0) = \widehat{1}$,

$$\widehat{U}(t) - \widehat{1} = -\frac{i}{\hbar} \int_{t_0}^t d\tau e^{i\widehat{H}_0 \tau/\hbar} \widehat{V}(\tau) e^{-i\widehat{H}_0 \tau/\hbar} \widehat{U}(\tau) \quad ,$$

$$\implies \widehat{U}(t) = \widehat{1} - \frac{i}{\hbar} \int_{t_0}^t d\tau e^{i\widehat{H}_0 \tau/\hbar} \widehat{V}(\tau) e^{-i\widehat{H}_0 \tau/\hbar} \widehat{U}(\tau) \quad . \quad (6.13)$$

This equation falls under the class of Volterra integral equations [86]. Then, a general expression for the evolution operator should be:

$$\widehat{U}(t) = \left[1 + \frac{i}{\hbar} \int_{t_0}^t d\tau e^{i\widehat{H}_0 \tau/\hbar} \widehat{V}(\tau) e^{-i\widehat{H}_0 \tau/\hbar} \right]^{-1} \quad . \quad (6.14)$$

We can now consider what would be the worst case scenario for Fermi's Golden Rule, the case that the state being acted on by the evolution operator is in fact stationary under its action. If the state is an eigenstate of this operator, then the Dyson series simplifies to a geometric series in a scalar ratio. If we take our more general expression above, which makes no assumption about the strength of the perturbation, and assume that the state it acts on is an eigenstate of the operator in the integrand, we will get:

$$\begin{aligned} \frac{1}{\hbar} \int_{t_0}^t d\tau e^{i\widehat{H}_0 \tau/\hbar} \widehat{V}(\tau) e^{-i\widehat{H}_0 \tau/\hbar} |\Psi_I(t_0)\rangle &= \sigma(t) |\Psi_I(t_0)\rangle \\ \implies |\Psi_I(t)\rangle &= \frac{1}{1 + i\sigma(t)} |\Psi_I(t_0)\rangle \quad . \end{aligned}$$

Now, let

$$D = \frac{1}{1 + i\sigma(t)} \quad . \quad (6.15)$$

Unitarity requires that:

$$|D|^2 = \frac{1}{1 - 2\Im(\sigma(t)) + |\sigma(t)|^2} = 1 \quad . \quad (6.16)$$

If we decompose σ into:

$$\sigma(t) = \rho(t) [\cos(\theta(t)) + i \sin(\theta(t))] \quad . \quad (6.17)$$

Then, the requirement is that:

$$1 - 2\rho(t) \sin(\theta(t)) + \rho^2(t) = 1 \quad ,$$

or, more simply:

$$\rho(t) = 2 \sin(\theta(t)) \quad . \quad (6.18)$$

Then, substituting into (6.17) we can say that:

$$\sigma(t) = 2 \sin(\theta(t)) \cos(\theta(t)) + i2 \sin^2(\theta(t)) = \sin(2\theta(t)) + i(1 - \cos(2\theta(t))) \quad . \quad (6.19)$$

Then, letting $\vartheta = 2\theta$, and substituting this into (6.15), we have that:

$$D = \frac{1}{\cos(\vartheta(t)) + i \sin(\vartheta(t))} = \cos(\vartheta(t)) - i \sin(\vartheta(t)) \quad , \quad (6.20)$$

which clearly has a squared magnitude of 1.

Now, we can use this result to compare to the first-order approximation. It is important to recall that, since our analysis comes from assuming the extreme case that the state is stationary, computing a transition rate would not be fruitful, i.e. an eigenstate does not transition. However, we can still compute the error of a first-order approximation to the evolution operator. If we had chosen to approximate the factor (6.15) with the first-order approximation, we would have:

$$F = 1 - i\sigma(t) = 2 - \cos(\vartheta(t)) - i \sin(\vartheta(t)) \quad , \quad (6.21)$$

using the expression in (6.19). Now we can directly compute the error in the evolution operator. Roughly speaking, we should require that:

$$\Delta = \frac{|D - F|}{|D|} = |2 - 2 \cos(\vartheta(t))| \ll 1 \quad . \quad (6.22)$$

If we were being more precise, we may want this error ratio to be smaller than 1 part in some power of 10. In that case, restricting to values of $0 \leq \vartheta \leq \frac{\pi}{2}$, we have:

$$1 - \cos(\vartheta(t)) < \frac{1}{2 \times 10^p} \quad .$$

Then, in terms of the angle ϑ and the eigenvalue σ , our criterion is:

$$\boxed{\vartheta = 2 \arctan \left(\frac{\Re(\sigma)}{\Im(\sigma)} \right) < \arccos \left(\frac{2 \times 10^p - 1}{2 \times 10^p} \right)} \quad . \quad (6.23)$$

This approach requires that the critical eigenstates of integrand in equation (6.11) are identified. Once identified, eigenstates which are relevant to the environment under study can be analyzed using this criterion.

Such a simple criterion would provide a straightforward and computationally inexpensive way to gauge the validity of the Golden Rule in general scenarios. Before applying this approach in

general, however, it would be prudent to apply it to some test cases, which will be the subject of future work.

Chapter 7

Coupling Angular Momenta

Currently, CRISTAL neglects the configuration interaction rule for angular momentum which requires that two interacting configurations have at least one pair of orbital and spin total angular momentum quantum numbers (i.e. an LS term) in common. The computational expense could potentially be reduced with a method of determining the allowed angular momentum couplings. We test a novel approach for calculating angular momentum coupling coefficients for the two-particle case and outline a generalization for the N-particle case.

In the case of multiple particles, the Hilbert space is a tensor product of the single particle Hilbert spaces:

$$\mathcal{H} = \bigotimes_{i=1}^N \mathcal{H}_i \quad . \quad (7.1)$$

A ket in this space is a sum of Kronecker products of single particle kets:

$$|\psi\rangle = \sum_{m_1, \dots, m_N} \left(\bigotimes_{i=1}^N \langle j_i, m_i | \right) |\psi\rangle \bigotimes_{i=1}^N |j_i, m_i\rangle \quad . \quad (7.2)$$

Operators that act on only (e.g.) particle i are technically a Kronecker product of a single particle operator acting on \mathcal{H}_i and the identity operators all other Hilbert spaces. For the sake of brevity, we will use the following simplification of the notation for these kinds of operators:

$$\bigotimes_{k=1}^{i-1} \widehat{I}_k \otimes \widehat{A}_i \otimes \bigotimes_{k=i+1}^N \widehat{I}_k = \widehat{I}_1 \otimes \dots \otimes \widehat{I}_{i-1} \otimes \widehat{A}_i \otimes \widehat{I}_{i+1} \otimes \dots \otimes \widehat{I}_N \rightarrow \widehat{A}_i \quad . \quad (7.3)$$

It should be clear that

$$i \neq j \implies [\widehat{A}_i, \widehat{B}_j] = 0 \quad . \quad (7.4)$$

Now, in the more specific case of angular momentum, the total angular momentum operator expands as follows:

$$\widehat{J}^2 \equiv \widehat{J}_x^2 + \widehat{J}_y^2 + \widehat{J}_z^2 = \left(\sum_{i=1}^N \widehat{J}_{ix} \right)^2 + \left(\sum_{i=1}^N \widehat{J}_{iy} \right)^2 + \left(\sum_{i=1}^N \widehat{J}_{iz} \right)^2 \quad . \quad (7.5)$$

As in the case with a single particle, it will be useful to represent the above expression in terms of raising and lowering operators. Consider the following product of angular momentum operators:

$$\begin{aligned} \left(\sum_{i=1}^N \widehat{J}_{ix} \mp i\widehat{J}_{iy} \right) \left(\sum_{k=1}^N \widehat{J}_{kx} \pm i\widehat{J}_{ky} \right) &= \left(\sum_{i=1}^N \widehat{J}_{ix} \right) \left(\sum_{k=1}^N \widehat{J}_{kx} \right) + \left(\sum_{i=1}^N \widehat{J}_{iy} \right) \left(\sum_{k=1}^N \widehat{J}_{ky} \right) \\ &\quad \pm i \sum_{i,k=1}^N \left(\widehat{J}_{ix}\widehat{J}_{ky} - \widehat{J}_{iy}\widehat{J}_{kx} \right) \quad . \end{aligned}$$

On the right-hand side, the real part can be thought of as having two terms that are the squares of the x and y components of the total angular momentum. The imaginary part is a commutator, which can be simplified by the rule (7.4) as follows:

$$\begin{aligned} \left(\sum_{i=1}^N \widehat{J}_{ix} \mp i\widehat{J}_{iy} \right) \left(\sum_{k=1}^N \widehat{J}_{kx} \pm i\widehat{J}_{ky} \right) &= \widehat{J}_x^2 + \widehat{J}_y^2 \pm i \sum_{i,k=1}^N \left[\widehat{J}_{ix}, \widehat{J}_{ky} \right] \\ &= \widehat{J}_x^2 + \widehat{J}_y^2 \pm i \left(0 + \sum_{i=1}^N i\hbar \widehat{J}_{iz} \right) \quad . \end{aligned}$$

From this result, it is clear that such summations will satisfy the algebraic properties of the ladder operators (up to a factor of \hbar). Therefore, we can define the multi-particle angular momentum

ladder operators as:

$$\widehat{J}_{\pm} \equiv \frac{1}{\hbar} \sum_{i=1}^N (\widehat{J}_{ix} \pm i\widehat{J}_{iy}) = \sum_{i=1}^N \widehat{J}_{i\pm} \quad , \quad (7.6)$$

and then the square of the total angular momentum operator can be expanded analogously to the single particle case as:

$$\widehat{\mathbf{J}}^2 = \hbar^2 \widehat{J}_{\mp} \widehat{J}_{\pm} \pm \hbar \widehat{J}_z + \widehat{J}_z^2 = \hbar^2 \left(\sum_{i,k=1}^N \widehat{J}_{i\mp} \widehat{J}_{k\pm} \right) \pm \hbar \sum_{i=1}^N \widehat{J}_{iz} + \left(\sum_{i=1}^N \widehat{J}_{iz} \right)^2 \quad . \quad (7.7)$$

It can be demonstrated that all the commutator relations from the single particle case shown in Appendix B are satisfied analogously by the operators defined in equations (7.7) and (7.5) for the N-particle case, for example:

$$\left[\sum_{i=1}^N \widehat{J}_{iz} , \sum_{k=1}^N \widehat{J}_{k\pm} \right] = 0 + \sum_{i=1}^n [\widehat{J}_{iz} , \widehat{J}_{i\pm}] = \pm \hbar \sum_{i=1}^N \widehat{J}_{i\pm} \quad (7.8)$$

$$\left[\sum_{i=1}^N \widehat{J}_{iz} , \mathbf{J}^2 \right] = 0 \quad . \quad (7.9)$$

Following the results from above, the algebraic structure of the coupled angular momentum operators is completely analogous to the single particle case and their actions on kets can be specified by the following equations:

$$\left\{ \begin{array}{l} \sum_{i=1}^N \widehat{J}_{iz} |J, M\rangle = \hbar M |J, M\rangle \\ \widehat{\mathbf{J}}^2 |J, M\rangle = \hbar^2 J(J+1) |J, M\rangle \\ \left(\sum_{i=1}^N \widehat{J}_{i\pm} \right)^p |J, M\rangle = \sqrt{\frac{(J\mp M)!(J\pm M+p)!}{(J\mp M-p)!(J\pm M)!}} |J, M \pm p\rangle \end{array} \right. \quad . \quad (7.10)$$

7.1 Two particles

In the case of two angular momenta, the eigenvalues from the above equations are specified by the quantum numbers:

$$\begin{aligned} J &\in \{j_1 + j_2 - n : n \in \mathbb{Z}, 0 \leq n \leq j_1 + j_2 - |j_1 - j_2|\} \quad , \\ M &\in \{J - p : p \in \mathbb{Z}, 0 \leq p \leq 2J\} \quad . \end{aligned} \quad (7.11)$$

Here, the quantum number J emerges as quantifying the alignment between the two angular momentum vectors and defines a family of states, which we will refer to as an **alignment family**, each with different values of M , the vertical component of the total angular momentum.

For the case of two particles, it is common to use the following simplified notation to represent a Kronecker product of kets:

$$|j_1, m_1; j_2, m_2\rangle \equiv |j_1, m_1\rangle \otimes |j_2, m_2\rangle \quad . \quad (7.12)$$

Then, we can expand an eigenket as:

$$|J, M\rangle = \sum_{m_1, m_2} \langle j_1, m_1; j_2, m_2 | J, M \rangle |j_1, m_1; j_2, m_2\rangle \quad . \quad (7.13)$$

We can begin with the simplest family of coupled states: those whose individual angular momenta are maximally aligned. Starting from the case when $m_1 = j_1$ and $m_2 = j_2$, the family can be generated by a simple application of the coupled lowering operator. In terms of the individual quantum numbers (j_1 and j_2):

$$|j_1 + j_2, j_1 + j_2\rangle = |j_1, j_1; j_2, j_2\rangle \quad , \quad (7.14)$$

$$|j_1 + j_2, j_1 + j_2 - p\rangle = \sqrt{\frac{(2j_1 + 2j_2 - p)!}{(2j_1 + 2j_2)! p!}} \left(\widehat{J}_{1-} + \widehat{J}_{2-} \right)^p |j_1, j_1; j_2, j_2\rangle \quad . \quad (7.15)$$

This procedure will generalize to any family of kets with the same alignment. Given value of $J = j_1 + j_2 - n$ as in (7.11), we can generate the family of states as follows:

$$|j_1 + j_2 - n, j_1 + j_2 - n - p\rangle = \sqrt{\frac{(2j_1 + 2j_2 - 2n - p)!}{(2j_1 + 2j_2 - 2n)!p!}} \left(\widehat{J}_{1-} + \widehat{J}_{2-}\right)^p |j_1 + j_2 - n, j_1 + j_2 - n\rangle \quad . \quad (7.16)$$

More generally, to generate the alignment family for any number of particles, we take the ket for which $M = J$, which we will refer to as the **top ket**, and apply the lowering operator in the following way:

$$|J, J - p\rangle = \sqrt{\frac{(2J - p)!}{(2J)!p!}} \widehat{J}_-^p |J, J\rangle \quad . \quad (7.17)$$

It is at this point that we diverge from the literature. In order to generate different alignment families, it is common to use either an iterative method or, in the group theoretic approach, to use one of the 3-, 6-, or 9-j symbols [52]. For the purpose of determining the allowed term symbols for any configuration, however, the iterative method will be too opaque. Additionally, the group theoretic approach provides some valuable reference cases, but does not yield a general solution.

To address our particular needs, we seek an operator that maps the top ket of the maximal alignment family to the top ket of a different alignment family. Explicitly, we want that:

$$\widehat{\mathcal{F}}_{j_1, j_2}^{(n)} |j_1 + j_2, j_1 + j_2\rangle = |j_1 + j_2 - n, j_1 + j_2 - n\rangle \quad , \quad (7.18)$$

for a given $n \in \mathbb{Z}$ where $0 \leq n \leq j_1 + j_2 - |j_1 - j_2|$. We will refer to this operator as the **alignment lowering operator**. In order for this operator to behave as desired, it will need to satisfy certain general conditions. First, the commutator of this operator with the raising operator must map the

maximally aligned top ket to 0:

$$\begin{aligned} \widehat{J}_+ \widehat{\mathcal{F}}_{j_1, j_2}^{(n)} |j_1 + j_2, j_1 + j_2\rangle &= \widehat{J}_+ |j_1 + j_2 - n, j_1 + j_2 - n\rangle \quad , \\ \left(\left[\widehat{J}_+, \widehat{\mathcal{F}}_{j_1, j_2}^{(n)} \right] + \widehat{\mathcal{F}}_{j_1, j_2}^{(n)} \widehat{J}_+ \right) |j_1 + j_2, j_1 + j_2\rangle &= 0 \quad , \end{aligned}$$

where, on the right-hand side we have simply added and subtracted $\widehat{\mathcal{F}}_{j_1, j_2}^{(n)} \widehat{J}_+$ to produce the commutator, and the left-hand side vanishes trivially. Then we have that:

$$\left[\widehat{J}_+, \widehat{\mathcal{F}}_{j_1, j_2}^{(n)} \right] |j_1 + j_2, j_1 + j_2\rangle = 0 \quad . \quad (7.19)$$

Thus we require that the maximally aligned top ket be in the kernel of this commutator. Secondly, we need to be sure that the maximally aligned top ket is mapped to the correct eigenstate. Applying the vertical component of the total angular momentum operator:

$$\begin{aligned} \widehat{J}_z \widehat{\mathcal{F}}_{j_1, j_2}^{(n)} |j_1 + j_2, j_1 + j_2\rangle &= \widehat{J}_z |j_1 + j_2 - n, j_1 + j_2 - n\rangle \quad , \\ \left(\left[\widehat{J}_z, \widehat{\mathcal{F}}_{j_1, j_2}^{(n)} \right] + \widehat{\mathcal{F}}_{j_1, j_2}^{(n)} \widehat{J}_z \right) |j_1 + j_2, j_1 + j_2\rangle &= \hbar(j_1 + j_2 - n) |j_1 + j_2 - n, j_1 + j_2 - n\rangle \quad , \end{aligned}$$

where, just as before, we simply add and subtract a term $\widehat{\mathcal{F}}_{j_1, j_2}^{(n)} \widehat{J}_z$ on the right-hand side to produce the commutator. Applying the operator $\widehat{\mathcal{F}}_{j_1, j_2}^{(n)} \widehat{J}_z$ to the ket, the right-hand side will now have a term $\hbar(j_1 + j_2) |j_1 + j_2 - n, j_1 + j_2 - n\rangle$, which can be subtracted from both sides. Then, using the defining equation (7.18), and factoring the ket $|j_1 + j_2, j_1 + j_2\rangle$ from both sides, we have our second condition:

$$\left[\widehat{J}_z, \widehat{\mathcal{F}}_{j_1, j_2}^{(n)} \right] = -\hbar n \widehat{\mathcal{F}}_{j_1, j_2}^{(n)} \quad . \quad (7.20)$$

Together, these two conditions guarantee that we have generated the desired alignment family.

We can verify this now by applying the $\widehat{\mathbf{J}}^2$ operator:

$$\begin{aligned} \Rightarrow \widehat{\mathbf{J}}^2 \widehat{\mathcal{F}}_{j_1, j_2}^{(n)} |j_1 + j_2, j_1 + j_2\rangle &= \left(\hbar^2 \widehat{J}_- \widehat{J}_+ + \hbar^2 \widehat{J}_z + \widehat{J}_z^2 \right) \widehat{\mathcal{F}}_{j_1, j_2}^{(n)} |j_1 + j_2, j_1 + j_2\rangle \\ &= \left(0 + \hbar^2 (j_1 + j_2 - n) + \hbar^2 (j_1 + j_2 - n)^2 \right) \widehat{\mathcal{F}}_{j_1, j_2}^{(n)} |j_1 + j_2, j_1 + j_2\rangle \quad . \end{aligned}$$

In summary, the alignment lowering operator must satisfy the following two criteria:

$$\boxed{\begin{cases} \left[\widehat{J}_+, \widehat{\mathcal{F}}_{j_1, j_2}^{(n)} \right] |j_1 + j_2, j_1 + j_2\rangle = 0 \\ \left[\widehat{J}_z, \widehat{\mathcal{F}}_{j_1, j_2}^{(n)} \right] = -\hbar n \widehat{\mathcal{F}}_{j_1, j_2}^{(n)} \end{cases}} \quad . \quad (7.21)$$

We can begin to solve these for the two-particle case (and later the N-particle case). First, we will find a general form for the alignment lowering operator that will satisfy the second criterion above. Using the operator relation (A.2) and the ladder operator relation (B.4),

$$\left[\widehat{J}_z, \widehat{J}_-^p \right] = \sum_{k=0}^{p-1} \widehat{J}_-^{p-1-k} \left[\widehat{J}_z, \widehat{J}_- \right] \widehat{J}_-^k = \sum_{k=0}^{p-1} \widehat{J}_-^{p-1-k} \left(-\hbar \widehat{J}_- \right) \widehat{J}_-^k \quad .$$

This expression evaluates straightforwardly to:

$$\left[\widehat{J}_z, \widehat{J}_-^p \right] = -\hbar p \widehat{J}_-^p \quad , \quad (7.22)$$

which is quite similar to the second relation in (7.21), but is not quite general enough to satisfy both conditions. Let's instead consider the following commutator:

$$\begin{aligned} \left[\widehat{J}_{1z} + \widehat{J}_{2z}, \widehat{J}_{1-}^p \widehat{J}_{2-}^q \right] &= \left[\widehat{J}_{1z}, \widehat{J}_{1-}^p \right] \widehat{J}_{2-}^q + \widehat{J}_{1-}^p \left[\widehat{J}_{2z}, \widehat{J}_{2-}^q \right] \\ &= -\hbar p \widehat{J}_{1-}^p \widehat{J}_{2-}^q - \hbar q \widehat{J}_{1-}^p \widehat{J}_{2-}^q \quad . \end{aligned}$$

This result simplifies to:

$$\left[\widehat{J}_z, \widehat{J}_{1-}^p \widehat{J}_{2-}^q \right] = -\hbar(p+q) \widehat{J}_{1-}^p \widehat{J}_{2-}^q . \quad (7.23)$$

With the constraint that $p + q = n$, we can write a sufficiently general ansatz for the alignment lowering operator. We will use a weighted sum over all products $\widehat{J}_{1-}^p \widehat{J}_{2-}^q$ where $p + q = n$:

$$\widehat{\mathcal{F}}_{j_1, j_2}^{(n)} = \sum_{l=0}^n \zeta_l^{(n)} \widehat{J}_{1-}^{n-l} \widehat{J}_{2-}^l . \quad (7.24)$$

Now we can find the exact form of the alignment lowering operator by applying the first criterion in equation (7.21). First we will need a commutator relation between the raising operator and a product of lowering operators. Using the basic ladder operator relation (B.5),

$$\begin{aligned} \left[\widehat{J}_{i+}, \widehat{J}_{i-}^p \right] |j_i, j_i\rangle &= \sum_{k=0}^{p-1} \widehat{J}_{i-}^{p-1-k} \left[\widehat{J}_{i+}, \widehat{J}_{i-} \right] \widehat{J}_{i-}^k |j_i, j_i\rangle \\ &= \sum_{k=0}^{p-1} \widehat{J}_{i-}^{p-1-k} \left(\frac{2}{\hbar} \widehat{J}_{iz} \right) \widehat{J}_{i-}^k |j_i, j_i\rangle \\ &= \sum_{k=0}^{p-1} \widehat{J}_{i-}^{p-1-k} \left(\frac{2}{\hbar} \hbar(j_i - k) \right) \widehat{J}_{i-}^k |j_i, j_i\rangle \\ &= 2 \left(\sum_{k=0}^{p-1} j_i - k \right) \widehat{J}_{i-}^{p-1} |j_i, j_i\rangle . \end{aligned}$$

The final summation evaluates as an arithmetic series, and we have:

$$\left[\widehat{J}_{i+}, \widehat{J}_{i-}^p \right] |j_i, j_i\rangle = (2j_i + 1 - p)(p) \widehat{J}_{i-}^{p-1} |j_i, j_i\rangle . \quad (7.25)$$

Now, using this relation, we let the commutator of the coupled raising operator and the alignment operator act on the maximally aligned top ket:

$$\begin{aligned}
& \left[\widehat{J}_+, \widehat{\mathcal{F}}_{j_1, j_2}^{(n)} \right] |j_1 + j_2, j_1 + j_2\rangle = \left[\widehat{J}_{1+} + \widehat{J}_{2+}, \sum_{l=0}^n \zeta_l^{(n)} \widehat{J}_{1-}^{n-l} \widehat{J}_{2-}^l \right] |j_1, j_1; j_2, j_2\rangle \\
& = \sum_{l=0}^n \zeta_l^{(n)} \left[\widehat{J}_{1+}, \widehat{J}_{1-}^{n-l} \right] \widehat{J}_{2-}^l |j_1, j_1; j_2, j_2\rangle + \sum_{l=0}^n \zeta_l^{(n)} \widehat{J}_{1-}^{n-l} \left[\widehat{J}_{2+}, \widehat{J}_{2-}^l \right] |j_1, j_1; j_2, j_2\rangle \\
& = \sum_{l=0}^{n-1} \zeta_l^{(n)} (2j_1 + 1 - n + l)(n - l) \widehat{J}_{1-}^{n-l-1} \widehat{J}_{2-}^l |j_1, j_1; j_2, j_2\rangle \\
& \quad + \sum_{l=1}^n \zeta_l^{(n)} (2j_2 + 1 - l)(l) \widehat{J}_{1-}^{n-l} \widehat{J}_{2-}^{l-1} |j_1, j_1; j_2, j_2\rangle \quad ,
\end{aligned}$$

where, in the last step, we have dropped the vanishing terms at the boundaries from the two summations. Directly applying the first criterion from equation (7.21), the left-hand side must vanish. The summations on the right-hand side can be grouped together by shifting the index on the second summation backwards by one:

$$\begin{aligned}
0 & = \sum_{l=0}^{n-1} \left[\zeta_l^{(n)} (2j_1 + 1 - n + l)(n - l) + \zeta_{l+1}^{(n)} (2j_2 - l)(l + 1) \right] \widehat{J}_{1-}^{n-l-1} \widehat{J}_{2-}^l |j_1, j_1; j_2, j_2\rangle \\
& \implies \zeta_l^{(n)} (2j_1 + 1 - n + l)(n - l) + \zeta_{l+1}^{(n)} (2j_2 - l)(l + 1) = 0 \quad , \quad (7.26)
\end{aligned}$$

and now we have a recurrence relation which is straightforward to solve algebraically:

$$\begin{aligned}
\frac{\zeta_{l+1}^{(n)}}{\zeta_l^{(n)}} & = -\frac{(n - l)(2j_1 + l - n + 1)}{(l + 1)(2j_2 - l)} \quad , \\
\frac{\zeta_l^{(n)}}{\zeta_0^{(n)}} & = \prod_{\lambda=0}^{l-1} \frac{\zeta_{\lambda+1}}{\zeta_\lambda} = (-1)^l \prod_{\lambda=0}^{l-1} \frac{(n - \lambda)(2j_1 + \lambda - n + 1)}{(\lambda + 1)(2j_2 - \lambda)} \quad , \\
\frac{\zeta_l^{(n)}}{\zeta_0^{(n)}} & = (-1)^l \frac{n!(2j_1 - n + l)!(2j_2 - l)!}{(n - l)!l!(2j_1 - n)!(2j_2)!} \quad .
\end{aligned}$$

We have our solution up to a normalization constant:

$$\text{Let } N_{j_1, j_2}^{(n)} = \zeta_0^{(n)} \frac{n!}{(2j_1 - n)!(2j_2)!} .$$

Then we can write the alignment lowering operator as:

$$\widehat{\mathcal{F}}_{j_1, j_2}^{(n)} = N_{j_1, j_2}^{(n)} \sum_{l=0}^n (-1)^l \frac{(2j_1 - n + l)!(2j_2 - l)!}{(n - l)!l!} \widehat{J}_{1-}^{n-l} \widehat{J}_{2-}^l . \quad (7.27)$$

We can find a value for this normalization constant by imposing that the maximally aligned top ket will be mapped to a normalized ket:

$$\begin{aligned} \widehat{\mathcal{F}}_{j_1, j_2}^{(n)} |j_1, j_1; j_2, j_2\rangle &= N_{j_1, j_2}^{(n)} \sum_{l=0}^n (-1)^l \frac{(2j_1 - n + l)!(2j_2 - l)!}{(n - l)!l!} \\ &\quad \times \sqrt{\frac{(2j_1)!(n - l)!(2j_2)!l!}{(2j_1 - n + l)!(2j_2 - l)!}} |j_1, j_1 - n + l; j_2, j_2 - l\rangle \\ &= N_{j_1, j_2}^{(n)} \sqrt{(2j_1)!(2j_2)!} \sum_{l=0}^n (-1)^l \sqrt{\frac{(2j_1 - n + l)!(2j_2 - l)!}{(n - l)!l!}} |j_1, j_1 - n + l; j_2, j_2 - l\rangle \\ &\implies 1 = \left(N_{j_1, j_2}^{(n)}\right)^2 (2j_1)!(2j_2)! \sum_{l=0}^n \frac{(2j_1 - n + l)!(2j_2 - l)!}{(n - l)!l!} , \quad (7.28) \end{aligned}$$

where, in the last step, we have simply taken the square modulus of both sides. This summation can be evaluated, though in a somewhat roundabout way, by considering the action of the usual coupled lowering operator on the maximally aligned top ket. Applying the ladder operator relation

from (B.14):

$$\begin{aligned}
\widehat{J}_-^p |j_1 + j_2, j_1 + j_2\rangle &= \sum_{k=0}^p \frac{p!}{(p-k)!k!} \widehat{J}_1^{p-k} \widehat{J}_2^k |j_1, j_1; j_2, j_2\rangle \quad , \\
\sqrt{\frac{(2j_1 + 2j_2)!p!}{(2j_1 + 2j_2 - p)!}} |j_1 + j_2, j_1 + j_2 - p\rangle &= \sum_{k=0}^p \frac{p!}{(p-k)!k!} \\
&\quad \times \sqrt{\frac{(2j_1)!(p-k)!(2j_2)!k!}{(2j_1 - p + k)!(2j_2 - k)!}} |j_1, j_1 - p + k; j_2, j_2 - k\rangle \\
&= p! \sum_{k=0}^p \sqrt{\frac{(2j_1)!(2j_2)!}{(p-k)!k!(2j_1 - p + k)!(2j_2 - k)!}} |j_1, j_1 - p + k; j_2, j_2 - k\rangle \\
\Rightarrow \frac{(2j_1 + 2j_2)!}{(2j_1 + 2j_2 - p)!p!} &= \sum_{k=0}^p \frac{(2j_1)!(2j_2)!}{(p-k)!k!(2j_1 - p + k)!(2j_2 - k)!} \quad , \quad (7.29)
\end{aligned}$$

again, taking the square modulus of both sides in the last step. We will now show that, with some algebraic manipulation, the right-hand side of (7.29) can be made identical to the summation in (7.28). First, recognize the following equivalence of products:

$$\frac{a!}{(a-b)!} = \prod_{i=0}^{b-1} a - i = \prod_{i=0}^{b-1} a - b + 1 + i = (-1)^b \prod_{i=0}^{b-1} b - a - 1 - i \quad .$$

The left-most product can be expressed in terms of improper factorials:

$$\frac{a!}{(a-b)!} = (-1)^b \frac{(b-a-1)!}{(-a-1)!} \quad . \quad (7.30)$$

These are improper because the arguments of the factorials will always be negative on at least one side of the equation. However, we will treat this expression as a representation of the products in the line above. Suppose now that we let the arguments of the factorials in (7.29) be negative and

we applied our new identity (7.30). Then, (7.29) would become:

$$(-1)^p \frac{(p - 2j_1 - 2j_2 - 1)!}{(-2j_1 - 2j_2 - 1)!p!} = \sum_{k=0}^p \frac{(-1)^{p-k} (p - k - 2j_1 - 1)! (-1)^k (k - 2j_2 - 1)!}{(p - k)! k! (-2j_1 - 1)! (-2j_2 - 1)!} .$$

Now, with some substitutions, we can obtain a summation that is identical to the one in (7.28).

$$\begin{aligned} p &\rightarrow n \quad \& \quad k \rightarrow l \quad , \\ 2j_1 &\rightarrow -2j_2 + n - 1 \quad \& \quad 2j_2 \rightarrow -2j_1 + n - 1 \quad , \\ \frac{(2j_1 + 2j_2 - n + 1)!}{(2j_1 + 2j_2 - 2n + 1)!n!} &= \sum_{l=0}^n \frac{(2j_1 - n + l)! (2j_2 - l)!}{(n - l)! l! (2j_1 - n)! (2j_2 - n)!} . \end{aligned}$$

Then, by simply multiplying by a factor of $(2j_1 - n)! (2j_2 - n)!$, we can evaluate the desired summation:

$$\sum_{l=0}^n \frac{(2j_1 - n + l)! (2j_2 - l)!}{(n - l)! l!} = \frac{(2j_1 + 2j_2 - n + 1)! (2j_1 - n)! (2j_2 - n)!}{(2j_1 + 2j_2 - 2n + 1)! n!} . \quad (7.31)$$

Substituting this into (7.28) gives:

$$\Rightarrow 1 = \left(N_{j_1, j_2}^{(n)} \right)^2 (2j_1)! (2j_2)! \frac{(2j_1 + 2j_2 - n + 1)! (2j_1 - n)! (2j_2 - n)!}{(2j_1 + 2j_2 - 2n + 1)! n!} ,$$

and thus, the explicit form of our two-particle alignment lowering operator is:

$$\boxed{\widehat{\mathcal{J}}_{j_1, j_2}^{(n)} = N_{j_1, j_2}^{(n)} \sum_{l=0}^n (-1)^l \frac{(2j_1 - n + l)! (2j_2 - l)!}{(n - l)! l!} \widehat{J}_{1-}^{n-l} \widehat{J}_{2-}^l} . \quad (7.32)$$

Where $N_{j_1, j_2}^{(n)} = \sqrt{\frac{(2j_1 + 2j_2 - 2n + 1)! n!}{(2j_1 + 2j_2 - n + 1)! (2j_1 - n)! (2j_2 - n)! (2j_1)! (2j_2)!}}$

7.2 N particles

Generalizing the previous result to the case of N-particles presents a number of challenges. First, in contrast to the two-particle case where we could quantify the lowering with only one integer

n , we will now need an integer for every pair of particles in the system to account for each possible coupling of particles. The action of the alignment lowering operator on the maximally aligned top ket should then be expressed as:

$$\widehat{\mathcal{F}}_{\{j_a\}}^{\{n_{ab}\}} \left| J = \sum_{i=1}^N j_i, M = J \right\rangle = \left| J = \sum_{i=1}^N j_i - \frac{1}{2} \sum_{\substack{a,b=1 \\ a \neq b}}^N n_{ab}, M = J \right\rangle, \quad (7.33)$$

where the factor of $\frac{1}{2}$ is meant to account for the fact that only one integer is needed for a given pair, i.e. $n_{ab} = n_{ba}$.

The second commutator relation in (7.21) will be satisfied in the following way:

$$\left[\widehat{J}_z, \widehat{\mathcal{F}}_{\{j_a\}}^{\{n_{ab}\}} \right] = \left(-\frac{\hbar}{2} \sum_{\substack{a,b=1 \\ a \neq b}}^N n_{ab} \right) \widehat{\mathcal{F}}_{\{j_a\}}^{\{n_{ab}\}}. \quad (7.34)$$

Since every term is doubled in the sum, we can be sure that the scalar factor on the right-hand side will evaluate to a negative integer multiple of Planck's constant. Analogously to the two-particle case, this condition is satisfied by using the following ansatz for the form of the alignment lowering operator:

$$\widehat{\mathcal{F}}_{\{j_a\}}^{\{n_{ab}\}} = \sum_{\substack{\{l_{ab}=0\} \\ \{l_{ab}+l_{ba}=n_{ab}\}}}^{\{n_{ab}\}} \zeta_{\{l_{ab}\}}^{\{n_{ab}\}} \bigotimes_{a=1}^N \widehat{J}_{a-}^{\sum_{\substack{b=1 \\ b \neq a}}^N l_{ab}}. \quad (7.35)$$

Here, we have adopted some conventions which may be unfamiliar to the reader in order to solve our second challenge in the N-particle generalization: writing manageably sized expressions. First, the indices are themselves now indexed by which two particles they couple and by which lowering operator's exponent they appear in: the index l_{ab} appears in the exponent of the lowering operator \widehat{J}_{a-} and accounts for the coupling to the particle whose index is b . For clarity, we will refer to the indices l_{ab} as **coupling indices** and the indices a and b as **particle indices**. Secondly, the coupling indices are constrained so that $l_{ab} + l_{ba} = n_{ab}$ ($\forall a, b \in [1, N] \cap \mathbb{Z}$), denoted implicitly below the

lower bound of the summation sign. With this constraint, the coupling index l_{ab} will take values from the lower bound 0 to its corresponding upper bound n_{ab} ($\forall a, b \in [1, N] \cap \mathbb{Z}$). Lastly, the exponent of each lowering operator has been chosen so that the sum of the exponents of every lowering operator will equal the summation in (7.34), that is:

$$\sum_{a=1}^N \sum_{\substack{b=1 \\ b \neq a}}^N l_{ab} = \sum_{\substack{a,b=1 \\ b \neq a}}^N l_{ab} = \frac{1}{2} \sum_{\substack{a,b=1 \\ a \neq b}}^N n_{ab} . \quad (7.36)$$

To make all of this clear to the reader, we will write the ansatz explicitly for the three particle case:

$$\widehat{\mathcal{F}}_{j_1, j_2, j_3}^{(n_{12}, n_{23}, n_{31})} = \sum_{\substack{l_{12}, l_{23}, l_{31}=0 \\ \{l_{ab}+l_{ba}=n_{ab}\}}}^{n_{12}, n_{23}, n_{31}} \zeta_{j_1, j_2, j_3}^{(n_{12}, n_{23}, n_{31})} \widehat{J}_{1-}^{l_{12}+l_{13}} \widehat{J}_{2-}^{l_{21}+l_{23}} \widehat{J}_{3-}^{l_{31}+l_{32}} .$$

Before we begin applying the first commutator relation in (7.21), we will find it useful to make the following substitution:

$$\text{Let} \quad p_a = \sum_{\substack{b=1 \\ b \neq a}}^N l_{ab} . \quad (7.37)$$

Now, just as in the two-particle case, we use equation (7.25) to obtain:

$$\begin{aligned} & \left[\widehat{J}_+, \widehat{\mathcal{F}}_{\{j_a\}}^{\{n_{ab}\}} \right] |J, J\rangle = 0 , \\ & \sum_{k=1}^N \sum_{\substack{\{n_{ab}\} \\ \{l_{ab}=0\} \\ \{l_{ab}+l_{ba}=n_{ab}\}}} \zeta_{\{l_{ab}\}}^{\{n_{ab}\}} (2j_k + 1 - p_k)(p_k) \bigotimes_{a=1}^N \widehat{J}_{a-}^{p_a - \delta_{ka}} |J, J\rangle = 0 , \end{aligned}$$

where we have used a Kronecker delta, δ_{ka} , in the exponent of the lowering operator \widehat{J}_{a-} to account for the reduction of the power of the k 'th ladder operator. In the interest of brevity, we can make a further simplification by noting that, as long as $0 \leq n_{ab} \leq j_a + j_b - |j_a - j_b|$ ($\forall a, b \in [1, N] \cap \mathbb{Z}$), the ket $|J, J\rangle$ cannot be in the kernel of every operator in the summation above. Thus, we can say

that this sum of operators must evaluate to zero:

$$\sum_{k=1}^N \sum_{\substack{\{n_{ab}\} \\ \{l_{ab}=0\} \\ \{l_{ab}+l_{ba}=n_{ab}\}}} \zeta_{\{l_{ab}\}}^{\{n_{ab}\}} (2j_k + 1 - p_k)(p_k) \bigotimes_{a=1}^N \widehat{J}_{a-}^{p_a - \delta_{ka}} = 0 \quad , \quad (7.38)$$

Now, we expand one of the factors of p_k as a summation of the coupling indices and exchange the order of the first two summations:

$$\begin{aligned} 0 &= \sum_{k=1}^N \sum_{\substack{\{n_{ab}\} \\ \{l_{ab}\} \\ \{l_{ab}+l_{ba}=n_{ab}\}}} \zeta_{\{l_{ab}\}}^{\{n_{ab}\}} (2j_k + 1 - p_k) \left(\sum_{\substack{b=1 \\ b \neq k}}^N l_{kb} \right) \bigotimes_{a=1}^N \widehat{J}_{a-}^{p_a - \delta_{ka}} \\ &= \sum_{\substack{\{n_{ab}\} \\ \{l_{ab}=0\} \\ \{l_{ab}+l_{ba}=n_{ab}\}}} \zeta_{\{l_{ab}\}}^{\{n_{ab}\}} \sum_{k=1}^N \sum_{\substack{b=1 \\ b \neq k}}^N (2j_k + 1 - p_k)(l_{kb}) \bigotimes_{a=1}^N \widehat{J}_{a-}^{p_a - \delta_{ka}} \quad . \end{aligned}$$

The next step may be challenging for the reader to follow in the more general case, so we have written it explicitly in the three-particle case to make the reasoning apparent. The summation above would be written as follows in the case of three-particles:

$$\begin{aligned} 0 &= \sum_{l_{12}, l_{23}, l_{31}=0}^{n_{12}, n_{23}, n_{31}} \zeta_{l_{12}, l_{23}, l_{31}}^{(n_{12}, n_{23}, n_{31})} \left[(2j_1 + 1 - p_1)(l_{12} + l_{13}) \widehat{J}_{1-}^{p_1-1} \widehat{J}_{2-}^{p_2} \widehat{J}_{3-}^{p_3} \right. \\ &\quad + (2j_2 + 1 - p_2)(l_{21} + l_{23}) \widehat{J}_{1-}^{p_1} \widehat{J}_{2-}^{p_2-1} \widehat{J}_{3-}^{p_3} \\ &\quad \left. + (2j_3 + 1 - p_3)(l_{31} + l_{32}) \widehat{J}_{1-}^{p_1} \widehat{J}_{2-}^{p_2} \widehat{J}_{3-}^{p_3-1} \right] \quad . \end{aligned}$$

From here, we want to extract a recurrence relation analogous to (7.26) for the coefficients $\zeta_{\{l_{ab}\}}^{\{n_{ab}\}}$ or, in this case, $\zeta_{l_{12}, l_{23}, l_{31}}^{(n_{12}, n_{23}, n_{31})}$. This will require that we arrange the coupling indices l_{ab} by pairs:

$$0 = \sum_{l_{12}, l_{23}, l_{31}=0}^{n_{12}, n_{23}, n_{31}} \zeta_{l_{12}, l_{23}, l_{31}}^{(n_{12}, n_{23}, n_{31})} \left\{ \left[(2j_1 + 1 - p_1)(l_{12}) \widehat{J}_{1-}^{p_1-1} \widehat{J}_{2-}^{p_2} \widehat{J}_{3-}^{p_3} \right. \right. \\ \left. \left. + (2j_2 + 1 - p_2)(l_{21}) \widehat{J}_{1-}^{p_1} \widehat{J}_{2-}^{p_2-1} \widehat{J}_{3-}^{p_3} \right] \right. \\ \left. + \left[(2j_2 + 1 - p_2)(l_{23}) \widehat{J}_{1-}^{p_1} \widehat{J}_{2-}^{p_2-1} \widehat{J}_{3-}^{p_3} \right. \right. \\ \left. \left. + (2j_3 + 1 - p_3)(l_{32}) \widehat{J}_{1-}^{p_1} \widehat{J}_{2-}^{p_2} \widehat{J}_{3-}^{p_3-1} \right] \right. \\ \left. + \left[(2j_3 + 1 - p_3)(l_{31}) \widehat{J}_{1-}^{p_1} \widehat{J}_{2-}^{p_2} \widehat{J}_{3-}^{p_3-1} \right. \right. \\ \left. \left. + (2j_1 + 1 - p_1)(l_{21}) \widehat{J}_{1-}^{p_1-1} \widehat{J}_{2-}^{p_2} \widehat{J}_{3-}^{p_3} \right] \right\} .$$

It should be clear now that this rearrangement is simply a re-indexing of the summation over particles:

$$0 = \sum_{\substack{\{n_{ab}\} \\ \{l_{ab}=0\} \\ \{l_{ab}+l_{ba}=n_{ab}\}}} \zeta_{\{l_{ab}\}}^{\{n_{ab}\}} \frac{1}{2} \sum_{\substack{a', b'=1 \\ a' \neq b'}}^N \left[(2j_{a'} + 1 - p_{a'}) (l_{a'b'}) \bigotimes_{a'=1}^N \widehat{J}_{a'-}^{p_{a'} - \delta_{a'a}} \right. \\ \left. + (2j_{b'} + 1 - p_{b'}) (l_{b'a'}) \bigotimes_{b'=1}^N \widehat{J}_{b'-}^{p_{b'} - \delta_{b'b}} \right] .$$

Now it should be clear that we can make the following exchange between the sum over particle indices and the sum over coupling indices:

$$0 = \frac{1}{2} \sum_{\substack{a', b'=1 \\ a' \neq b'}}^N \sum_{\substack{\{n_{ab}\} \\ \{l_{ab}=0\} \\ \{l_{ab}+l_{ba}=n_{ab}\}}} \zeta_{\{l_{ab}\}}^{\{n_{ab}\}} \left[(2j_{a'} + 1 - p_{a'}) (l_{a'b'}) \bigotimes_{a'=1}^N \widehat{J}_{a'-}^{p_{a'} - \delta_{a'a}} \right. \\ \left. + (2j_{b'} + 1 - p_{b'}) (l_{b'a'}) \bigotimes_{b'=1}^N \widehat{J}_{b'-}^{p_{b'} - \delta_{b'b}} \right] .$$

In order to make the recurrence relation's dependence on the coupling index l_{ab} explicit, we will make the following change of variables:

$$\text{Let} \quad p_{cd} = p_c - l_{cd} = \sum_{\substack{d'=1 \\ d' \neq c, d}}^N l_{cd'} \quad . \quad (7.39)$$

Now, our expression reads:

$$0 = \frac{1}{2} \sum_{\substack{a', b'=1 \\ a' \neq b'}}^N \sum_{\substack{\{n_{ab}\} \\ \{l_{ab}=0\} \\ \{l_{ab}+l_{ba}=n_{ab}\}}} \zeta_{\{l_{ab}\}}^{\{n_{ab}\}} \left[(2j_{a'} + 1 - l_{a'b'} - p_{a'b'}) (l_{a'b'}) \bigotimes_{a'=1}^N \widehat{J}_{a'-}^{p_{a'} - \delta_{a'a}} \right. \\ \left. + (2j_{b'} + 1 - l_{b'a'} - p_{b'a'}) (l_{b'a'}) \bigotimes_{b'=1}^N \widehat{J}_{b'-}^{p_{b'} - \delta_{b'b}} \right] .$$

There remains one step, which is to shift the indices so that the exponents on the lowering operators can be matched and the summation can be expressed as one coefficient on each product of lowering operators. We also need the recurrence relation to depend on only one coupling index so that it may be solved by one product. We can satisfy these two requirements with the following substitutions:

$$l_{a'b'} \rightarrow l_{a'b'} + 1 \quad \& \quad l_{b'a'} \rightarrow n_{a'b'} - l_{a'b'} \quad .$$

Now, we have the desired expression:

$$0 = \frac{1}{2} \sum_{\substack{a', b'=1 \\ a' \neq b'}}^N \sum_{\substack{\{n_{ab} - \delta_{a'b'}\} \\ \{l_{ab}=0\} \\ \{l_{ab}+l_{ba}=n_{ab}\}}} \left(\bigotimes_{b'=1}^N \widehat{J}_{b'-}^{p_{b'} - \delta_{b'b}} \right) \left[\zeta_{\{l_{ab} + \delta_{a'b'}\}}^{\{n_{ab}\}} (2j_{a'} - l_{a'b'} - p_{a'b'}) (l_{a'b'} + 1) \right. \\ \left. + \zeta_{\{l_{ab}\}}^{\{n_{ab}\}} (2j_{b'} - n_{a'b'} + l_{b'a'} - p_{b'a'}) (n_{a'b'} - l_{a'b'}) \right] ,$$

where we have used a Kronecker delta in the subscript of the coefficient $\zeta_{\{l_{ab} + \delta_{a'b'}\}}^{\{n_{ab}\}}$ to account for the shifting of the particular coupling index $l_{a'b'}$. This result immediately gives the recurrence

relation:

$$\begin{aligned} & \zeta_{\{l_{ab}\}}^{\{n_{ab}\}} (2j_{b'} - p_{b'a'} + 1 - n_{a'b'} + l_{a'b'}) (n_{a'b'} - l_{a'b'}) \\ & + \zeta_{\{l_{ab} + \delta_{a'b'}\}}^{\{n_{ab}\}} (2j_{a'} - p_{a'b'} - l_{a'b'}) (l_{a'b'} + 1) = 0 \quad . \end{aligned} \quad (7.40)$$

This recurrence relation can be now be solved straightforwardly by a product, as was done in the two-particle case, by making the substitutions $2j_1 \rightarrow 2j_{b'} - p_{b'a'}$ and $2j_2 \rightarrow 2j_{a'} - p_{a'b'}$:

$$\begin{aligned} & \frac{\zeta_{\{l_{ab} + \delta_{a'b'}\}}^{\{n_{ab}\}}}{\zeta_{\{l_{ab}\}}^{\{n_{ab}\}}} = - \frac{(n_{a'b'} - l_{a'b'}) (2j_{b'} - p_{b'a'} - n_{a'b'} + l_{a'b'} + 1)}{(l_{a'b'} + 1) (2j_{a'} - p_{a'b'} - l_{a'b'})} \\ \implies & \frac{\zeta_{\{l_{ab}\}}^{\{n_{ab}\}}}{\zeta_{\{l_{ab}, l_{a'b'}=0\}}^{\{n_{ab}\}}} = (-1)^{l_{a'b'}} \frac{(n_{a'b'})! (2j_{b'} - p_{b'a'} - n_{a'b'} + l_{a'b'})! (2j_{a'} - p_{a'b'} - l_{a'b'})!}{(n_{a'b'} - l_{a'b'})! (l_{a'b'})! (2j_{b'} - p_{b'a'} - n_{a'b'})! (2j_{a'} - p_{a'b'})!} \quad . \end{aligned}$$

Just as before, we can absorb the constant terms into a normalization constant $N_{j_{a'}, j_{b'}}^{(n_{a'b'})}$. The partial solution will be given by:

$$\zeta_{\{l_{ab}\}}^{\{n_{ab}\}} = N_{j_{a'}, j_{b'}}^{(n_{a'b'})} \zeta_{\{l_{ab}, l_{a'b'}=0\}}^{\{n_{ab}\}} (-1)^{l_{a'b'}} \frac{\left(2j_{a'} - \sum_{\substack{b'=0 \\ b' \neq a'}}^N l_{a'b'}\right)! \left(2j_{b'} - \sum_{\substack{a'=0 \\ a' \neq b'}}^N l_{b'a'}\right)!}{(l_{a'b'})! (l_{b'a'})!} \quad . \quad (7.41)$$

There still remains the factor of $\zeta_{\{l_{ab}, l_{a'b'}=0\}}^{\{n_{ab}\}}$, which carries the dependence on all other coupling indices $l_{ab} \neq l_{a'b'}$. To acquire the full solution, first we note that only one factor of $(2j_a - \sum_{\substack{b=0 \\ b \neq a}}^N l_{ab})!$ can appear for each particle a , otherwise the recurrence relation (7.40) will not be satisfied in general. Additionally, one factor of $(l_{ab})!$ must appear for every possible choice of particle a and b to satisfy (7.40) for all possible particle pairs. Lastly, for each particle pair, there must be only one factor of $(-1)^{l_{ab}}$ as a result of the product, which will require us to make a choice about which index to make this factor dependent on. Therefore, the full solution is given by:

$$\zeta_{\{l_{ab}\}}^{\{n_{ab}\}} = N_{\{j_a\}}^{\{n_{a,b}\}} \left(\prod_{(a,b)} (-1)^{l_{ab}} \right) \prod_{a=1}^N \frac{\left(2j_a - \sum_{\substack{b=1 \\ b \neq a}}^N l_{ab}\right)!}{\prod_{\substack{b=1 \\ b \neq a}}^N (l_{ab}!)}, \quad (7.42)$$

where, in the factor of $(-1)^{\sum_{(a,b)} l_{ab}}$, we have made the choice to sum over particle indices which belong to the following set of ordered pairs:

$$\{(a, b) \in [1, N] \cap \mathbb{Z} : a > b \iff (-1)^a = (-1)^b\} . \quad (7.43)$$

This choice was made to agree with the convention we chose for our preferred coupling indices in the three-particle case, i.e. l_{12} , l_{23} , and l_{31} . For clarity, the full solution for the three-particle case is written below:

$$\begin{aligned} \widehat{\mathcal{F}}_{j_1, j_2, j_3}^{(n_{12}, n_{23}, n_{31})} = & N_{j_1, j_2, j_3}^{(n_{12}, n_{23}, n_{31})} \sum_{\substack{l_{12}, l_{23}, l_{31}=0 \\ \{l_{ab}+l_{ba}=n_{ab}\}}} (-1)^{l_{12}+l_{23}+l_{31}} \frac{(2j_1-l_{12}-l_{13})!(2j_2-l_{21}-l_{23})!(2j_3-l_{31}-l_{32})!}{(l_{12})!(l_{13})!(l_{21})!(l_{23})!(l_{31})!(l_{32})!} \\ & \times \widehat{J}_{1-}^{l_{12}+l_{13}} \widehat{J}_{2-}^{l_{21}+l_{23}} \widehat{J}_{3-}^{l_{31}+l_{32}} . \end{aligned} \quad (7.44)$$

7.3 Exchange symmetries

Now that we have the general N -particle solution (7.42) for the coefficient $\zeta_{\{l_{ab}\}}^{\{n_{ab}\}}$ in the summation (7.35), we can derive the particle exchange symmetry properties of the alignment lowering operator, $\widehat{\mathcal{F}}_{\{j_a\}}^{\{n_{ab}\}}$. Consider the case that the quantum numbers j_a are all equal. Recall that a particular alignment family of kets is generated from its top ket by the lowering operators as in (7.17). Because the total ladder operator is now symmetric under the exchange of any two particles, the exchange symmetry is the same for all kets within the alignment family. Additionally, by applying the alignment lowering operator, one can generate any alignment family from the top ket of the maximally aligned family of kets $|J, J\rangle$ as shown in equation (7.33). In the case that all the quantum numbers j_a are the same, the ket $|J, J\rangle = \bigotimes_{a=1}^N |j_a\rangle$ is completely symmetric under particle exchange. Therefore, the exchange symmetry of the generated alignment family must be carried by the alignment lowering operator. More precisely, if $\widehat{\mathcal{F}}_{\{j_a\}}^{\{n_{ab}\}}$ maps $|J, J\rangle$ to a symmetric alignment family, then $\widehat{\mathcal{F}}_{\{j_a\}}^{\{n_{ab}\}}$ is symmetric and, if $\widehat{\mathcal{F}}_{\{j_a\}}^{\{n_{ab}\}}$ maps $|J, J\rangle$ to an antisymmetric alignment family, then $\widehat{\mathcal{F}}_{\{j_a\}}^{\{n_{ab}\}}$ is antisymmetric. Since we are interested in the angular momentum states of electrons, which are fermions, the state is physical only when it is antisymmetric under particle exchange. Therefore, *we can determine the allowed alignment families by determining the symmetries of the*

alignment lowering operator. We should note, before proceeding, that the alignment lowering operator would have to be symmetrized by summing over all permutations of the integers n_{ab} . We will see, however, that this fact will not effect results of this section.

Now, consider the factor of $(-1)^{l_{a'b'}}$ in the product $\prod_{(a,b)}(-1)^{l_{ab}}$ in equation (7.42) with the particular choice of ordered pairs (a, b) described in (7.43) and the particular choice of particles a' and b' . If all j_a are the same, then exchanging the particles a' and b' in the summation (7.35) for $\widehat{\mathcal{F}}_{\{j_a\}}^{\{n_{ab}\}}$ will only change this factor exactly as follows:

$$\begin{aligned} (-1)^{l_{a'b'}} &\rightarrow (-1)^{l_{b'a'}} \\ &= (-1)^{n_{a'b'} - l_{a'b'}} \\ &= (-1)^{n_{a'b'}} (-1)^{-l_{a'b'}} \\ &= (-1)^{n_{a'b'}} (-1)^{l_{a'b'}} \quad . \end{aligned}$$

Then the factor is transforms as:

$$(-1)^{l_{a'b'}} \rightarrow (-1)^{n_{a'b'}} (-1)^{l_{a'b'}} \quad , \quad (7.45)$$

which means that the alignment lowering operator will transform as follows:

$$\widehat{\mathcal{F}}_{\{j_a\}}^{\{n_{ab}\}} \rightarrow (-1)^{n_{a'b'}} \widehat{\mathcal{F}}_{\{j_a\}}^{\{n_{ab}\}} \quad , \quad (7.46)$$

and, therefore, the symmetry of the alignment lowering operator is given by the parity of the integers n_{ab} . Then, we can conclude that *the allowed alignment families generated are those generated by an alignment lowering operator whose integer parameters n_{ab} are all odd*.

In order to determine the allowed LS terms, the integers n_{ab} will have to be expressed in terms of the quantum numbers for the orbital angular momentum, l , the spin angular momentum $s = \frac{1}{2}$, and the respective totals, L and S , which quantify the orbital and spin alignments (respectively) of all the electrons. We will show this for the two-particle case and leave the N -particle case for

future work. For the two-particle case, we can take the set of possible J values from (7.11) and let $j_1 = j_2 = j$:

$$J \in \{2j - n : n \in \mathbb{Z}, 0 \leq n \leq 2j\}$$

$$\implies n = 2j - J \quad . \quad (7.47)$$

Now, in the particular case that the angular momenta and the spins of two electrons were coupled, we would have an allowed state given by:

$$\left| 2l - \lambda, 2\left(\frac{1}{2}\right) - \sigma \right\rangle = \widehat{\mathcal{L}}_{l,l}^{(\lambda)} \otimes \widehat{\mathcal{S}}_{\frac{1}{2},\frac{1}{2}}^{(\sigma)} \left| l, \frac{1}{2} \right\rangle_1 \otimes \left| l, \frac{1}{2} \right\rangle_2 \quad . \quad (7.48)$$

By the same logic as in (7.46),

$$\widehat{\mathcal{L}}_{l,l}^{(\lambda)} \otimes \widehat{\mathcal{S}}_{\frac{1}{2},\frac{1}{2}}^{(\sigma)} \rightarrow (-1)^\lambda (-1)^\sigma \widehat{\mathcal{L}}_{l,l}^{(\lambda)} \otimes \widehat{\mathcal{S}}_{\frac{1}{2},\frac{1}{2}}^{(\sigma)} \quad .$$

Thus, $\lambda + \sigma = 2(l + \frac{1}{2}) - (L + S)$ must be odd. If we simplified this result further we would say:

$$(L + S) \bmod 2 = 0 \quad (7.49)$$

The rule that $L + S$ must be even for two equivalent electrons is derived in many textbook introductions to quantum mechanics and serves as quick check that our current approach agrees with established results. In future work, it is our intention to check the alignment lowering operator we have constructed in the N -particle case against the allowed LS terms that have been tabulated.

Chapter 8

Conclusion

It has been shown that the problem of accurate near-ionization threshold atomic processes and, consequently, the problem of low-temperature DR in photoionized plasmas can be greatly improved for low charge states of light elements by the decision tree algorithm described in Chapter 3. It is clear that the configuration sequences chosen by CRISTAL for the Boron-like and Beryllium-like isoelectronic sequences will consistently converge on the tabulated energies. Additionally, the number of configurations now grows as the number of orbitals to the power of the number of electrons in the valence n -shell, where, before, the growth went as the number of orbitals to the power of the total number of electrons in the ion.

We have proven in Chapter 5 that the optimum configuration sequence chosen by CRISTAL will be invariant along an isoelectronic sequence. Then, in principle, one could use the tabulated energies for each neutral element in the periodic table and use CRISTAL to find the optimum configuration sequence for each isoelectronic sequence. In practice, isoelectronic sequences with more than 3 electrons in the valence n -shell will require configuration sequences that still grow too quickly for a typical computing cluster to calculate. We can, however, still test the remaining cases where there are 3 or fewer electrons in the valence n -shell, i.e. Sodium-like, Magnesium-like, Aluminum-like, Copper-like, Zinc-like, Gallium-like, Promethium-like, Samarium-like, and Europium-like. Improving on the currently archived low temperature DR rate coefficients for these systems would allow them to be used in modeling and diagnostic codes, to improve abundances and other diagnostics of photoionized plasmas.

CRISTAL has thus far only been used on a nonrelativistic, homogeneous central-field approximated Hamiltonian. We could, in principle, improve the accuracy further by using a fully relativistic

code (e.g. GRASP [60]) for generating the configuration state functions and/or diagonalizing a relativistic Hamiltonian. Including relativistic effects will be a topic for future work.

As shown in Chapter 6, the current method for calculating the transition rate, Fermi's Golden Rule, is a first-order approximation to the Dyson series. Using the method that we derived, we can calculate an upper bound for the error of Fermi's Golden rule. This method would be a useful uncertainty diagnostic in future DR rate calculations, which we would hope to test for some ions in the future.

A notable benefit to using a large CI model is the ability to model the emission from doubly excited (and more highly excited) states such as those responsible for satellite lines. It has proven to be essential, particularly in X-ray astrophysical spectroscopy [87, 88] and impurity spectroscopy for tokamak divertors [89, 90], to accurately account for satellite line emission in any spectroscopic diagnostics. High resolution X-ray spectra have shown that the current satellite line data in astrophysical databases is often not sufficiently accurate to determine plasma properties from fits to spectral data [91]. The current XRISM/Resolve X-ray telescope has much higher resolution than was available in previous missions. In addition, future missions (Athena/XIFU and Lynx/LXM) will also have high resolution detectors. Analyzing these results will require wavelength accuracy of mÅ or less. Satellite lines are potentially very useful electron temperature diagnostics when compared against the intensity of resonance lines [92].

In 2010, Robicheaux proposed a mechanism for below-threshold recombination [93]. Nemer observed evidence for this mechanism in planetary nebulae [94]. The mechanism depends on an energy overlap between the thermally broadened resonances from a singly excited Rydberg sequence near its ionization limit and those of a doubly excited Rydberg sequence. Thus, modeling such a transition can be made feasible with the improved accuracy of the doubly excited states calculated by CRISTAL allowing future studies in this area.

Overall, a decision tree algorithm is a powerful tool for atomic structure calculations and opens up promising opportunities for future research directions.

Bibliography

- [1] NASA, ESA, HEIC, and The Hubble Heritage Team (STScI/AURA).
- [2] A. Kramida, Yu. Ralchenko, J. Reader, and NIST ASD Team. NIST Atomic Spectra Database (ver. 5.12), [Online]. Available: <https://physics.nist.gov/asd> [2025, November 7]. National Institute of Standards and Technology, Gaithersburg, MD., 2024.
- [3] R. B. C. Henry, Karen B. Kwitter, Anne E. Jaskot, Bruce Balick, Michael A. Morrison, and Jacquelynne B. Milingo. Abundances of Galactic Anticenter Planetary Nebulae and the Oxygen Abundance Gradient in the Galactic Disk. *The Astrophysical Journal*, 724(1):748–761, November 2010.
- [4] R. L. Kingsburgh and M. J. Barlow. Elemental abundances for a sample of southern galactic planetary nebulae. *Monthly Notices of the Royal Astronomical Society*, 271:257–299, November 1994.
- [5] W. J. Maciel, R. D. D. Costa, and O. Cavichia. Radial abundance gradients from planetary nebulae at different distances from the galactic plane. *arXiv*, 51:165, October 2015.
- [6] Letizia Stanghellini and Misha Haywood. Galactic Planetary Nebulae as Probes of Radial Metallicity Gradients and Other Abundance Patterns. *The Astrophysical Journal*, 862(1):45, July 2018.
- [7] Quentin A. Parker. Planetary nebulae and how to find them: A concise review. *Frontiers in Astronomy and Space Sciences*, Volume 9 - 2022, 2022.
- [8] N. Erzincan, N. Aksaker, A. Akyuz, and Q. Parker. Analysis of Planetary Nebulae in the Milky Way: Physical Properties, Chemical Abundances, and Galactic Distributions. *arXiv e-prints*, page arXiv:2510.14149, October 2025.

- [9] Shuyu Tan, Quentin A. Parker, Albert A. Zijlstra, and Bryan Rees. A catalogue of planetary nebulae chemical abundances in the Galactic bulge. *Monthly Notices of the Royal Astronomical Society*, 527(3):6363–6387, January 2024.
- [10] O. Cavichia, R. D. D. Costa, W. J. Maciel, and M. Mollá. The population of planetary nebulae near the Galactic Centre: chemical abundances. *Monthly Notices of the Royal Astronomical Society*, 468(1):272–290, June 2017.
- [11] XinPei Lu, Peter J. Bruggeman, Stephan Reuter, George Naidis, Annemie Bogaerts, Mounir Laroussi, Michael Keidar, Eric Robert, Jean-Michel Pouvesle, DaWei Liu, and Kostya (Ken) Ostrikov. Grand challenges in low temperature plasmas. *Frontiers in Physics*, Volume 10 - 2022, 2022.
- [12] Gloria Delgado-Inglada, Christophe Morisset, and Grażyna Stasińska. Ionization correction factors for planetary nebulae – i. using optical spectra. *Monthly Notices of the Royal Astronomical Society*, 440(1):536–554, March 2014.
- [13] G. J. Ferland, M. Chatzikos, F. Guzmán, M. L. Lykins, P. A. M. van Hoof, R. J. R. Williams, N. P. Abel, N. R. Badnell, F. P. Keenan, R. L. Porter, and P. C. Stancil. The 2017 Release Cloudy. *Revista Mexicana de Astronomía y Astrofísica*, 53:385–438, October 2017.
- [14] T. R. Kallman and P. Palmeri. Atomic data for x-ray astrophysics. *Rev. Mod. Phys.*, 79:79–133, Jan 2007.
- [15] Smaranika Banerjee, Anders Jerkstrand, Nigel Badnell, Quentin Pognan, Niamh Ferguson, and Jon Grumer. Nebular spectra of kilonovae with detailed recombination rates – i. light r-process composition, 2025.
- [16] Randall K. Smith, Nancy S. Brickhouse, Duane A. Liedahl, and John C. Raymond. Collisional Plasma Models with APEC/APED: Emission-Line Diagnostics of Hydrogen-like and Helium-like Ions. *The Astrophysical Journal Letters*, 556(2):L91–L95, August 2001.

- [17] S. B. Kraemer, G. J. Ferland, and J. R. Gabel. The effects of low-temperature dielectronic recombination on the relative populations of the Fe m-shell states. *The Astrophysical Journal*, 604(2):556, apr 2004.
- [18] Hagai Netzer. The iron unresolved transition array in active galactic nuclei. *The Astrophysical Journal*, 604(2):551–555, April 2004.
- [19] N. R. Badnell. Dielectronic recombination of Fe $3p^q$ ions: A key ingredient for describing x-ray absorption in active galactic nuclei. *The Astrophysical Journal*, 651(1):L73–L76, October 2006.
- [20] E. W. Schmidt, S. Schippers, A. Müller, M. Lestinsky, F. Sprenger, M. Grieser, R. Repnow, A. Wolf, C. Brandau, D. Lukić, M. Schnell, and D. W. Savin. Electron-Ion Recombination Measurements Motivated by AGN X-Ray Absorption Features: Fe XIV Forming Fe XIII. *The Astrophysical Journal Letters*, 641(2):L157–L160, April 2006.
- [21] A. W. Leonard. Plasma detachment in divertor tokamaks. *Plasma Physics and Controlled Fusion*, 60(4):044001, April 2018.
- [22] J. Karhunen, A. Holm, B. Lomanowski, V. Solokha, S. Aleiferis, P. Carvalho, M. Groth, K. D. Lawson, A. G. Meigs, A. Shaw, and JET Contributors. Experimental distinction of the molecularly induced Balmer emission contribution and its application for inferring molecular divertor density with 2D filtered camera measurements during detachment in JET L-mode plasmas. *Plasma Physics and Controlled Fusion*, 64(7):075001, July 2022.
- [23] N. R. Badnell, M. G. O’Mullane, H. P. Summers, Z. Altun, M. A. Bautista, J. Colgan, T. W. Gorczyca, D. M. Mitnik, M. S. Pindzola, and O. Zatsarinny. Dielectronic recombination data for dynamic finite-density plasmas. I. Goals and methodology. *Astronomy and Astrophysics*, 406:1151–1165, August 2003.

- [24] O. Zatsarinny, T. W. Gorczyca, K. T. Korista, N. R. Badnell, and D. W. Savin. Dielectronic recombination data for dynamic finite-density plasmas. II. The oxygen isoelectronic sequence. *Astronomy and Astrophysics*, 412:587–595, December 2003.
- [25] J. Colgan, M. S. Pindzola, A. D. Whiteford, and N. R. Badnell. Dielectronic recombination data for dynamic finite-density plasmas. III. The beryllium isoelectronic sequence. *Astronomy and Astrophysics*, 412:597–601, December 2003.
- [26] O. Zatsarinny, T. W. Gorczyca, K. T. Korista, N. R. Badnell, and D. W. Savin. Dielectronic recombination data for dynamic finite-density plasmas. IV. The carbon isoelectronic sequence. *Astronomy and Astrophysics*, 417:1173–1181, April 2004.
- [27] J. Colgan, M. S. Pindzola, and N. R. Badnell. Dielectronic recombination data for dynamic finite-density plasmas. V: The lithium isoelectronic sequence. *Astronomy and Astrophysics*, 417:1183–1188, April 2004.
- [28] Z. Altun, A. Yumak, N. R. Badnell, J. Colgan, and M. S. Pindzola. Dielectronic recombination data for dynamic finite-density plasmas. VI. The boron isoelectronic sequence. *Astronomy and Astrophysics*, 420:775–781, June 2004.
- [29] O. Zatsarinny, T. W. Gorczyca, K. Korista, N. R. Badnell, and D. W. Savin. Dielectronic recombination data for dynamic finite-density plasmas. VII. The neon isoelectronic sequence. *Astronomy and Astrophysics*, 426:699–705, November 2004.
- [30] D. M. Mitnik and N. R. Badnell. Dielectronic recombination data for dynamic finite-density plasmas. VIII. The nitrogen isoelectronic sequence. *Astronomy and Astrophysics*, 425:1153–1159, October 2004.
- [31] O. Zatsarinny, T. W. Gorczyca, J. Fu, K. T. Korista, N. R. Badnell, and D. W. Savin. Dielectronic recombination data for dynamic finite-density plasmas. IX. The fluorine isoelectronic sequence. *Astronomy and Astrophysics*, 447(1):379–387, February 2006.

- [32] N. R. Badnell. Dielectronic recombination data for dynamic finite-density plasmas. X. The hydrogen isoelectronic sequence. *Astronomy and Astrophysics*, 447(1):389–395, February 2006.
- [33] Z. Altun, A. Yumak, N. R. Badnell, S. D. Loch, and M. S. Pindzola. Dielectronic recombination data for dynamic finite-density plasmas. XI. The sodium isoelectronic sequence. *Astronomy and Astrophysics*, 447(3):1165–1174, March 2006.
- [34] M. A. Bautista and N. R. Badnell. Dielectronic recombination data for dynamic finite-density plasmas. XII. The helium isoelectronic sequence. *Astronomy and Astrophysics*, 466(2):755–762, May 2007.
- [35] Z. Altun, A. Yumak, I. Yavuz, N. R. Badnell, S. D. Loch, and M. S. Pindzola. Dielectronic recombination data for dynamic finite-density plasmas. XIII. The magnesium isoelectronic sequence. *Astronomy and Astrophysics*, 474(3):1051–1059, November 2007.
- [36] Sh. A. Abdel-Naby, D. Nikolić, T. W. Gorczyca, K. T. Korista, and N. R. Badnell. Dielectronic recombination data for dynamic finite-density plasmas. XIV. The aluminum isoelectronic sequence. *Astronomy and Astrophysics*, 537:A40, January 2012.
- [37] M. Gu. Dielectronic recombination rate coefficients for h-like through ne-like isosequences of mg, si, s, ar, ca, fe, and ni. *The Astrophysical Journal*, 590:1131, 12 2008.
- [38] Taha Sochi and Peter J. Storey. Dielectronic recombination lines of c+. *Atomic Data and Nuclear Data Tables*, 99(6):633–650, November 2013.
- [39] Sultana N. Nahar. Electron-Ion Recombination Rate Coefficients and Photoionization Cross Sections for Astrophysically Abundant Elements. XII. Na IX, Na X, Mg X, and Mg XI for Ultraviolet and X-Ray Modeling. *The Astrophysical Journal Supplement Series*, 167(2):315–333, December 2006.

- [40] S N Nahar, J Oelgoetz, and A K Pradhan. Recombination rate coefficients for kll dielectronic satellite lines of fe xxv and ni xxvii. *Physica Scripta*, 79(5):055301, April 2009.
- [41] C. Ballance, S Loch, M Pindzola, and D Griffin. Dielectronic recombination of w35 +. *Journal of Physics B: Atomic, Molecular and Optical Physics*, 43:205201, 09 2010.
- [42] M. S. Pindzola, S. D. Loch, and F. Robicheaux. Dielectronic recombination in C³⁺ above and below the ionization threshold. *Physical Review A*, 83(4):042705, April 2011.
- [43] H. N. Russell and F. A. Saunders. New Regularities in the Spectra of the Alkaline Earths. *The Astrophysical Journal*, 61:38, January 1925.
- [44] M. Fogle, N. R. Badnell, P. Glans, S. D. Loch, S. Madzunkov, Sh. A. Abdel-Naby, M. S. Pindzola, and R. Schuch. Electron-ion recombination of Be-like C, N, and O. *Astronomy and Astrophysics*, 442(2):757–766, November 2005.
- [45] Z. K. Huang, W. Q. Wen, X. Xu, S. Mahmood, S. X. Wang, H. B. Wang, L. J. Dou, N. Khan, N. R. Badnell, S. P. Preval, S. Schippers, T. H. Xu, Y. Yang, K. Yao, W. Q. Xu, X. Y. Chuai, X. L. Zhu, D. M. Zhao, L. J. Mao, X. M. Ma, J. Li, R. S. Mao, Y. J. Yuan, B. Wu, L. N. Sheng, J. C. Yang, H. S. Xu, L. F. Zhu, and X. Ma. Dielectronic and Trielectronic Recombination Rate Coefficients of Be-like Ar¹⁴⁺. *The Astrophysical Journal Supplement Series*, 235(1):2, March 2018.
- [46] M. Schnell, M.E. Bannister, S. Böhm, G. Gwinner, S. Kieslich, A. Müller, S. Schippers, D. Schwalm, W. Shi, A. Wolf, and S.-G. Zhou. Trielectronic recombination in be-like ions. *Nuclear Instruments and Methods in Physics Research Section B: Beam Interactions with Materials and Atoms*, 205:367–369, 2003. 11th International Conference on the Physics of Highly Charged Ions.
- [47] D Mantia, Weronika Biela, J Tanis, and Andrzej Warczak. Evidence of trielectronic recombination for ar ions in an ebit. *Journal of Physics: Conference Series*, 1412:192015, 01 2020.

- [48] Gloria Delgado-Inglada, Mónica Rodríguez, Manuel Peimbert, Grażyna Stasińska, and Christophe Morisset. Oxygen enrichment in carbon-rich planetary nebulae. *Monthly Notices of the Royal Astronomical Society*, 449(2):1797–1810, May 2015.
- [49] K Z Arellano-Córdova, C Esteban, J García-Rojas, and J E Méndez-Delgado. The galactic radial abundance gradients of c, n, o, ne, s, cl, and ar from deep spectra of h ii regions. *Monthly Notices of the Royal Astronomical Society*, 496(2):1051–1076, 06 2020.
- [50] Stefan Schippers. Astrophysical relevance of storage-ring electron-ion recombination experiments. In *Journal of Physics Conference Series*, volume 163 of *Journal of Physics Conference Series*, page 012001. IOP, April 2009.
- [51] Charlotte Froese Fischer, Tomas Brage, and Per Jönsson. *Computational Atomic Structure: An MCHF Approach*. Institute of Physics Publishing, Bristol, UK; Philadelphia, PA, 1997.
- [52] Robert D. Cowan. *The Theory of Atomic Structure and Spectra*. University of California Press, 1981.
- [53] A. Bar-Shalom, M. Klapisch, and J. Oreg. HULLAC, an integrated computer package for atomic processes in plasmas. *Journal of Quantitative Spectroscopy and Radiative Transfer*, 71:169–188, October 2001.
- [54] J. Abdallah, R. E. H. Clark, D. P. Kilcrease, G. Csanak, and C. J. Fontes. Various applications of atomic physics and kinetics codes to plasma modeling. In Albert L. Osterheld and William H. Goldstein, editors, *Atomic Processes in Plasmas (Tenth)*, volume 381 of *American Institute of Physics Conference Series*, pages 131–142. AIP, July 1996.
- [55] JJ Abdallah, REH Clark, and RD Cowan. Los alamos national laboratory manual no. Technical report, LA-11436-M, 1988.
- [56] C. J. Fontes, H. L. Zhang, J. Abdallah, Jr., R. E. H. Clark, D. P. Kilcrease, J. Colgan, R. T. Cunningham, P. Hakel, N. H. Magee, and M. E. Sherrill. The Los Alamos suite of relativistic

- atomic physics codes. *Journal of Physics B Atomic Molecular Physics*, 48(14):144014, July 2015.
- [57] Christopher J. Fontes, James Colgan, and Joseph Abdallah, Jr. Self-consistent Large-Scale Collisional-Radiative Modeling. In Yuri Ralchenko, editor, *Modern Methods in Collisional-Radiative Modeling of Plasmas*, pages 17–50. Springer, 2016.
- [58] F.A. Parpia, C.Froese Fischer, and I.P. Grant. Grasp92: A package for large-scale relativistic atomic structure calculations. *Computer Physics Communications*, 94(2):249–271, 1996.
- [59] P. Jönsson, X. He, C. Froese Fischer, and I.P. Grant. The grasp2k relativistic atomic structure package. *Computer Physics Communications*, 177(7):597–622, 2007.
- [60] P. Jönsson, G. Gaigalas, J. Bieroń, C. Froese Fischer, and I. P. Grant. New version: GRASP2K relativistic atomic structure package. *Computer Physics Communications*, 184(9):2197–2203, September 2013.
- [61] N R Badnell. Dielectronic recombination of fe_{22+} and fe_{21+} . *Journal of Physics B: Atomic and Molecular Physics*, 19(22):3827, nov 1986.
- [62] N R Badnell. On the effects of the two-body non-fine-structure operators of the breit - pauli hamiltonian. *Journal of Physics B: Atomic, Molecular and Optical Physics*, 30(1):1, jan 1997.
- [63] N. R. Badnell. A Breit-Pauli distorted wave implementation for AUTOSTRUCTURE. *Computer Physics Communications*, 182(7):1528–1535, July 2011.
- [64] Pavlo Bilous, Adriana Pálffy, and Florian Marquardt. Deep-learning approach for the atomic configuration interaction problem on large basis sets, 2023.
- [65] Jinzhe Zhang, Jinde Liu, Yi Qin, Renjie Liu, Chen Yang, and Gang Jiang. Variational monte carlo configuration-interaction approach for multielectron atoms within the multiconfigurational dirac-hartree-fock framework. *Physical Review A*, 110, 12 2024.

- [66] Yan Ting Li, Kai Wang, Ran Si, Michel Godefroid, Gediminas Gaigalas, Chong Yang Chen, and Per Jönsson. Reducing the computational load – atomic multiconfiguration calculations based on configuration state function generators. *Computer Physics Communications*, 283:108562, 2023.
- [67] G. Breit. The effect of retardation on the interaction of two electrons. *Phys. Rev.*, 34:553–573, Aug 1929.
- [68] Leslie L. Foldy and Siegfried A. Wouthuysen. On the dirac theory of spin 1/2 particles and its non-relativistic limit. *Phys. Rev.*, 78:29–36, Apr 1950.
- [69] T. D. Newton and E. P. Wigner. Localized states for elementary systems. *Rev. Mod. Phys.*, 21:400–406, Jul 1949.
- [70] H. A. Bethe and E. E. Salpeter. *Quantum mechanics of one- and two-electron atoms*. Academic Press/Springer-Verlag, 1957.
- [71] David Layzer. On a screening theory of atomic spectra. *Annals of Physics*, 8(2):271–296, 1959.
- [72] A. Bar-Shalom, J. Oreg, W. H. Goldstein, D. Shvarts, and A. Zigler. Super-transition-arrays: A model for the spectral analysis of hot, dense plasma. *Physical Review A*, 40(6):3183–3193, September 1989.
- [73] M. S. Pindzola, N. R. Badnell, and D. C. Griffin. Validity of the independent-processes and isolated-resonance approximations for electron-ion recombination. *Physical Review A*, 46(9):5725–5729, November 1992.
- [74] Alan Burgess. Dielectronic Recombination and the Temperature of the Solar Corona. *The Astrophysical Journal*, 139:776–780, February 1964.

- [75] Enrico Fermi. *Nuclear Physics*, page 142. University of Chicago Press, Chicago, IL, USA, 1950. A course given by Enrico Fermi at the University of Chicago, notes compiled by Jay Orear, A.H. Rosenfeld, and R.A. Schluter.
- [76] Paul M. A. Dirac. *The Principles of Quantum Mechanics*. Oxford University Press, 1930.
- [77] Kohei Sugita, Hideaki Matsuura, and Yasuyuki Nakao. On the ion distribution function in degenerate electron plasmas. *Plasma and Fusion Research*, 8:3404050–3404050, 05 2013.
- [78] Håkan Danared. Electron cooling at CRYRING with an expanded electron beam. *Nuclear Instruments and Methods in Physics Research A*, 391(1):24–31, February 1997.
- [79] H. P. Summers. *The ADAS User Manual, version 2.6*, 2004.
- [80] J M Zhang and Y Liu. Fermi’s golden rule: its derivation and breakdown by an ideal model. *European Journal of Physics*, 37(6):065406, October 2016.
- [81] V. Debierre and E. Lassalle. The onset time of Fermi’s golden rule. *Proceedings of the Royal Society of London Series A*, 477(2248):20200777, April 2021.
- [82] Tobias Micklitz, Alan Morningstar, Alexander Altland, and David A. Huse. Emergence of fermi’s golden rule. *Phys. Rev. Lett.*, 129:140402, Sep 2022.
- [83] Jianyi Chen, Songtao Huang, Yunpeng Ji, Grant L. Schumacher, Alan Tsidilkovski, Alexander Schuckert, Gabriel G. T. Assumpção, and Nir Navon. Emergence of fermi’s golden rule in the probing of a quantum many-body system, 2025.
- [84] F. J. Dyson. The radiation theories of tomonaga, schwinger, and feynman. *Phys. Rev.*, 75:486–502, Feb 1949.
- [85] G. Gabrielse, D. Hanneke, T. Kinoshita, M. Nio, and B. Odom. New determination of the fine structure constant from the electron g value and qed. *Phys. Rev. Lett.*, 97:030802, Jul 2006.

- [86] H. Brunner. *Volterra integral equations : an introduction to theory and applications / Hermann Brunner*. Cambridge monographs on applied and computational mathematics ; 30. Cambridge University Press, Cambridge, first edition. edition, 2017.
- [87] Amy C. Gall, Adam R. Foster, Roshani Silwal, Joan M. Dreiling, Alexander Borovik, Jr., Ethan Kilgore, Marco Ajello, John D. Gillaspay, Yuri Ralchenko, and Endre Takács. EBIT Observation of Ar Dielectronic Recombination Lines near the Unknown Faint X-Ray Feature Found in the Stacked Spectrum of Galaxy Clusters. *The Astrophysical Journal*, 872(2):194, February 2019.
- [88] M. F. Gu, P. Beiersdorfer, G. V. Brown, S. M. Kahn, D. A. Liedahl, K. J. Reed, and D. W. Savin. Laboratory Measurements of Resonant Contributions to Fe XXIV Line Emission. *Physica Scripta Volume T*, 80(2):310–311, January 1999.
- [89] F. Sciortino, N. T. Howard, R. Reksoatmodjo, A. R. Foster, J. W. Hughes, E. S. Marmar, M. A. Miller, S. Mordijck, T. Odstrčil, T. Pütterich, M. L. Reinke, J. E. Rice, and P. Rodriguez-Fernandez. Experimental inference of neutral and impurity transport in Alcator C-Mod using high-resolution x-ray and ultra-violet spectra. *Nuclear Fusion*, 61(12):126060, December 2021.
- [90] Dian Lu, Fudi Wang, Luis F. Delgado-Aparicio, Yang Yang, Kenneth Hill, Cheonho Bae, Manfred Bitter, Jia Fu, Hongming Zhang, Yongcai Shen, Yifei Jin, Haijing Liu, Liang He, Shengyu Fu, Qing Zang, and Bo Lyu. Observations of xenon spectra on the EAST x-ray crystal spectrometer for high-temperature plasma diagnostics. *Nuclear Fusion*, 63(5):056002, May 2023.
- [91] Hitomi Collaboration. Atomic data and spectral modeling constraints from high-resolution X-ray observations of the Perseus cluster with Hitomi. *Publications of the Astronomical Society of Japan*, 70(2):12, March 2018.

- [92] G. A. Doschek. Soft X-Ray Spectroscopy of Solar Flares: an Overview. *The Astrophysical Journal Supplement Series*, 73:117, June 1990.
- [93] F. Robicheaux, S. D. Loch, M. S. Pindzola, and C. P. Ballance. Contribution of Near Threshold States to Recombination in Plasmas. *Physical Review Letters*, 105(23):233201, December 2010.
- [94] A. Nemer, N. C. Sterling, J. Raymond, A. K. Dupree, J. García-Rojas, Qianxia Wang, M. S. Pindzola, C. P. Ballance, and S. D. Loch. First Evidence of Enhanced Recombination in Astrophysical Environments and the Implications for Plasma Diagnostics. *The Astrophysical Journal Letters*, 887(1):L9, December 2019.

Appendices

Appendix A
Operator Relations

In this appendix we will review some useful operator relations to support the derivations and proofs in Chapters 5 and 7. The derivations of these relations will be outlined.

A.1 Commutators with products of operators

The commutator between an operator, \widehat{A} , and a product of two operators, \widehat{B} and \widehat{C} can be computed as follows:

$$\left[\widehat{A}, \widehat{BC} \right] = \widehat{A}\widehat{B}\widehat{C} - \widehat{B}\widehat{C}\widehat{A} = \widehat{A}\widehat{B}\widehat{C} - \widehat{B}\widehat{A}\widehat{C} + \widehat{B}\widehat{A}\widehat{C} - \widehat{B}\widehat{C}\widehat{A} \quad ,$$

$$\left[\widehat{A}, \widehat{BC} \right] = \left[\widehat{A}, \widehat{B} \right] \widehat{C} + \widehat{B} \left[\widehat{A}, \widehat{C} \right] \quad . \quad (\text{A.1})$$

The above result can be extended to the commutator with a product of p operators as follows:

$$\left[\widehat{A}, \prod_{i=1}^p \widehat{B}_i \right] = \sum_{k=0}^{p-1} \left(\prod_{i=1}^k \widehat{B}_i \right) \left[\widehat{A}, \widehat{B}_{k+1} \right] \left(\prod_{i=k+2}^p \widehat{B}_i \right)$$

$$\Rightarrow \left[\widehat{A}, \prod_{i=1}^p \widehat{B}_i \right] \widehat{B}_{p+1} + \prod_{i=1}^p \widehat{B}_i \left[\widehat{A}, \widehat{B}_{p+1} \right] = \sum_{k=0}^{p-1} \left(\prod_{i=1}^k \widehat{B}_i \right) \left[\widehat{A}, \widehat{B}_{k+1} \right] \left(\prod_{i=k+2}^p \widehat{B}_i \right) \widehat{B}_{p+1} + \prod_{i=1}^p \widehat{B}_i \left[\widehat{A}, \widehat{B}_{p+1} \right] \quad .$$

$$\begin{aligned}
& \because \left[\widehat{A}, \prod_{i=1}^p \widehat{B}_i \right] = \sum_{k=0}^{p-1} \left(\prod_{i=1}^k \widehat{B}_i \right) \left[\widehat{A}, \widehat{B}_{k+1} \right] \left(\prod_{i=k+2}^p \widehat{B}_i \right) \\
& \implies \left[\widehat{A}, \prod_{i=1}^{p+1} \widehat{B}_i \right] = \sum_{k=0}^p \left(\prod_{i=1}^k \widehat{B}_i \right) \left[\widehat{A}, \widehat{B}_{k+1} \right] \left(\prod_{i=k+2}^{p+1} \widehat{B}_i \right) \\
& \& \left[\widehat{A}, \widehat{B}_1 \widehat{B}_2 \right] = \left[\widehat{A}, \widehat{B}_1 \right] \widehat{B}_2 + \widehat{B}_1 \left[\widehat{A}, \widehat{B}_2 \right] \quad .
\end{aligned}$$

$$\therefore \left[\widehat{A}, \prod_{i=1}^p \widehat{B}_i \right] = \sum_{k=0}^{p-1} \left(\prod_{i=1}^k \widehat{B}_i \right) \left[\widehat{A}, \widehat{B}_{k+1} \right] \left(\prod_{i=k+2}^p \widehat{B}_i \right) \quad (\forall p \in \mathbb{N} \geq 2) \quad \square \quad . \quad (\text{A.2})$$

A.2 Block diagonal matrices

Let \mathcal{B} be a set of indices, and \mathcal{B}' be a subset of \mathcal{B} . Consider a block diagonal matrix \widehat{Y} that has a block whose set of indices are \mathcal{B}' , X , and another block diagonal matrix \widehat{X} that has a block whose set of indices are \mathcal{B} :

$$X_{mn} = 0 \text{ if } m \in \mathcal{B} \text{ \& } n \notin \mathcal{B}$$

$$Y_{mn} = 0 \text{ if } m \in \mathcal{B}' \subseteq \mathcal{B} \text{ \& } n \notin \mathcal{B}'$$

We show that \widehat{Y} commutes with \widehat{X} :

$$\left[\widehat{X}, \widehat{Y} \right]_{mn} = \sum_a X_{ma} Y_{an} - Y_{ma} X_{an} \quad ,$$

$$m \in \mathcal{B} \implies \left[\widehat{X}, \widehat{Y} \right]_{mn} = \sum_{a \in \mathcal{B}} X_{ma} Y_{an} - Y_{ma} X_{an} \quad ,$$

$$\because n \notin \mathcal{B} \implies Y_{an} = X_{an} = 0 \quad (\forall a \in \mathcal{B}) \quad ,$$

$$\begin{aligned} \therefore X_{mn} &= 0 \text{ if } m \in \mathcal{B} \text{ \& } n \notin \mathcal{B} \quad , \\ Y_{mn} &= 0 \text{ if } m \in \mathcal{B}' \subseteq \mathcal{B} \text{ \& } n \notin \mathcal{B}' \quad , \\ \implies \left[\widehat{X}, \widehat{Y} \right]_{mn} &= 0 \text{ if } m \in \mathcal{B} \text{ \& } n \notin \mathcal{B} \quad . \end{aligned} \tag{A.3}$$

Now, consider a Taylor expansion in powers of \widehat{Y} acting on \widehat{X} in the following way:

$$\left(T(-\widehat{Y}s) \widehat{X} T(\widehat{Y}s) \right)_{mn} = \sum_{a,b} T(-\widehat{Y}s)_{ma} X_{ab} T(\widehat{Y}s)_{bn} \quad .$$

We show that, because the sets of block indices of \widehat{Y} are subsets of those of \widehat{X} , the sets of block indices of the matrix resulting from the transformation above are the same as those of \widehat{X} :

$$m \in \mathcal{B} \implies \left(T(-\widehat{Y}s) \widehat{X} T(\widehat{Y}s) \right)_{mn} = \sum_{a,b \in \mathcal{B}} T(-\widehat{Y}s)_{ma} X_{ab} T(\widehat{Y}s)_{bn} \quad .$$

$$\because n \notin \mathcal{B} \implies T(\widehat{Y}s)_{bn} = \sum_{k=0}^{\infty} T_k s^k (\widehat{Y})_{bn}^k = 0 \quad ,$$

$$\begin{aligned} \therefore X_{mn} &= 0 \text{ if } m \in \mathcal{B} \text{ \& } n \notin \mathcal{B} \quad , \\ Y_{mn} &= 0 \text{ if } m \in \mathcal{B}' \subseteq \mathcal{B} \text{ \& } n \notin \mathcal{B}' \quad , \\ \implies \left(T(-\widehat{Y}s) \widehat{X} T(\widehat{Y}s) \right)_{mn} &= 0 \text{ if } m \in \mathcal{B} \text{ \& } n \notin \mathcal{B} \quad \square \quad . \end{aligned} \tag{A.4}$$

Appendix B

Angular momentum of a single particle

In this appendix, we review some of the relations for single-particle angular momentum operators to support the derivations in Chapter 7.

The squared angular momentum $\widehat{\mathbf{J}}^2$ can be expressed using ladder operators \widehat{J}_{\pm} that are defined using the component operators \widehat{J}_x and \widehat{J}_y :

$$\left(\widehat{J}_x \mp i\widehat{J}_y\right) \left(\widehat{J}_x \pm i\widehat{J}_y\right) = \widehat{J}_x^2 + \widehat{J}_y^2 \pm i \left[\widehat{J}_x, \widehat{J}_y\right] ,$$

$$\widehat{\mathbf{J}}^2 \equiv \widehat{J}_x^2 + \widehat{J}_y^2 + \widehat{J}_z^2 = \left(\widehat{J}_x \mp i\widehat{J}_y\right) \left(\widehat{J}_x \pm i\widehat{J}_y\right) \mp i \left[\widehat{J}_x, \widehat{J}_y\right] + \widehat{J}_z^2 , \quad (\text{B.1})$$

$$\widehat{J}_{\pm} \equiv \frac{1}{\hbar} \left(\widehat{J}_x \pm i\widehat{J}_y\right) , \quad (\text{B.2})$$

$$\widehat{\mathbf{J}}^2 = \hbar^2 \widehat{J}_{\mp} \widehat{J}_{\pm} \pm \hbar \widehat{J}_z + \widehat{J}_z^2 . \quad (\text{B.3})$$

The ladder operators have the following commutator relations:

$$\frac{1}{\hbar} \left[\widehat{J}_z, \widehat{J}_x \pm i\widehat{J}_y\right] = i\widehat{J}_y \pm \widehat{J}_x ,$$

$$\left[\widehat{J}_z, \widehat{J}_\pm \right] = \pm \hbar \widehat{J}_\pm \quad , \quad (\text{B.4})$$

$$\left[\widehat{J}_x + i\widehat{J}_y, \widehat{J}_x - i\widehat{J}_y \right] = -i \left[\widehat{J}_x, \widehat{J}_y \right] + i \left[\widehat{J}_y, \widehat{J}_x \right] = 2\hbar \widehat{J}_z \quad ,$$

$$\left[\widehat{J}_+, \widehat{J}_- \right] = \frac{2}{\hbar} \widehat{J}_z \quad . \quad (\text{B.5})$$

The commutator of \widehat{J}_z and \widehat{J}^2 can be calculated as follows:

$$\begin{aligned} \left[\widehat{J}_z, \widehat{J}^2 \right] &= \hbar^2 \left[\widehat{J}_z, \widehat{J}_- \widehat{J}_+ \right] = \hbar^2 \left[\widehat{J}_z, \widehat{J}_- \right] \widehat{J}_+ + \hbar^2 \widehat{J}_- \left[\widehat{J}_z, \widehat{J}_+ \right] \\ &= -\hbar^3 \widehat{J}_- \widehat{J}_+ + \hbar^3 \widehat{J}_- \widehat{J}_+ \quad , \end{aligned}$$

$$\left[\widehat{J}_z, \widehat{J}^2 \right] = 0 \quad . \quad (\text{B.6})$$

By rotational symmetry, this result extends to the other components:

$$\begin{aligned} \left[\widehat{J}_z, \widehat{J}^2 \right] &= \left[\widehat{J}_x, \widehat{J}^2 \right] = \left[\widehat{J}_y, \widehat{J}^2 \right] = 0 \\ \implies \left[\widehat{J}_x \pm i\widehat{J}_y, \widehat{J}^2 \right] &= 0 \quad , \end{aligned}$$

$$\left[\widehat{J}^2, \widehat{J}_\pm \right] = 0 \quad . \quad (\text{B.7})$$

Because they commute, $\widehat{\mathbf{J}}^2$ and \widehat{J}_z must have the same eigenstates:

$$\begin{cases} \widehat{J}_z |\alpha, m\rangle = \hbar m |\alpha, m\rangle \\ \widehat{\mathbf{J}}^2 |\alpha, m\rangle = \hbar^2 \alpha |\alpha, m\rangle \end{cases} . \quad (\text{B.8})$$

The action of the ladder operators on the eigenstate can be partially derived as follows:

$$\begin{aligned} \widehat{J}_z \widehat{J}_\pm |\alpha, m\rangle &= \left(\widehat{J}_\pm \widehat{J}_z + [\widehat{J}_z, \widehat{J}_\pm] \right) |\alpha, m\rangle = \hbar(m \pm 1) \widehat{J}_\pm |\alpha, m\rangle \quad , \\ \widehat{\mathbf{J}}^2 \widehat{J}_\pm |\alpha, m\rangle &= \left(\widehat{J}_\pm \widehat{\mathbf{J}}^2 + [\widehat{\mathbf{J}}^2, \widehat{J}_\pm] \right) |\alpha, m\rangle = (\hbar^2 \alpha + 0) \widehat{J}_\pm |\alpha, m\rangle \quad , \end{aligned}$$

$$\implies \widehat{J}_\pm |\alpha, m\rangle = C_\pm(\alpha, m) |\alpha, m \pm 1\rangle \quad . \quad (\text{B.9})$$

The action of $\widehat{\mathbf{J}}^2$ on the states with the maximum eigenvalue m_{\max} and the minimum eigenvalue m_{\min} respectively, is:

$$\begin{aligned} \widehat{\mathbf{J}}^2 |\alpha, m_{\max}\rangle &= \left(0 + \hbar^2 m_{\max} + \hbar^2 m_{\max}^2 \right) |\alpha, m_{\max}\rangle = \hbar^2 \alpha |\alpha, m_{\max}\rangle \\ \widehat{\mathbf{J}}^2 |\alpha, m_{\min}\rangle &= \left(0 - \hbar^2 m_{\min} + \hbar^2 m_{\min}^2 \right) |\alpha, m_{\min}\rangle = \hbar^2 \alpha |\alpha, m_{\min}\rangle \quad . \end{aligned}$$

The above expressions motivate a change of variables. Define j as:

$$j \equiv m_{\max} = -m_{\min} \quad . \quad (\text{B.10})$$

Then, the eigenvalue of $\widehat{\mathbf{J}}^2$ is given by:

$$\widehat{\mathbf{J}}^2 |j, m\rangle = \hbar^2 j(j+1) |j, m\rangle \quad (\text{B.11})$$

To find the explicit action of the ladder operators on the eigenstates of \widehat{J}_z , first show the following complex conjugate relation:

$$\begin{aligned}
C_{\pm}(j, m) &= \langle j, m \pm 1 | \widehat{J}_{\pm} | j, m \rangle \\
&= \left(\widehat{J}_{\mp} | j, m \pm 1 \rangle \right)^{\dagger} | j, m \rangle \\
&= (C_{\mp}(j, m \pm 1) | j, m \rangle)^{\dagger} | j, m \rangle \\
\implies C_{\pm}(j, m) &= C_{\mp}^*(j, m \pm 1) \quad ,
\end{aligned}$$

$$C_{\mp}(j, m \pm 1) = C_{\pm}^*(j, m) \quad . \quad (\text{B.12})$$

Now, the action of the ladder operators on the eigenstates of \widehat{J}_z can be found by using the expression (B.1):

$$\begin{aligned}
\hbar^2 \widehat{J}_{\mp} \widehat{J}_{\pm} | j, m \rangle &= \left(\widehat{J}^2 \mp \hbar \widehat{J}_z - \widehat{J}_z^2 \right) | j, m \rangle \quad , \\
\hbar^2 C_{\mp}(j, m \pm 1) C_{\pm}(j, m) &= \hbar^2 (j^2 + j \mp m - m^2) | j, m \rangle
\end{aligned}$$

$$\implies |C_{\pm}(j, m)|^2 = (j \mp m)(j \pm m + 1) \quad .$$

Then, the action of the ladder operators on the eigenstates of \widehat{J}_z is:

$$\widehat{J}_{\pm} | j, m \rangle = \sqrt{(j \mp m)(j \pm m + 1)} | j, m \pm 1 \rangle \quad . \quad (\text{B.13})$$

We can extend this expression to find the action of all powers of the ladder operator on these eigenstates as follows:

$$\begin{aligned}\widehat{J}_-^p |j, m\rangle &= \prod_{\gamma=0}^{p-1} \sqrt{(j+m-\gamma)(j-m+\gamma+1)} |j, m-p\rangle \\ &= \sqrt{\frac{(j+m)!(j-m+p)!}{(j+m-p)!(j-m)!}} |j, m-p\rangle \quad , \\ \widehat{J}_+^p |j, m\rangle &= \prod_{\gamma=0}^{p-1} \sqrt{(j-m-\gamma)(j+m+\gamma+1)} |j, m+p\rangle \\ &= \sqrt{\frac{(j-m)!(j+m+p)!}{(j-m-p)!(j+m)!}} |j, m+p\rangle \quad .\end{aligned}$$

In summary, we have:

$$\left\{ \begin{array}{l} \widehat{J}_z |j, m\rangle = \hbar m |j, m\rangle \\ \widehat{J}^2 |j, m\rangle = \hbar^2 j(j+1) |j, m\rangle \\ \widehat{J}_\pm^p |j, m\rangle = \sqrt{\frac{(j\mp m)!(j\pm m+p)!}{(j\mp m-p)!(j\pm m)!}} |j, m\pm p\rangle \end{array} \right. \quad . \quad (\text{B.14})$$